Doctoral Dissertation
Doctoral Program in Chemical Engineering (34th Cycle)

Metal Oxide Catalysts for the Abatement of Volatile Organic Compounds and Carbonaceous Particulate Matter

By

Miguel José Marín Figueredo

******

Supervisor(s):
Prof. Marco Piumetti, Supervisor

Doctoral Examination Committee:
Prof. Ioan-Cezar Marcu, Referee, University of Bucharest
Prof. Francesco Mauriello, Referee, Mediterranea University of Reggio Calabria

Politecnico di Torino
2022

Declaration

I hereby declare that, the contents and organization of this dissertation constitute my own original work and does not compromise in any way the rights of third parties, including those relating to the security of personal data.

Miguel J. Marin Figueredo

2022

* This dissertation is presented in partial fulfillment of the requirements for **Ph.D. degree** in the Graduate School of Politecnico di Torino (ScuDo).

Mom and Dad, this work is dedicated to both of you.
Dad, from heaven, I hope you are proud of the outcome of all these years.

Acknowledgments

These years have been full of sacrifice and efforts. Among the good and the bad, finally, the time converted into an outcome. For this experience I would like to thank Prof. Marco Piumetti for his guidance and advice during this path. Moreover, I want to thank professors Samir Bensaid, Nunzio Russo and Debora Fino for allowing me to perform my research using fine instruments and the laboratories of the CREST group. Special thanks to Mauro Raimondo, Fabio Deorsola, Camilla Galletti and Salvatore Guastella for the elevated number of physico-chemical analyses carried out and reported in this work. As well, thank you Mrs. Marangoni for your assistance during these years. I feel fortunate to have met Ferenc, Melodj and Tahrizi during the Ph.D., your contribution during the work of these years was fundamental and I really appreciate it. Thanks as well to the other Ph.D. candidates that were there to help when most needed, Clarissa, Enrico S., Mara, Fabio, Loredana, Giuseppe, Freddy and Hilmar. Special thanks to those who were close to me and giving me courage and support during this period, you are my Italian family, Paolo, Estefany, Barbara, Alessandro, Gean, Gabriel, Hernan, Agostina and Tullio. To my entire family and friends, thank you all for supporting me throughout these years, I hope to be able to see you again in a short time, in Venezuela, in Argentina, in Chile, in the U.S.A., in Dominican Republic, in Spain, it does not matter where you are, I know we will be together again sharing good moments.

Abstract

This thesis work aims to investigate different metal-oxide based materials as catalysts for the abatement of volatile organic compounds (VOCs) and carbonaceous particulate matter, i.e., nowadays typical atmospheric pollutants.

From the various synthesis procedures reported in the literature, the solution combustion synthesis (SCS) represents an easy, relatively economic and fast pathway for the preparation of catalytic powder materials. As well, the sol-gel procedure is a facile procedure that allows to prepare mesoporous materials with promising structural and catalytic performances. Consequently, these two procedures were carried out in order to synthesize active powder catalysts. Moreover, an in-situ synthesis procedure was used in order to prepare catalyzed monoliths (structured catalysts).

The catalysts investigated contain metals that are between the most abundant elements in the earth crust. Accordingly, the elements present in the catalysts were engineered with an eye towards the preparation of sustainable, low-temperature active and relatively economic catalysts. Oxide materials have been object of study due to their promising catalytic performances. In this sense, various single-metal and, particularly, mixed oxide catalysts were synthesized in order to better investigate their physico-chemical and catalytic properties in the catalytic abatement of VOCs and carbon soot.

Cerium oxide is a catalyst known by the redox behavior that occurs between Ce^{4+} and Ce^{3+} species, that allows the structure to storage oxygen. As well, manganese oxides have evidenced interesting catalytic performances mainly correlated to the occurrence of different oxidation state species ($Mn^{4+}|Mn^{3+}|Mn^{2+}$). Accordingly, efforts have been carried out in order to improve the catalytic activity of these materials, as of an example, by means of doping them with other elements, preparing mixed oxides, or by promoting cooperative interactions (or synergy) between different oxide phases.

The catalytic materials studied in this work were characterized by means of complementary characterization techniques, e.g., X-ray diffraction (XRD), N_2 physisorption at -196 °C, field-emission scanning electron microscopy (FESEM), X-ray photoelectron spectroscopy (XPS), hydrogen and soot temperature-programmed reduction (H_2-TPR, soot-TPR), oxygen temperature-programmed desorption (O_2-TPD). The catalytic screenings were performed in a PID-controlled TPO setup. The powder catalysts were tested in a U-tube fixed-bed reactor, whereas the monoliths were tested in a bench-scale stainless steel tubular reactor system. Propylene and ethylene were used as VOC probe molecules, whereas Printex-U was used as carbon soot surrogate.

Mixed cerium oxide-based families (Ce-Mn, Ce-Cu and Ce-Mn-Cu) were synthesized by means of the SCS. The best performance in propylene oxidation were attributed to beneficial interactions occurring between clusters of MnO_x that and CeO_2. Instead, the co-presence of MnO_x, CuO and CeO_2 species was responsible of the excellent catalytic results in ethylene oxidation at low temperature. The catalysts that were deposited over SiC monoliths showed as well good catalytic performances, and converted the VOCs at temperatures below those required for the thermal non-catalytic oxidation. The powders and the monolith catalysts evidenced good catalytic stability and reproducibility.

Mesoporous manganese oxides (doped with Cu and/or Fe) were synthesized by means of the sol-gel technique. The optimum catalytic activities observed in VOC oxidation were correlated to the following aspects: high superficial population chemisorbed oxygen species and the improved low-temperature reducibility. As well, beneficial interactions between Mn, Cu and Fe most likely improve the activity of the parent Mn_2O_3 catalyst Reproducible catalytic performances in VOC oxidation were observed for the most promising catalyst. Additional studies were carried out over the catalysts prepared by means of the sol-gel technique, in order to investigate their catalytic performance in soot oxidation under a stream containing 5 vol.% H_2O. Furthermore, the simultaneous soot and propylene oxidation was assessed. For the catalytic soot oxidation, the ratio between the Mn^{3+}/Mn^{2+} species was the key parameter, whereas for the propylene oxidation reaction the key parameter was the improved low-temperature reducibility (caused by the incorporation of Cu in the Mn_2O_3 structure). Little deactivation for the soot oxidation reaction was observed under a gaseous stream containing H_2O and, as well over the severely aged catalysts. Remarkably, the contemporary soot-propylene oxidation test evidenced a probable cooperative effect from the

propylene oxidation reaction, towards the oxidation of soot particles in “tight” contact with the catalyst.

Finally, a comparative study was performed between catalysts synthesized by means of the SCS and sol-gel technique. Different synthesis conditions evidenced marked changes in the physico-chemical properties of the catalyst. The best catalytic performances in VOC oxidation were attributed to the improved reducibility at low temperatures and to the increased amount of chemisorbed oxygen species, active for oxidation reactions. Similarly, the mentioned characteristics demonstrated to play a key role in the oxidation of soot particles in “tight” contact with the catalyst. On the other hand, the oxidation of soot particles under “loose” contact conditions highlighted the beneficial role of the catalyst’s “filter-like” morphology that seems to trap soot particles. Under the latter condition, the probable high amount of acid-sites characteristic of catalysts containing Mn_3O_4 seems co-responsible for the good catalytic performance observed in soot oxidation.

Contents

List of Figures

List of Tables

Chapter 1

State of the Art

1.1 Introduction

The "state of the art" section provides a brief introduction of the most relevant topics that are discussed in this thesis work. To begin, the definitions of volatile organic compounds and carbonaceous particulate matter are explained. As well, the methods utilized for the control or abatement of those substances in industrial streams were defined. An insight was included regarding the materials used in heterogeneous catalysis, particularly, for oxidation reactions.

1.2 Volatile Organic Compounds (VOCs)

The volatile organic compounds are a group of chemical substances that are produced in the atmosphere as a consequence of either natural processes (i.e. biogenic VOCs) or as a result of human-related activities (anthropogenic VOCs) (Koppmann, 2007). While biogenic VOCs are emitted mostly from land vegetation, examples of anthropogenic VOCs emission include industrial processes (e.g., fossil fuel production, waste management) and daily or household activities (e.g., painting, transport, etc.).

Different regulations have issued different definitions for these chemical compounds. As of an example, the European legislation (in force) defines, according to the Directive 2004/42/CE, a volatile organic compound as "… *any organic compound having an initial boiling point less than or equal to 250 °C measured at a standard pressure of 101,3 kPa*" (European Parliament and Council, 2004). Instead, the United States Environment Protection Agency (EPA) describes

the VOCs as "… *any compound of carbon, excluding carbon monoxide, carbon dioxide, carbonic acid, metallic carbides or carbonates and ammonium carbonate, which participates in atmospheric photochemical reactions, except those designated by EPA as having negligible photochemical reactivity*" (United States Environmental Protection Agency, 2021b). Both definitions highlight two paramount characteristics of the VOCs, e.g., the physical properties that can be measured or estimated, and the reactivity of the compounds in atmospheric photochemical reactions.

Considering the chemical properties of these compounds, they may constitute a health risk for humans (e.g. teratogenic, mutagenic, toxic, carcinogenic) (Bloemen & Burn, 1993; Ramírez, Cuadras, Rovira, Borrull, & Marcé, 2012). The amount of these substances in present in outdoor and (especially) in indoor environments is of relevant importance (Fu, Wei, Jia, Zheng, & Guan, 2021; Sarigiannis, Karakitsios, Gotti, Liakos, & Katsoyiannis, 2011). Consistently, this highlights the potential effect of these compounds in decreasing the breathing air quality and thus the necessity of eventual assessments of the exposure risk.

1.3 Carbonaceous Particulate Matter

Different research studies have evidenced the increasing incidence of various health issues due to the exposure to airborne particulate matter (Hime, Marks, & Cowie, 2018; Mukherjee & Agrawal, n.d.; Wu, Jin, & Carlsten, 2018). Accordingly, the penetration of these particles in the human body should be avoided. As a consequence, environmental regulations are being applied, e.g., in Europe (European Parliament and Council, 2008) and in the United States (United States Environmental Protection Agency, 2021a) in order to reduce the emissions of particulate matter. The corresponding environmental regulations classify the particulate matter according to its diameter, as follows:

- PM_{10}: Considers generally particles with diameters below 10 µm.
- $PM_{2.5}$: Includes very fine particles with diameters with lengths below 2.5 µm.

According to the literature (Gupta & Kumar Singh, 2016; Mohankumar & Senthilkumar, 2017), the nucleation of solid carbonaceous matter takes place subsequently to the combustion of hydrocarbons (HCs) under lean oxygen condition, i.e. due to the occurrence of HC pyrolysis. After the nucleation phase, the surface of the particles grows thus enhancing a coalescence process that results in the final particulate matter (PM). Therefore, the carbon soot constitutes elemental

carbon that is aggregated and forming particles. Additionally, the particles usually present adsorbed organic compounds, sulfur, and metal oxides.

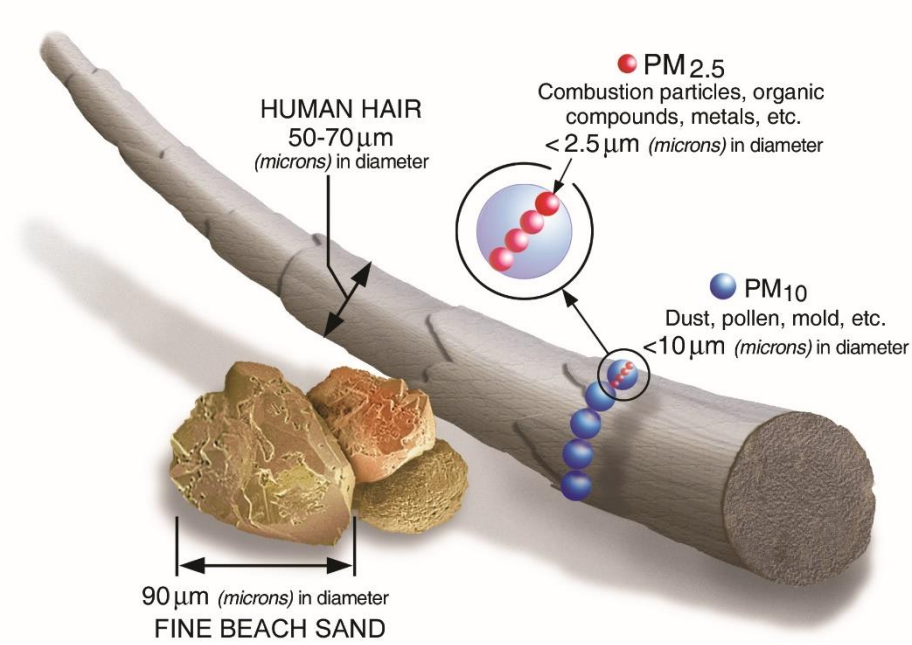

Figure 1.1 Comparison of the possible length of soot particles. Extracted from (United States Environmental Protection Agency, 2021a).

In this sense, carbonaceous particulate matter is a residue of the combustion occurring in the motors of vehicles. In fact, the automotive industry has performed investigations and developed technologies for the catalytic elimination of PM (e.g. Diesel particulate filters, DPF) produced in internal combustion engines.

Nevertheless, particulate matter is also produced in industrial environments. In fact, the literature reports (from the oil-industry) the gas flaring process (Fawole, Cai, & Mackenzie, 2016) as an important emission source. Accordingly, the energy industry accounts nowadays an elevated share of the carbonaceous particle emissions world widely (Ni et al., 2014).

1.4 Control techniques of VOCs Emissions in Industrial Streams

In order to diminish the industrial emissions of VOCs, several techniques have been developed. Depending on the emission control technique over the industrial streams, it is possible to recover/capture the emitted compounds or to reduce its concentration to amounts acceptable by the regulations in force. In this sense, the

following group comprises some processes that have been developed as VOC control techniques:

- **Adsorption** (Khan & Kr. Ghoshal, 2000; X. Li et al., 2020; Yang et al., 2019): For this process, the VOC (adsorbate) interacts with a solid material (adsorbent). The adsorption of the adsorbate can be physical or chemical. In the former phenomenon the molecule is withhold on the surface of the adsorbent by means of Van der Waals attraction forces, whereas in the latter the formation of chemical bonds takes place. In order to recover the adsorbed molecules (and eventually eliminate them by means of another process), a pressure or temperature swing process can be used. Consistently, this technique can result expensive if the treated flow has low concentration of VOCs. The materials used in adsorption processes include carbons, silica gels, clays and zeolites.
- **Thermal oxidation** (Khan & Kr. Ghoshal, 2000; Krishnamurthy, Adebayo, Gelles, Rownaghi, & Rezaei, 2020): in this process the organic compounds are oxidized at elevated temperatures (ca. 900-1000 °C), leading to the formation of carbon dioxide and water. This type of process is more energetically-efficient when the stream treated contains elevated amounts of VOCs. Otherwise, the elevated temperatures that must be achieved would require the use of a high amount of fuel. As equipment, a thermal oxidizer is used for the elimination task. This type of process may then allow to storage or recover the energy derived from the exothermic reaction.
- **Catalytic oxidation** (Kamal, Razzak, & Hossain, 2016; Khan & Kr. Ghoshal, 2000; Krishnamurthy et al., 2020; Yang et al., 2019): Consists in a process similar to thermal oxidation, but it is carried out at lower temperatures due to the use of catalysts. The operative temperature depends on the activity of the catalytic material used and, as well, on the nature of the VOC to eliminate. In this sense, catalysts containing noble metals usually have excellent catalytic activities at lower temperatures, respect to other catalytic materials, e.g. metal oxides. In this sense, this technique allows to reduce the fuel consumption required for the abatement. The reactors used in this type of process include fixed-bed reactors and monolithic or honeycomb structures. This type of process allows to treat streams containing low VOC concentrations.
- **Absorption** (Khan & Kr. Ghoshal, 2000; U.S. Environmental Protection Agency. Office of Air and Radiation, 1992): The process consists in trapping the VOC molecule by means of a liquid solvent.

Consistently, a good affinity between the VOC and the corresponding solvent is required. Absorption towers comprise a (randomly or structured) packed-bed that enhanced the contact between the liquid absorbent and the gaseous VOC. Moreover, tower containing plates that enhance the gas-liquid contact can be used. During the cost planning, it is important to consider the regeneration of the used solvent. This technique is not considered for the treatment of streams containing low VOC concentrations.

1.5 Heterogeneous Catalysis in the Elimination of VOCs and Soot

Considering the physicochemical properties of the VOCs, many of them are likely to be found in gaseous state. On the other hand, carbon soot is a solid substance. In both cases, solid catalysts may be used in order to perform the corresponding catalytic abatement. Evidently, the mentioned cases imply the occurrence of gas-solid or solid-solid state reactions.

In heterogeneous catalysis, solids can be used as catalysts for the abatement task. The active sites located over the surface of the catalyst must be reached by the reactants for the reaction to take place. Accordingly, in order to better understand the catalytic oxidation reaction mechanisms (for the VOCs or soot), different mathematic models have been proposed and developed.

Several reaction mechanisms (and the corresponding rates expression) have been reported in the literature (Kamal et al., 2016; Krishnamurthy et al., 2020; Yang et al., 2019) in order to model the VOCs oxidation reaction, as follows:

- **Langmuir-Hinshelwood (LH) mechanism**: This model assumes that both the VOC and O_2 molecules adsorb onto the sites of the catalyst. Afterwards, the reaction takes place and the reaction product(s) desorb from the sites over the catalytic surface. The following equation has been reported for the VOC reaction rate:

$$-r_{VOC} = \frac{k\, K_{VOC} K_{O_2} P_{VOC} P_{O_2}}{(1 + K_{VOC} P_{VOC} + K_{O_2} P_{O_2})^2}$$

Where:

$-r_{VOC}$: reaction rate of the VOC molecule

K_x: equilibrium constant for the adsorption of the "x" molecule

P_x: partial pressure of the "x" molecule

As well, it can be assumed that the adsorption sites for the VOC molecule are different to those where oxygen adsorbs. For this case, the following expression has been reported:

$$-r_{VOC} = \frac{k\, K_{VOC} K_{O_2} P_{VOC} P_{O_2}}{(1 + K_{VOC} P_{VOC})(1 + K_{O_2} P_{O_2})}$$

- **Eley-Rideal (ER) mechanism**: this model assumes that one of the molecules is adsorbed on the sites over the catalytic surface. In this sense, the adsorbed molecule reacts with the other present in the gas-phase. Accordingly, the following rate expression has been reported for a case where the VOC is adsorbed and O_2 is present in the gas-phase:

$$-r_{VOC} = \frac{k\, K_{VOC} P_{VOC} P_{O_2}}{1 + K_{VOC} P_{VOC}}$$

- **Mars-van Krevelen (MvK) mechanism**: it is also known as the redox mechanism. The reaction pathway postulates that a redox cycle occurs over the catalytic surface, leading to the oxidation of the adsorbed molecule. In this sense, the VOC molecule adsorbs onto the catalytic surface and is oxidized by means of the structural oxygen (O^{2-}) in the catalyst (released by means of the reduction of the catalyst). The oxygen in the catalyst's structure is the replenished by means of gaseous O_2 molecules in the reactive environment. The following reaction rate has been reported:

$$-r_{VOC} = \frac{k_{VOC} P_{VOC} k_{O_2} P_{O_2}}{\gamma k_{VOC} P_{VOC} + k_{O_2} P_{O_2}}$$

Where:
k_{O2}: constant for the catalyst re-oxidation rate
k_{VOC}: VOC reaction rate constant
γ: Stoichiometric coefficient of O_2 in the oxidation reaction

In the literature, this redox mechanism has been reported to adequately model the VOC oxidation reaction rates over oxide and perovskite materials (Genuino, Dharmarathna, Njagi, Mei, & Suib, 2012; Mars & van Krevelen, 1954; Q. Wang, Yeung, & Bañares, 2020).

Regarding the modelling of the catalytic soot oxidation, the literature (Fino, Bensaid, Piumetti, & Russo, 2016; Marco Piumetti, Bensaid, Russo, & Fino, 2015) highlights the enormous complexity of this system. In this sense, the system

comprises a solid-solid reaction in which not only in the catalyst and the carbon soot take part, but also includes the oxygen required for the reaction. Accordingly, the better the interactions between these actors, the higher the combustion reaction rates. In fact, it has been reported that the intrinsic catalytic activity of surfaces is better investigated by means of catalytic tests in which an "intimate" contact between soot and the catalyst is assured. Under this complex scenario, it has been postulated that only a multi-population kinetics approach could adequately describe the catalytic soot combustion process.

The enhanced catalytic soot oxidation performance has been correlated to different physico-chemical phenomena in the literature. Recent studies outlined interesting parameters that aid in better understanding the efficient catalytic activity of different materials in the catalytic oxidation of soot. Under "tight" contact conditions, the oxidation reaction (even under reactive environments containing high amounts of O_2 or NO_2) seems to occur mainly by means of structural oxygen, thus following a MvK mechanism (Christensen, Grunwaldt, & Jensen, 2017). Furthermore, the aforementioned investigation highlighted the beneficial effect of an intermediate oxygen bond-strength over the catalyst for achieving optimum reaction rates under "loose" contact conditions. Similarly, other studies have reported the effectivity of catalysts that participate in redox cycles, e.g. CeO_2 (Fino et al., 2016) and that host increased populations of surface-chemisorbed oxygen species (O_α). Other physico-chemical characteristics like a high number of superficial Lewis acid-sites have demonstrated as well to play a key role in the better oxidative activity of oxide materials towards soot (Wagloehner, Baer, & Kureti, 2014; Wagloehner, Nitzer-Noski, & Kureti, 2015).

In order to better understand the soot oxidation process over metal oxides, a scheme was prepared and reported in Figure 1.2. The reaction mechanism was adapted according to the soot oxidation reaction mechanism published by (Gross, Ulla, & Querini, 2012) for cerium oxide catalyst. In this sense, the scheme shows the steps for the oxidation of soot by means of chemisorbed peroxide species. Moreover, it clarifies the pathway for the occurrence of the redox process over the catalytic surface that leads to the formation of oxygen-defective sites that are then replenished by means of gaseous O_2.

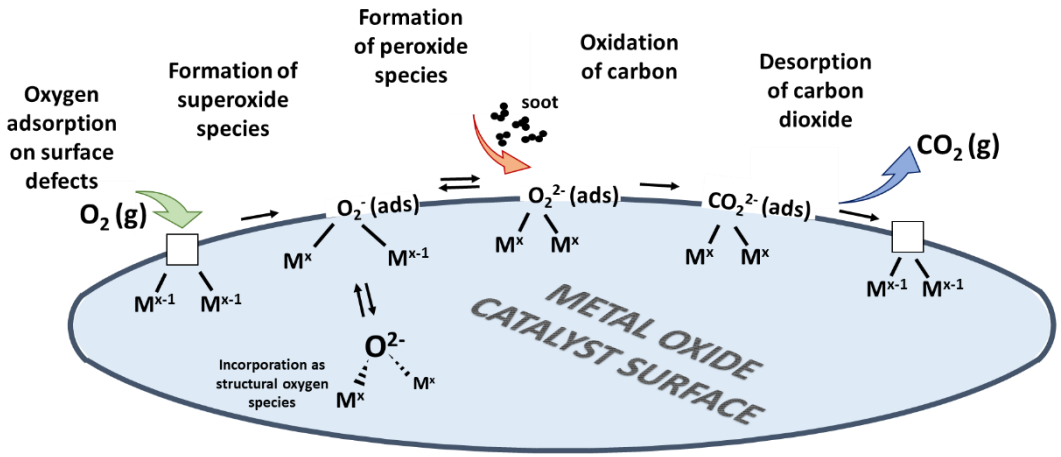

Figure 1.2 Scheme for the catalytic oxidation of soot by means of chemisorbed peroxide species over metal oxide catalysts. Adapted from (Gross, Ulla, & Querini, 2012).

1.6 Catalytic Materials for the Abatement of VOCs and Soot

Different materials, for example, metal oxides and mixed oxides or noble metals, have evidenced promising catalytic properties toward VOC and soot oxidation reaction. In this sense, these types of materials have been object of many investigations in the past years. The following groups summarize the families of catalysts commonly studied in the literature for the abatement of VOCs and carbon particulate matter.

1.6.1 Noble Metals

The noble metals commonly studied for the VOC oxidation reaction include the Pt, Pd and Au (Kamal et al., 2016; Liotta, 2010; Z. Zhang, Jiang, & Shangguan, 2016). As well, the activity of these materials has been reported for the catalytic oxidation of soot (Lee et al., 2021). These metals are commonly deposited over structured materials with elevated surface areas, which normally are resistant to elevated temperatures (like Al_2O_3, zeolites). Parameters like the metal dispersion and loading have shown to play a key role in the excellent catalytic performance of the supported noble metals (Abdelouahab-Reddam, Mail, Coloma, & Sepúlveda-Escribano, 2015; Joung et al., 2014; Liotta, 2010).

The literature highlights that these metals generally exhibit excellent catalytic performances in the oxidation of hydrocarbons at low temperatures. Nevertheless, the rather high cost of these materials, the likelihood of being poisoned by certain molecules (e.g. compounds containing sulfur or chlorine), and the possibility of

being deactivated due to a sintering process lead the researchers to study other catalytic materials like the metal oxides.

1.6.2 Single and Mixed Metal Oxides

Metal oxides have been widely investigated as alternative catalytic materials to the noble metals. Materials like copper, manganese, cerium, chromium oxides have been widely studied, since they have shown promising catalytic activities in VOC oxidation (Gelles, Krishnamurthy, Adebayo, Rownaghi, & Rezaei, 2020; Kamal et al., 2016). Interestingly, the improvement of the catalytic performance of transition metal oxides has been ascribed to different aspects like: (i) elevated population of chemisorbed oxygen-species and improved oxygen mobility/reducibility (Marco Piumetti, Fino, & Russo, 2015; Santos, Pereira, Órfão, & Figueiredo, 2010), (ii) electron-deficient structures with improved electron conductivity (in other words, the presence of positive holes) and the eventual ability to assume various oxidation states (Spivey, 1987).

Remarkably, mixed metal oxides have evidenced promising catalytic performances for the oxidation of VOCs, ascribed to possible beneficial (or in the best of cases, synergistic) interactions that take place between the metals in a single structure or, between oxide phases (Delimaris & Ioannides, 2008, 2009; Heynderickx, Thybaut, Poelman, Poelman, & Marin, 2010; Marco Piumetti, Bensaid, Andana, Russo, et al., 2017; Trovarelli, 2002). Accordingly, the aforementioned literature highlighted that doping metal oxides with other metals can lead to better structural stability, oxygen mobility, oxygen storage capacity, etc. Furthermore, it has been reported that the reducibility of metal species (like Ce) may be enhanced by means of oxides phase-interactions.

Regarding the single-metal oxides (e.g. MnO_x, CuO_x and FeO_x), their catalytic activities have been reported in the literature (Marco Piumetti, Bensaid, Andana, Russo, et al., 2017; Ranji-Burachaloo, Masoomi-Godarzi, Khodadadi, & Mortazavi, 2016; Wasalathanthri et al., 2017). Nevertheless, growing interest has been observed in the recent years about the catalytic properties of mixed oxide materials in the soot oxidation reaction have been reported in the literature (Andana et al., 2016; Bensaid et al., 2016; Dosa et al., 2018; S. Liu, Wu, Weng, & Ran, 2015; Marco Piumetti, Bensaid, Andana, Russo, et al., 2017).

Accordingly, the literature highlights the increased importance of the contact conditions between the catalyst and soot particles. Under “tight” contact conditions the intrinsic activity of the catalytic surfaces is better understood, since the number

of soot-catalyst contact points is maximized (Marco Piumetti, Bensaid, et al., 2015). However, this condition is not representative of typical Diesel particulate filters, therefore, studies under “loose” contact conditions are usually performed as well. Under the latter conditions, properties like a nanostructured morphology (e.g., nanorods, nanocubes, etc.) have evidenced to play a key role in soot oxidation, due to their tuned amount of crystalline planes active in oxidation reactions (Andana et al., 2016; Dosa et al., 2018).

Chapter 2

Materials and methods

2.1 Introduction

This chapter summarizes the various catalytic materials that were synthesized during the research activity. Moreover, the preparation techniques used for the aforementioned syntheses are explained in detail. Consistently, this section includes the experimental procedures of the sol-gel and the solution combustion synthesis techniques.

As well, the procedures carried out in order to perform the physicochemical characterization of the prepared catalysts are included in this chapter. Therefore, the operative parameters utilized during the performance of techniques like the N_2 physisorption at -196 °C, X-ray powder diffraction, field emission scanning electron microscopy, temperature-programmed analyses (reduction/desorption) and X-ray spectroscopy.

Finally, this chapter includes the experimental procedures carried out for the study of the catalytic activity of the synthesized materials for the different abatement reactions. The catalytic activity tests performed were typical temperature-programmed oxidation tests. During these tests, the catalytic materials performed the abatement of the probe molecule in a temperature-controlled reactor.

2.2 Synthesis procedures for the preparation of catalysts

During the research activities, the synthesis procedures investigated for the preparation of powder catalysts were the solution combustion synthesis and the sol-gel preparation techniques.

2.2.1 Solution combustion synthesis (SCS)

In a typical solution combustion synthesis procedure, the metal precursor(s) was/were dissolved in deionized water. In order to synthesize oxide powder catalysts (single metal or mixed), the precursors utilized were the corresponding metal nitrates. Therefore, the metal precursors utilized were the $Ce(NO_3)_3 \bullet 6H_2O$ from Alfa Aesar, while both the $Mn(NO_3)_2 \bullet 4H_2O$ and the $Cu(NO_3)_2 \bullet 3H_2O$ from Sigma-Aldrich. Along with the nitrate(s), an organic compound was dissolved in the same solution and was used as "fuel" for the synthesis.

For the catalysts reported in **Chapter 3**, this synthesis procedure was performed dissolving the nitrates along with urea (CH_4N_2O) in excess, (2x the stoichiometric amount respect to the nitrate/s) in 100 mL of deionized water. After stirring the solution magnetically for 5 min at room temperature (r.t.), the mixture was set in the oven and the temperature was raised (10 °C min^{-1}) until 650 °C (30 min). Three sets of powder catalysts (single metal and mixed oxides) were synthesized. The single metal oxides were the CeO_2, Mn_2O_3 and CuO. The notation used for the binary oxides is $Ce_{100-x}M_x$, where "M" stands for either Cu or Mn and "x" is the nominal atomic percent of the corresponding metal. Instead, the notation used for the ternary oxides was $Ce_{100-x}Mn_{x/2}Cu_{x/2}$. Consistently, the mixed oxides were denoted as: $Ce_{95}Mn_5$, $Ce_{85}Mn_{15}$, $Ce_{55}Mn_{45}$, $Ce_{95}Cu_5$, $Ce_{85}Cu_{15}$, $Ce_{55}Cu_{45}$, $Ce_{95}Mn_{2.5}Cu_{2.5}$, $Ce_{85}Mn_{7.5}Cu_{7.5}$ and $Ce_{55}Mn_{22.5}Cu_{22.5}$. Additionally, the powders that evidenced the most promising catalytic performances, thus the $Ce_{55}Mn_{45}$ and the $Ce_{55}Mn_{22.5}Cu_{22.5}$ were washcoated over SiC monoliths (Céramiques Techniches et Industrielles s.a.s.) of 290 cells per square inch (cpsi), length 3 cm and diameter of 2.54 cm. The aforementioned task was achieved by performing an in-situ SCS using precursor solutions identical to those used for the preparation of the powder catalysts. The solution was poured inside the channels of the monolith in order to saturate the walls with the precursors. Afterwards, in order to perform the synthesis and calcination, the monolith was set inside a preheated oven (ca. 650 °C) for 5 min. Subsequently, when the temperature of the monolith decreased to r.t., compressed air was flown inside the channels to remove eventual powders deposited loosely. These steps were carried out several times until the loading of

catalyst reached 15 wt.%, respect to its original mass. The notation for the catalyzed monoliths was: $Ce_{55}Mn_{45}$–SiC and $Ce_{55}Mn_{22.5}Cu_{22.5}$–SiC.

Two SCS manganese-oxide catalysts were investigated in **Chapter 6** (denoted as Mn_2O_3 – SCS and Mn_3O_4/Mn_2O_3 - SCS). The Mn_2O_3 – SCS catalyst was prepared using a precursor solution (total volume = 50 mL) containing the metal precursor (0.2 mol L^{-1}, $Mn(NO_3)_2•4H_2O$, Sigma-Aldrich) and citric acid (0.2 mol L^{-1}, $C_6H_8O_7•H_2O$, Sigma-Aldrich). The solution was homogenized by means of magnetic stirring for 10 min. The solution was set in an oven and heated (5 °C min^{-1}) from r.t. until 650 °C, in order to calcine the catalyst under isothermal conditions for 30 min. Instead, the preparation of the Mn_3O_4/Mn_2O_3 – SCS catalyst required to use a Mn nitrate-to-citric acid molar ratio of 1:1.25 in the solution. The solution was stirred for 10 min and was subsequently heated in the oven (10 °C min^{-1}) until 600 °C. It was calcined in isothermal conditions for 30 minutes. The resulting catalyst sample were gently ground by means of mortar and pestle.

2.2.2 Sol-gel synthesis

For the preparation of metal oxide catalysts by means of sol-gel synthesis, the corresponding precursor(s) amount(s) (e.g. $Mn(NO_3)_2•4H_2O$; $Fe(NO_3)_3•9H_2O$ and $Cu(NO_3)_2•3H_2O$, Sigma-Aldrich), along with CA (citric acid, $C_6H_8O_7•H_2O$ from Sigma-Aldrich) was/were dissolved in water.

The single-metal and mixed manganese-oxide catalysts investigated in **Chapters 4 and 5** (Mn_2O_3, $MnCu_{15}$, $MnFe_{15}$ and $MnCu_{7.5}Fe_{7.5}$) were prepared dissolving the corresponding nitrate(s) in Milli-Q water (50 mL), aiming to assure 0.2 M as the total molar concentration. For the samples containing various metals, a metal-to-manganese ratio was defined (e.g. for the $MnCu_{15}$ the content of Cu content was 15 at.%, while the Mn species in the solution corresponds to 85 at.%). The molar ratio between citric acid and the nitrates in the solution was a 1:1 (i.e. 0.2 M of CA). The solution was put inside a water bath at r.t. and was mixed continuously using a magnetic stirrer. The pH of the solution was raised (until pH = 5) adding the corresponding amount of an ammonium hydroxide solution (NH_4OH, Sigma-Aldrich). Afterwards, the temperature of the water bath was raised at a rate of ca. 1°C min^{-1}, until reaching a temperature of 60 °C. The isothermal condition was assured (2 h) in order to promote the formation and aggregation of colloidal particles. Subsequently, the particles were recovered from the suspension through vacuum filtration and were washed with abundant water, in order to remove any eventual residues of the precursor materials. The resulting material was dried

at 60 °C overnight. Afterwards, the calcination of the sample was performed at 550 °C for 2 h. The powders were ground gently with mortar and pestle.

In **Chapter 4**, CuO and Fe_2O_3 were synthesized with comparison purposes. A solution (0.2 M) containing the corresponding metal nitrate in Milli-Q water (50 mL) was prepared. A molar ratio of 1:1 was maintained between CA:$Cu(NO_3)_2$, while the ratio between CA:$Fe(NO_3)_3$ was 1.5:1. The solution set in a H_2O bath and stirred, and the pH was increased in both cases (solution containing copper ions: pH = 5; solution containing iron ions: pH = 7). Subsequently, the water bath was heated and the temperature increased to a value of 80 °C. The isothermal condition was maintained for 4 h. Afterwards, the resulting liquid was set in an oven overnight (60 °C.) Finally, the dry gel was calcined for 2 h (550 °C). The powders were ground gently with mortar and pestle

A similar procedure was used for synthesizing the catalysts reported in **Chapter 6**. Manganese nitrate tetrahydrate (0.2 M) and citric acid (0.2 M) were dissolved in Milli-Q water (50 mL). After magnetically stirring the solution, ammonium hydroxide was added dropwise in order to raise the pH to a value of pH=5. The solution was put in a H_2O bath, afterwards the temperature was increased slowly until reaching 60 °C. Isothermal conditions were maintained 2 h under continuous stirring. After separating the resulting particles from the solution and drying in the oven overnight (60 °C), each sample was heated (from r.t.) and calcined in isothermal condition as follows: (i) the Mn_2O_3-SG550 until 550 °C and (ii) the Mn_2O_3-SG650 until 650 °C.

2.3 Catalyst characterization techniques

Various characterization techniques were used in order to investigate the physico-chemical properties of the catalysts synthesized. The operative parameters utilized for each technique are described as follows:

The X-ray powder diffraction patterns were retrieved using an X'Pert Philips PW3040 diffractometer. Cu K_α radiation was used and the 2θ range was 20°-80° (step = 0.05° 2θ; 0.2 s per step). The patterns obtained in the analyses were indexed by means of the Powder Data File Database (PDF 2000) of the International Centre for Diffraction Data, Pennsylvania. Moreover, the Scherrer formula was used in order to estimate the average size of the crystallites, as follows:

$$D = \frac{0.9\,\lambda}{b\,\cos\theta}$$

Where:

D: crystallite size (Å)

0.9: shape factor for spherical particles (adim.)

λ: wavelength (Å)

b: full width at half maximum (radians)

θ: Bragg angle (radians)

N_2 physisorption analyses at -196 °C were carried out in a Micromeritics Tristar II 3020. Prior to the analysis, the powder samples were pretreated at 200 °C for 2 h in order to desorb eventual atmospheric pollutants. The specific surface area of the powders was estimated according to the Brunauer-Emmett-Teller method (BET). The cumulative volume of pores and the pore diameter (V_p and D_p, respectively) were estimated according to the Barrett-Joyner-Halenda (BJH) method.

The morphology of the prepared materials was investigated using a field emission scanning electron microscope (FESEM). The analyses reported in **Chapters 3, 4 and 5**, were carried out in a FESEM Zeiss Merlin, Gemini II column. As well, the average chemical composition of the powders was estimated by means of energy-dispersive spectroscopy (EDS, Oxford X-ACT), considering a suitable number of representative areas over the samples. Instead, the images reported in **Chapter 6** were obtained using a FESEM FEI QUANTA 200F. The operative parameters (e.g. extra high tension, working distance and probe intensity) were tuned during each analysis in order to improve the quality of the images.

The different temperature-programmed studies were carried out in a ThremoQuest TPD/R/O 1100 analyzer comprising a thermal conductivity detector (TCD). In all chapters, the reducibility of the samples was assessed by means of H_2 temperature-programmed reduction (H_2-TPR) analyses. Prior to the mentioned analysis, the powder catalyst was set in the tubular reactor and pretreated (ca. 1 h) under a He flow (40 mL min^{-1}) at 500 °C (only in **Chapter 4**) or 550 °C. Subsequently, the sample was reduced flowing H_2 5 vol.% in Ar, while the temperature was raised from 100 °C until 800 °C (5 °C min^{-1}). The final temperature was maintained constant for 10 min. As well, O_2 temperature-programmed desorption analyses (O_2-TPD) were performed for the synthesized catalysts (50 mg). The corresponding pretreatment was carried out under 40 mL min^{-1} of O_2 (550

°C, 30 min). Afterwards, the temperature of the sample was reduced (until 50 °C) under the same gaseous flow. The desorption phase was performed flowing He (20 mL min^{-1}), and raising the temperature in the range 50-950 °C (5 °C min^{-1}).

The reducibility of the catalysts by soot was investigated performing soot-TPR tests in **Chapters 5 and 6**. These tests were performed in a quartz U-tube reactor (internal diameter = 4 mm) containing a fixed-bed. The fixed-bed comprised the catalyst (45 mg), inert SiO_2 (150 mg) and soot (5 mg), in "tight contact" (condition assured by means of a ball milling process performed for 15 min, under 250 rpm). The reactor was placed in a furnace and a pretreatment was performed under a N_2 flow (100 mL min^{-1}) at 100 °C for 30 min. Afterwards, the temperature was increased from 100 °C to 700 °C under the same gaseous flow (heating rate = 5 °C min^{-1}). The reactor-outlet gases were analyzed in a NDIR gas-analyzer in order to determine the outflowing amounts of CO and CO_2.

The X-ray photoelectron spectroscopy technique (XPS) was performed using an XPS PHI 5000 Versa probe. The operative conditions were: band-pass energy = 187.85 eV; take off angle = 45°; X-ray sport size diameter = 100.0 μm. The spectra were resolved by means of the following software: Multipack 9.0.

2.4 Catalytic activity tests

Several procedures were performed over the synthesized catalysts in order to assess their catalytic activity and performance towards the abatement of the different atmospheric pollutant.

2.4.1 Total oxidation of VOCs over powder catalysts

The tests for VOC catalytic abatement were carried out in a temperature-programmed oxidation setup. The system contained a quartz U-tube reactor hosting the catalyst as a fixed-bed. For the tests, 100 mg of catalyst were set in the reactor. The catalytic tests were carried out flowing in the reactor a gaseous reactive mix containing the VOC probe molecule (500 ppm, C_2H_4 or C_3H_6), O_2 (10 vol.%) and N_2 (balance). The reactor heating was regulated using a PID controller, while the temperature in catalytic bed was measured by means of a thermocouple (K-type). ABB Uras 14, Non-dispersive infrared (NDIR) analyzers were used in order to estimate the concentration of CO and CO_2 in the reactor outlet, and thus to evaluate the conversion (%) of the VOC.

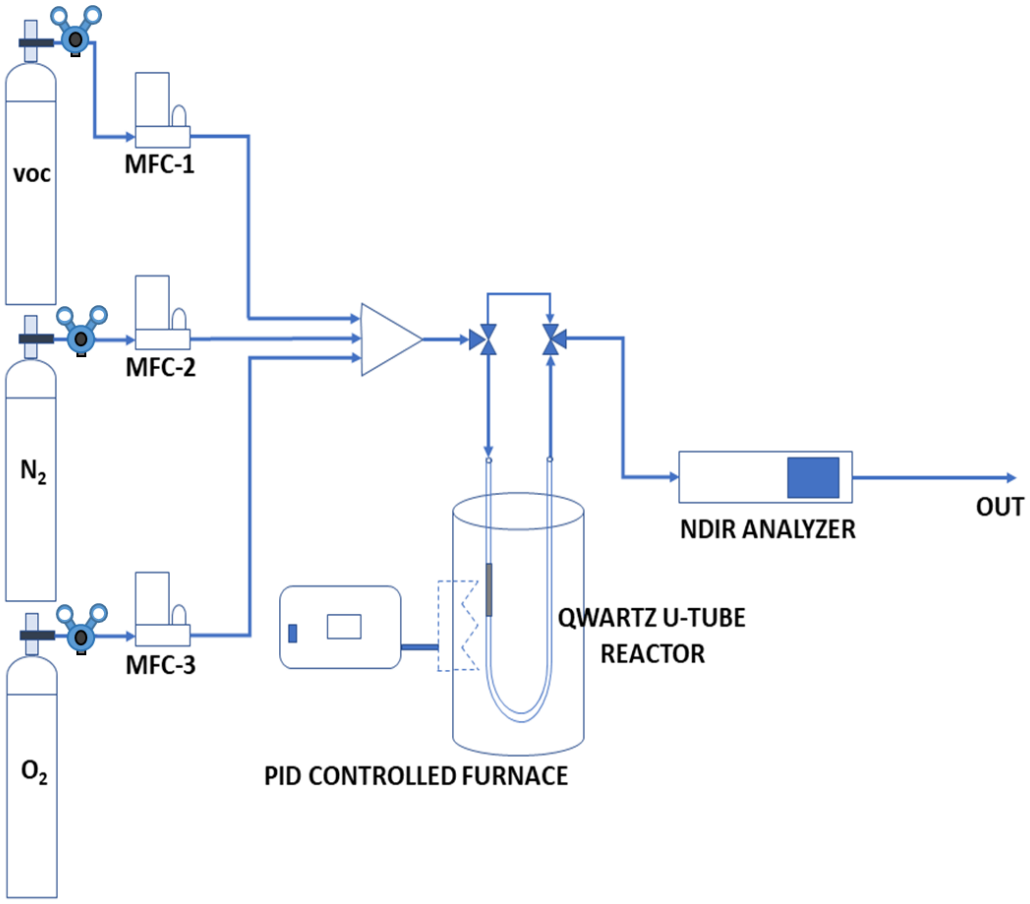

Figure 2.1 Representative scheme of the TPO setup used for the abatement of VOCs and soot over powder catalysts.

Before the catalytic tests included in **Chapter 3**, the powder was pretreated for 1 h under 15 mL min^{-1} of He at 150 °C. For the tests, 20,000 h^{-1} was maintained constant as the gas hourly space velocity (GHSV) parameter. Consequently, the W/F (weight-to-volumetric flow rate ratio) in the reactor was 0.065 g h L^{-1}. The temperature was raised from 50 °C until 350 °C, thus performing isothermal steps every 50 °C. The temperature was after the conversion of the corresponding VOC stabilized (in terms of the reactor-outflowing amounts of CO and CO_2). The reproducibility of the catalytic performance was investigated by means of three consecutive catalytic tests. In order to assess the catalytic performance of the powder catalysts under 100% of relative humidity, the gaseous reactive mix was bubbled in a vessel with water at 20 °C and was subsequently fed inside the reactor.

The catalytic tests reported in **Chapter 4** were carried out using pelletized catalysts with particle diameters between 212 µm and 300 µm. Before the test, a

pretreatment of 60 min was performed flowing N_2 (30 mL min^{-1}) in the reactor at 150 °C. The GHSV (20,000 h^{-1}) was maintained constant during the catalytic tests and corresponded to a W/F of 0.050 g h L^{-1}. The reactor temperature was increased from 100 °C to 400 °C, and isothermal steps were carried out every 30 °C. The temperature was increased when the VOC conversion was stabilized. Additionally, the reproducibility of the catalytic activity was investigated by conducting consecutive catalytic runs. The conditions used in this case were equal to those of the catalytic tests, while the temperature was raised at a rate of ca. 2 °C min^{-1}.

As reported in **Chapter 5**, the pelletized powders were subject to a degassing pretreatment, carried out flowing (100 mL min^{-1}) of N_2 at 150 °C for 60 min. Subsequently, the catalytic tests for the abatement of propylene were performed feeding 100 mL min^{-1} of gaseous reactive mix and the temperature was raised at a rate of 5 °C min^{-1} from r.t. until the total conversion of propylene was reached. Additionally, two consecutive catalytic tests were performed in order to evaluate the reproducibility of the catalytic performance. Furthermore, long-term catalytic tests (7 h) were carried out with swinging operative conditions to evaluate the stability of the catalytic performance. The humidity in the stream for the catalytic tests performed under 5 vol.% H_2O was achieved by means of an evaporation system containing liquid water.

Prior to the catalytic tests described in **Chapter 6**, the corresponding pelletized catalyst was pretreated flowing N_2 in the reactor at a rate of 100 mL min^{-1}. The pretreatment was carried out for 1 h at 150 °C. A GHSV of 20,000 h^{-1} was fixed during the tests and, therefore a W/F ratio equal to 0.044 g h L^{-1}. During the test, isothermal steps were performed every 30 °C and raising the temperature after the conversion was stabilized. The test started at 70 °C and was ended when the total oxidation of the VOC probe molecule was achieved.

2.4.2 Total oxidation of VOCs over catalyzed monoliths

As reported in **Chapter 3**, catalytic tests for the abatement of VOCs (ethylene and propylene) were performed over catalyzed SiC monoliths. The tests were carried out in a horizontal furnace (60 cm). For the tests, the corresponding catalyzed monolith was inserted inside a cordierite monolith and finally placed in a tubular stainless-steel reactor. The temperature at the inlet and outlet of the monolith was measured using two K-type thermocouples. Before each catalytic test, a degassing pretreatment was conducted at 150 °C, flowing He (300 mL min^{-1}) for 60 min. Afterwards, the catalytic tests were carried out flowing in the reactor a gaseous reactive mix containing 500 ppm of C_2H_4 or C_3H_6, O_2 (10 vol.%) and N_2 (balance).

During the test, a constant GHSV was maintained (9,000 h^{-1}), as well as the W/F ratio (0.031 g h L^{-1}). As well, the temperature was increased between 100-620 °C, maintaining a constant heating rate (5 °C min^{-1}). The amounts of CO and CO_2 outflowing from the reactor were evaluated with NDIR analyzers. The reproducibility of the catalytic performance was investigated by means of consecutive catalytic tests. Moreover, the long-term catalytic stability was evaluated performing time on stream tests.

2.4.3 Soot oxidation

In **Chapter 5** and **Chapter 6** catalytic tests for the abatement of carbonaceous particulate matter are included. These tests were performed in a temperature-programmed oxidation setup comprising a quartz U-tube reactor hosting a fixed-bed. The composition of the fixed-bed contained the catalyst (45 mg), inert silica (150 mg) and soot (Printex-U, 5 mg). The tests were carried out under two soot-catalyst contact dynamics: "loose" and "tight" contact. The "loose" contact condition was assured by gently mixing the corresponding powders with a spatula for three minutes. Instead, the "tight" contact between the powders was achieved performing a ball-milling process for 15 min at a rate of 250 rpm. Before the catalytic test, a pretreatment (30 min) was performed flowing N_2 (100 mL min^{-1}) at 100 °C. The catalytic tests were performed flowing 100 mL min^{-1} of a gaseous mix (content: 10 vol.% of O_2 in N_2). During the tests, the temperature in the reactor was raised (100-700 °C) at a constant heating rate (5 °C min^{-1}). The amounts of CO and CO_2 outflowing from the reactor were measured using NDIR analyzers.

Additional tests were performed and reported in **Chapter 5**, in order to evaluate the catalytic performance for soot oxidation under a stream containing a probe VOC (propylene). The powders comprised in the fixed-bed (soot, catalyst, inert silica) in "loose" contact. The composition of the gaseous mix fed to the reactor was: 500 ppm of propylene, O_2 (10 vol.%) and N_2 (balance). For the tests, the temperature was raised according to a rate of 3 °C min^{-1}, in the range 100-700 °C. Further catalytic tests for the simultaneous oxidation of C_3H_6 and soot were carried out under a stream containing 5 vol.% of H_2O. The required amount of water in the feed was assured by means of a water-evaporation system.

Chapter 3

Mixed Cerium-based Oxides (Ce-Mn-Cu) Prepared via Solution Combustion Synthesis (SCS) for the Abatement of VOCs

3.1 Introduction

This chapter includes the investigation regarding the catalytic activity improvement of CeO_2, due to the insertion of different transition metals in the lattice (e.g. copper and/or manganese). Moreover, better catalytic performances were observed when segregated oxide phases (e.g. MnO_x, CuO) were present in the catalysts.

The catalysts were synthesized by means of the solution combustion synthesis. The corresponding procedure, along with the set of prepared catalysts is reported in section 2.2.1. The study of the physico-chemical properties of the synthesized catalysts was carried out using several characterization techniques (as reported in section 2.3). Powder catalysts, as well as catalyst-coated SiC monoliths were prepared and tested for the ethylene and propylene oxidation reactions.

This chapter includes data resulting from my personal research and was published in: Marin Figueredo, M.J., Andana, T., Bensaid, S., Dosa, M., Fino, D., Russo, N., Piumetti, M. (2020). Cerium-Copper-Manganese Oxides Synthesized via Solution Combustion Synthesis (SCS) for Total Oxidation of VOCs. *Catalysis*

Letters, 150, pages 1821-1840. The publication and the copyright license are consultable at the following link: https://link.springer.com/article/10.1007/s10562-019-03094-x.

3.2 Material structural and textural properties

The powder diffraction data harvested by means of the XRD technique is reported in Figure 3.1. The data obtained for the ceria sample was attributed to diffraction of fluorite cerium (IV) oxide (reference code 01-081-0792), therefore a face-centered cubic structure consisting in hexahedral and octahedral holes containing oxygen ions (Trovarelli, 2002). The diffractograms evidence the presence of the fluorite structure of ceria in either the binary (Ce-Cu; Ce-Mn) or the ternary oxides (Ce-Mn-Cu). Interestingly, when the amount of foreign metal(s) in the mixed-oxides was 45 at.%, diffraction patterns corresponding to phases of CuO (reference code 00-045-0937), Mn_2O_3 (reference code 01-078-0390) and $Ce_{1.5}Mn_{1.5}O_4$ (reference code 01-070-0260) could be observed. This suggests that the formation of extra-framework metal oxide species took place.

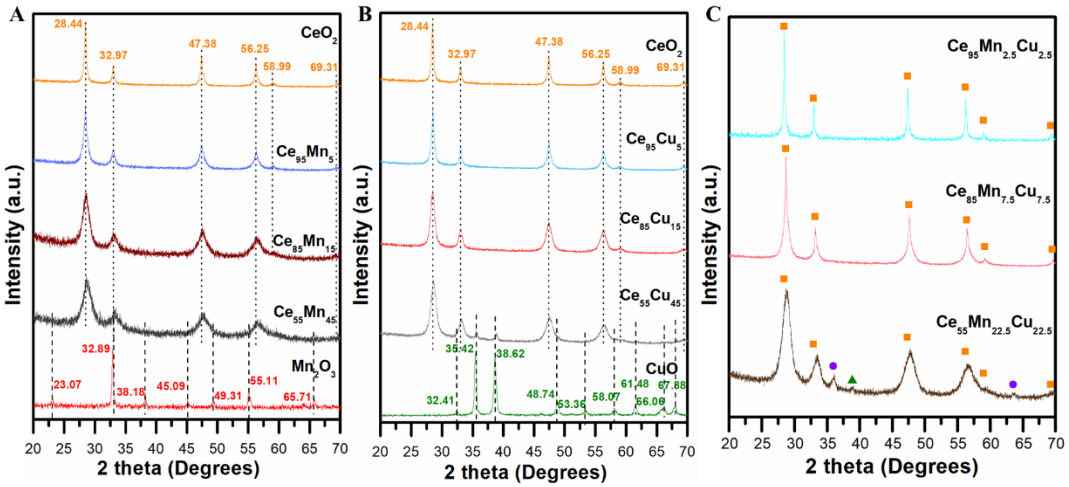

Figure 3.1 XRD diffractograms harvested for the (A) Ce-Mn, (B) Ce-Cu and (C) Ce-Mn-Cu set of samples. Metal oxide phases: CeO_2 = yellow square; $Cu_{1.5}Mn_{1.5}O_4$ = purple circle; green triangle = CuO. Reprinted from (Marin Figueredo et al., 2020).

Additionally, it can be observed that the higher the amount of foreign metal content, the broader the peaks in the XRD diffractogram. This trend could be associated to an increased amount of defect-rich crystallites in the studied materials (Ertl, Knözinger, & Weitkamp, 2008). Indeed, this condition could be favored due to the formation of smaller crystallites, as calculated by means of Scherrer's

formula (average size: 12 nm; see Table 3.1). This behavior suggests that the higher the amount of foreign metal, the smaller the size of the crystallites (see Figure 3.2).

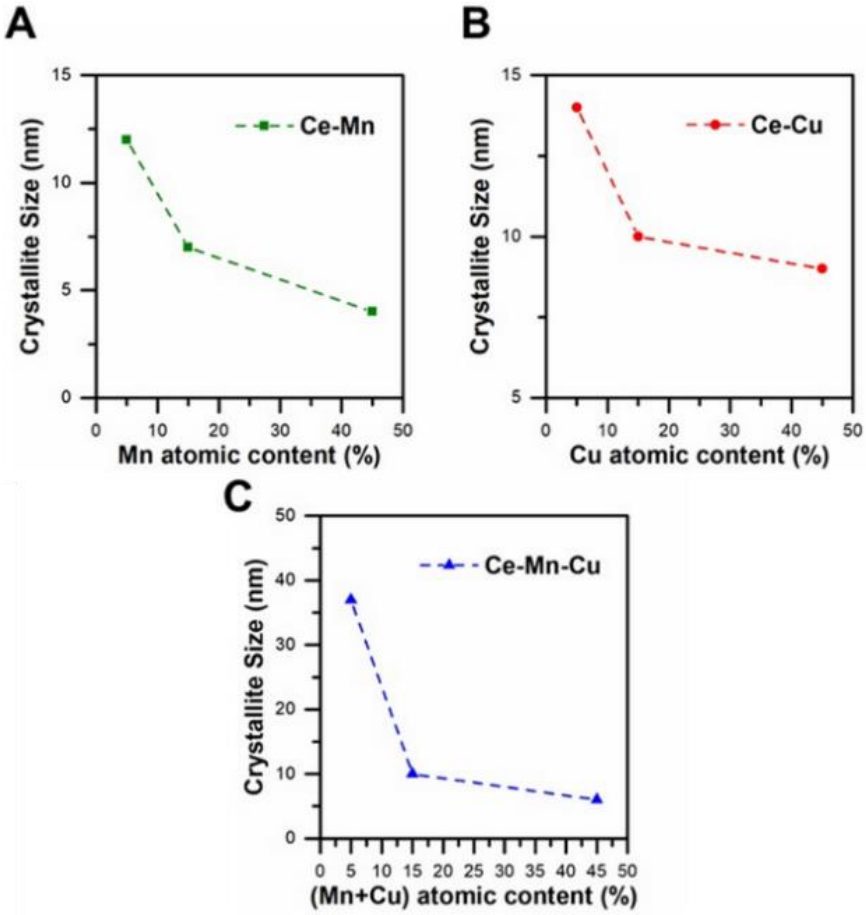

Figure 3.2 Trend of the crystallite size as a function of the content (at.%) of (A) Mn, (B) Cu and (C) Mn-Cu. Reprinted from (Marin Figueredo et al., 2020).

However, the occurrence of structural defects may take place simultaneously with strain effects due to the insertion of the foreign metals with different radii inside the framework of ceria.

The textural properties of the synthesized samples, according to the resulting data of the XRD and N_2 physisorption analyses, is summarized in Table 3.1. Accordingly, the specific surface area of the samples (calculated using the BET method) were comprised in the 8-48 m^2 g^{-1} range. Generally, higher BET surface area were observed in the catalysts with the lowest loading of foreign metal (thus Mn and/or Cu). Conversely, the catalysts containing the highest foreign metal loading evidenced worse textural properties. However, the $Ce_{95}Mn_{2.5}Cu_{2.5}$ catalyst evidenced an unexpected low BET surface area (8 m^2 g^{-1}), thus attributed to the formation of increased size crystallites (see Figure 3.2; Table 3.1). On the other

hand, the values obtained for the pore diameters (D_p = 11-24 nm) and the pore volumes (V_p = 0.02-0.12 cm^3 g^{-1}) of the catalysts were comparable.

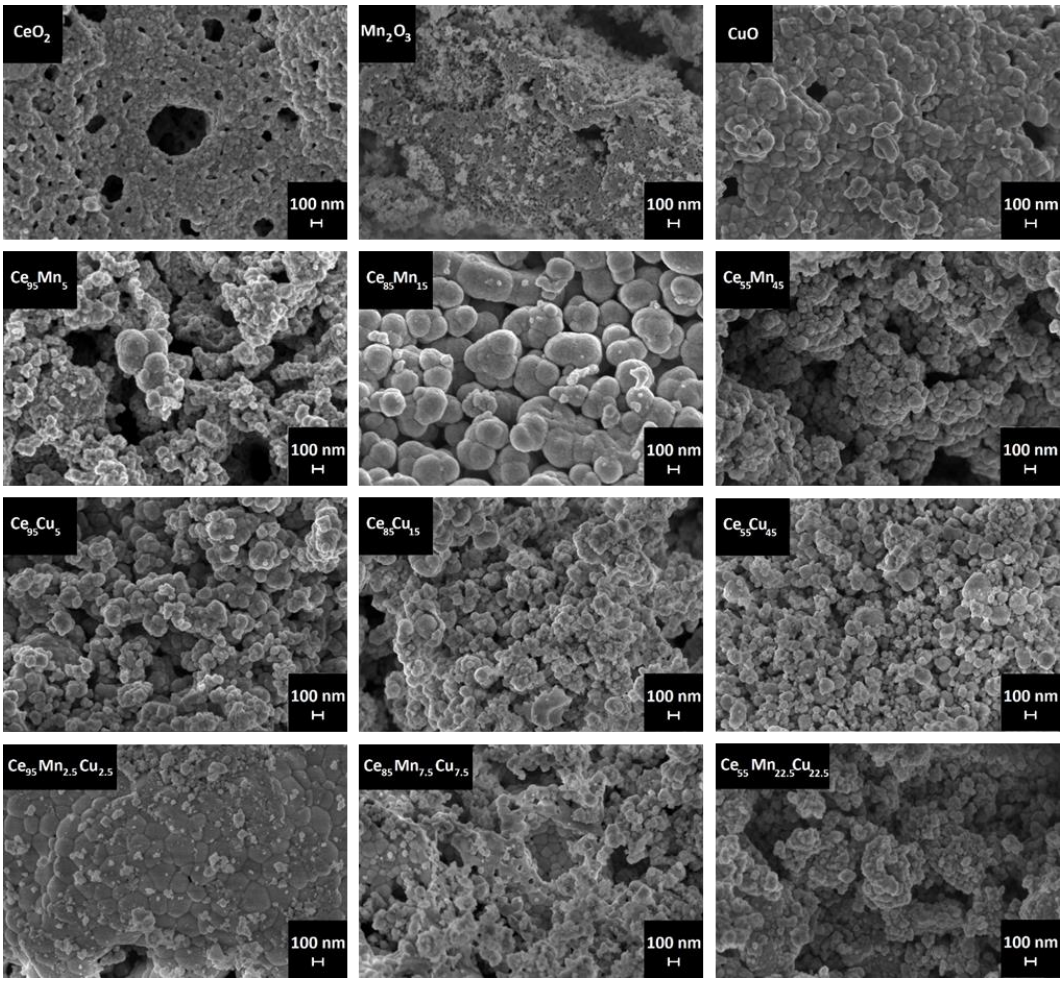

Figure 3.3 FESEM images of the synthesized catalysts. Reprinted from (Marin Figueredo et al., 2020).

Table 3.1 Textural properties of the synthesized catalysts calculated according to the data from the XRD and N_2 physisorption at -196 °C analyses. Reprinted from (Marin Figueredo et al., 2020)

Catalyst	**Crystallite size[a] (nm)**	**S_{BET}[b] (m^2 g^{-1})**	**V_p[c] (cm^3 g^{-1})**	**D_p[d] (nm)**
CeO_2	23	32	0.09	15
$Ce_{95}Mn_5$	12	39	0.07	11
$Ce_{85}Mn_{15}$	7	41	0.12	15
$Ce_{55}Mn_{45}$	4	21	0.11	17

Catalyst	Crystallite size[a] (nm)	S_{BET}[b] ($m^2\ g^{-1}$)	V_p[c] ($cm^3\ g^{-1}$)	D_p[d] (nm)
$Ce_{95}Cu_5$	14	48	0.09	14
$Ce_{85}Cu_{15}$	10	26	0.08	22
$Ce_{55}Cu_{45}$	9	16	0.06	17
$Ce_{95}Mn_{2.5}Cu_{2.5}$	37	8	0.02	13
$Ce_{85}Mn_{7.5}Cu_{7.5}$	10	38	0.10	17
$Ce_{55}Mn_{22.5}Cu_{22.5}$	6	18	0.10	24
Mn_2O_3	44	15	0.11	28
CuO	27	1	0.01	18

[a]calculated using Scherrer's formula; [b]specific surface area estimated by means of the BET method: [c]cumulative volume of pores; [d]diameter of pores calculated by means of the BJH method

The morphology of the synthesized materials as observed in FESEM is reported in Figure 3.3. The micrographs of the mixed catalysts evidenced surface characteristics similar to the morphology of ceria (the parent oxide), therefore the formation of porous materials with a globular surface. The size of the surface agglomerates observed in the set of Ce-Mn catalysts seems to increase when the amount of Mn is raised until 15 at.%. Instead, the size of these features decreased when the Mn atomic content was higher.

Table 3.2 Element atomic composition of the mixed oxide catalysts as derived from the EDS technique. Reprinted from (Marin Figueredo et al., 2020)

Sample	O (at.%)	Ce (at.%)	Cu (at.%)	Mn (at.%)
$Ce_{95}Mn_5$	67.00	31.20	-	1.80
$Ce_{85}Mn_{15}$	72.50	23.90	-	3.70
$Ce_{55}Mn_{45}$	69.80	18.10	-	12.10
$Ce_{95}Cu_5$	66.47	31.45	2.08	-
$Ce_{85}Cu_{15}$	62.00	31.50	6.50	-
$Ce_{55}Cu_{45}$	57.30	22.00	20.70	-
$Ce_{95}Mn_{2.5}Cu_{2.5}$	62.50	33.90	2.60	1.00
$Ce_{85}Mn_{7.5}Cu_{7.5}$	53.00	41.30	2.70	3.00
$Ce_{55}Mn_{22.5}Cu_{22.5}$	57.40	22.60	11.30	8.70

Interestingly, the specific surface area seems to follow o this trend (see Table 3.1), thus the bigger the agglomerates, the higher the BET surface area. Considering the Ce-Cu catalysts set, the diameter of the spherical features in the $Ce_{95}Cu_5$ and $Ce_{85}Cu_{15}$ is rather similar, while the $Ce_{55}Cu_{45}$ evidenced smaller surface agglomera-

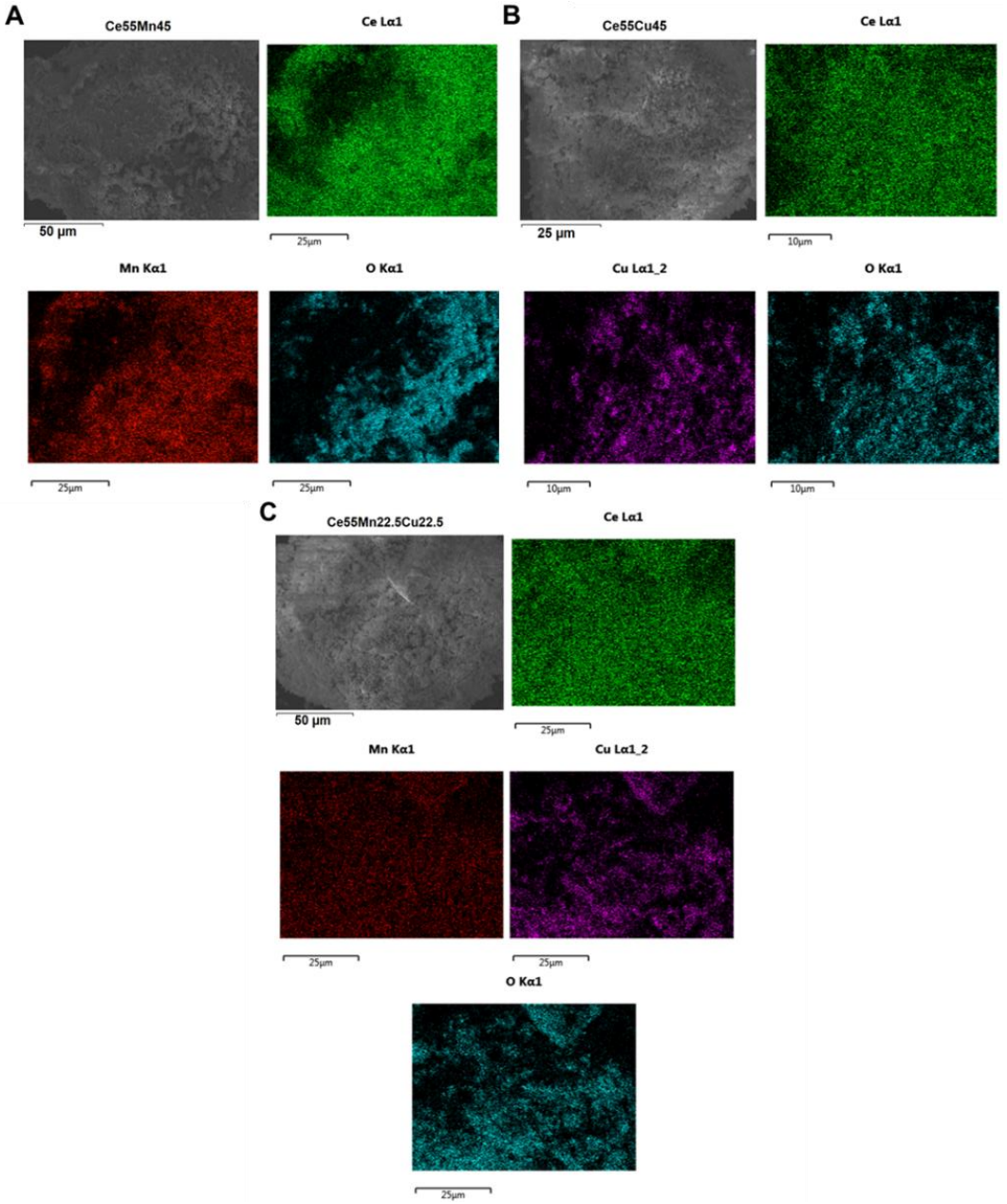

Figure 3.4 EDS element maps of the (A) $Ce_{55}Mn_{45}$, (B) $Ce_{55}Cu_{45}$ and $Ce_{55}Mn_{22.5}Cu_{22.5}$ catalysts. Reprinted from (Marin Figueredo et al., 2020).

tes. The ternary $Ce_{95}Mn_{2.5}Cu_{2.5}$ and $Ce_{85}Mn_{7.5}Cu_{7.5}$ exhibited small agglomerates and, as well, the formation of compact structures with noticeable grain boundaries. In fact, the observed non-porous structure of the ternary oxides confirms their low S_{BET}. The micrograph of the CuO catalyst evidenced the formation of a compact

structure with reduced porosity. Instead, the image of the Mn_2O_3 catalyst evidenced the presence of small pores distributed over the internal and external surface.

Element maps were carried out by means of EDS technique for the catalysts with the highest loading (45 at.%) of foreign metals (see Figure 3.4). The analyses, carried out over a set of planar zones, evidenced that the analyzed elements are distributed uniformly over the catalytic surface. Moreover, the technique was used for estimating the atomic composition of the mixed oxide catalysts, see Table 3.2. The EDS experimental results evidence a fair agreement with the nominal loading of the foreign metal(s) in the catalysts.

3.3 Temperature-programmed analyses (H_2-TPR and O_2-TPD)

The reducibility analyses under a flow of H_2 (5 vol.% in Ar) carried out over the synthesized catalysts are summarized in Figure 3.5. The first reduction signal of the CeO_2 appeared at ca. 300 °C. As a whole, an early reduction signal was observed, along with a reduction peak with a maximum intensity at 492 °C. As reported in the literature, the reduction signal occurring at high temperature is be attributed to the reduction of Ce species. On the other hand, the signal appeared at lower temperature is ascribed to surface oxygen species (Guo & Zhou, 2016; Marco Piumetti, Bensaid, Andana, Russo, et al., 2017). Moreover, the signal occurred above 600 °C can be assigned to the reduction of cerium species located in the bulk.

In accordance with the literature, the reduction profile of the CuO particles evidenced a single peak with a maximum signal located at 266 °C (George Avgouropoulos & Ioannides, 2003; Delimaris & Ioannides, 2009). Instead, the profile obtained for the Mn_2O_3 sample evidenced the occurrence of two overlapping reduction peaks. The signal occurred at lower temperature (at ca. 325 °C) was ascribed to the following reduction step: $Mn_2O_3 \rightarrow Mn_3O_4$, while a second reduction peak takes place at higher temperature (ca. 444 °C). The deconvolution carried out to the reduction profile evidenced that a total H_2 consumption equivalent to 9.22 mmol g^{-1} took place. Consistently, the consumption is higher than the theoretical amount needed in order to reduce pure Mn_2O_3, thus 6.33 mmol g^{-1}. As well, such H_2 consumption is lower respect to the amount required if all the manganese was present in the sample as Mn^{4+} (11.50 mmol g^{-1}). This evidences that the reduction signal is ascribed to the reduction of both Mn^{3+} and Mn^{4+} species (the presence of the latter confirmed by means of XPS analyses). Consistently, and according to the literature, the steps involved in the reduction of the Mn_2O_3 are:

$MnO_2 \rightarrow Mn_2O_3 \rightarrow Mn_3O_4 \rightarrow MnO$ (Kapteijn, Singoredjo, Andreini, & Moulijn, 1994; Marco Piumetti, Fino, et al., 2015).

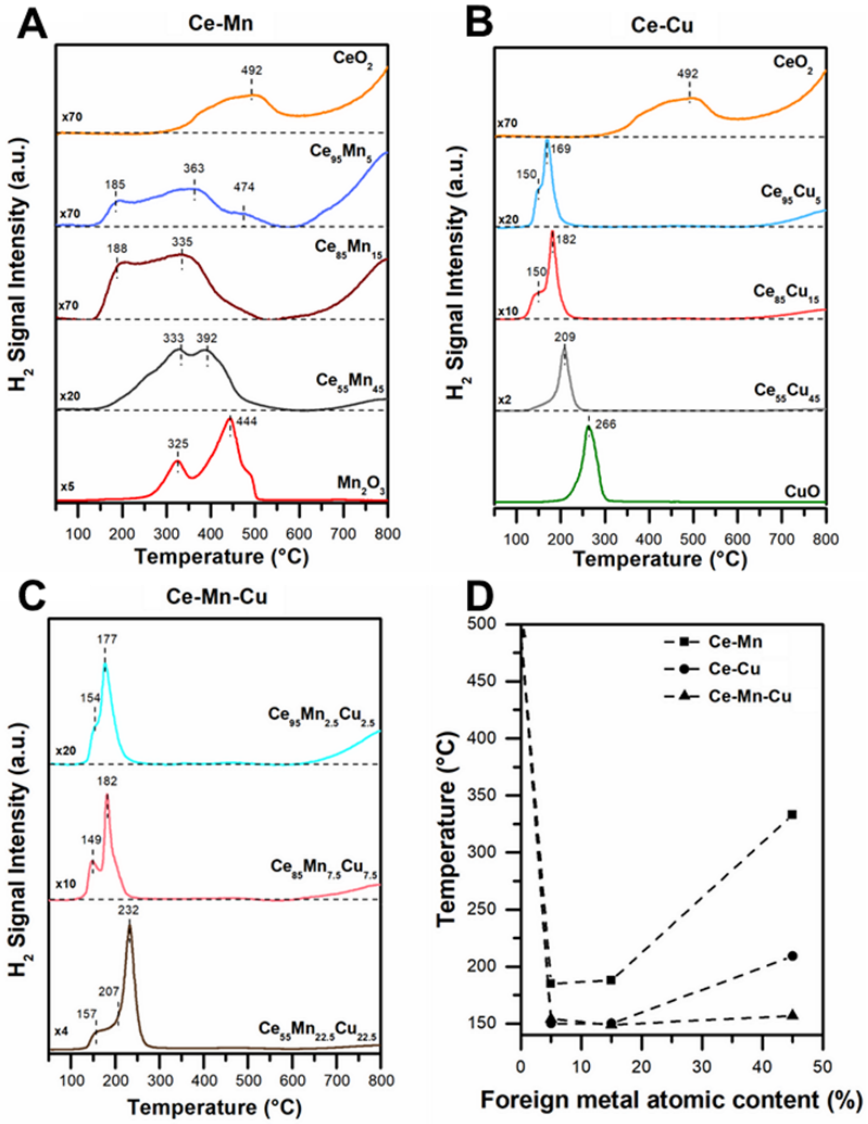

Figure 3.5 Reduction profiles of the (A) Ce-Mn, (B) Ce-Cu and (C) Ce-Mn-Cu sets of catalysts, obtained during H_2-TPR analyses. (D) Low-temperature reduction trend of the synthesized catalysts. Reprinted from (Marin Figueredo et al., 2020).

The reduction profiles of the Ce-Mn catalysts (see Figure 3.5, section A) evidence the presence of contemporary reduction peaks at low temperature. As a whole, it was observed that the reducibility of the samples (in terms of H_2 consumption) improves when the content of Mn in the catalyst is higher. Considering the reduction profiles of the $Ce_{95}Mn_5$ and the $Ce_{85}Mn_{15}$, the improved

low-temperature reducibility (main-peak shifting from 492 °C to 185 °C) highlights the enhancement caused by the insertion of Mn in ceria's lattice. It was observed that the reduction profile of the $Ce_{55}Mn_{45}$ changed, compared to the other binary Ce-Mn catalysts. Moreover, an increased H_2 consumption was observed, thus suggesting that the MnO_x species present in the catalyst could be interacting with ceria.

The reduction signal obtained during the H_2-TPR of the binary Ce-Cu catalysts is summarized in section B, Figure 3.5. It is noteworthy that the presence of Cu in the prepared catalysts enhances their reducibility at lower temperatures compared to the parent CeO_2. Consistently, the reduction profiles of the $Ce_{85}Cu_{15}$ and the $Ce_{95}Cu_5$ achieved two signal maxima at 150 °C and 182 °C (169 °C for the catalyst containing the lowest amount of Cu). In accordance with the literature, the signal occurring at the lower temperature was assigned to Cu species located in the lattice and interacting with Ce (Ce-O-Cu), while the one located at higher temperature can be attributed to CuO_x clusters that are highly dispersed and interacting with CeO_2 (George Avgouropoulos & Ioannides, 2003; Guo & Zhou, 2016; Y. Li, Fu, & Flytzani-Stephanopoulos, 2000; Marco Piumetti, Bensaid, Andana, Russo, et al., 2017). Instead, the signal harvested for the $Ce_{55}Cu_{45}$ catalyst revealed the appearance of an additional reduction peak at higher temperature. Such signal was attributed to the reduction of crystalline CuO, which was formed due to the segregation of copper oxide species during the synthesis (as confirmed by means of XRD analysis). In this sense, the reduction signal appeared at 209 °C (for the $Ce_{55}Cu_{45}$) was attributed to the reduction of the CuO clusters that are dispersed on CeO_2 (George Avgouropoulos & Ioannides, 2003; Guo & Zhou, 2016; Y. Li et al., 2000; Marco Piumetti, Bensaid, Andana, Russo, et al., 2017). Consistently, an increasing surface reducibility trend for the Ce-Cu system can be outlined, as a function of the amount of Cu, as follows: $Ce_{95}Cu_5 < Ce_{85}Cu_{15} < Ce_{55}Cu_{45}$.

Observing the reduction data harvested for the Ce-Mn-Cu catalysts (see section C, Figure 3.5), the shape of the reduction profiles is rather similar to those obtained for the binary Ce-Cu, i.e. they are characterized by two reduction signal maxima at ca. 150 °C and 180 °C. This behavior highlights that a substantial contribution to the overall reducibility of the catalysts is given by Cu species. Nevertheless, the manganese present in the Ce-Mn-Cu catalysts seems to induce a slight shift of the reduction signal assigned to copper species (H. Wang et al., 2017; Wöllner, Lange, Schmelz, & Knözinger, 1993). The reduction signals harvested for the $Ce_{85}Mn_{7.5}Cu_{7.5}$ and the $Ce_{95}Mn_{2.5}Cu_{2.5}$ were ascribed to: the reduction of isolated

Cu species that interact with cerium and manganese in the lattice (at 149 °C and 154 °C), and to the reduction of dispersed clusters of CuO_x that interact with the mixed oxide (at 177 °C and 182 °C). The reduction profile of the $Ce_{55}Mn_{22.5}Cu_{22.5}$ evidence the contemporary occurrence of various reduction peaks, thus complicating the analysis of the reduction signal. The reduction peak centered at ca. 157 °C was ascribed to isolated Cu species, which occurrence could be increased due to the presence of manganese in the catalyst. Instead, the signal occurring at ca. 207 °C can be ascribed to the reduction of both CuO_x clusters and the copper-manganese spinel ($Cu_{1.5}Mn_{1.5}O_4$), interacting with CeO_2. Moreover, the reduction signal occurring at 232 °C was assigned to CuO species.

The low-temperature reduction trend of the catalysts (reported in section D, Figure 3.5) puts a light in the probable key role played by the foreign metals present in the mixed oxide catalysts. It highlights that the insertion of manganese or copper inside CeO_2 enhances the reduction at low temperatures, i.e. it improves the surface reducibility. Remarkably, the catalysts containing foreign metal content of 5 and 15 at.%, evidenced reduction peaks at the lowest temperature value (ca. 150 °C). In fact, this outcome was also noticed in terms of H_2 consumption and may be correlated to the presence of Mn/Cu inside ceria's lattice, i.e. the formation of solid solutions. Nevertheless, the reduction occurred at higher temperatures when the loading of foreign metals was higher, as a consequence of the segregated Cu and Mn oxides present in the catalyst (as demonstrated via XRD analyses).

Interestingly, the deconvolution of the reduction profiles demonstrated the participation of ceria in the reduction process. Consistently, Table 3.3 summarizes the total H_2 consumption of the synthesized catalysts during the H_2-TPR analyses. Moreover, Table 3.3 includes the amount (%) of Ce^{4+} species that are reduced during the TPR, considering the initial oxidation states of Cu and Mn as +2 and 3+ (respectively), and the final reduced species as Cu^0 and Mn^{2+}. The results evidenced that a higher overall H_2 consumption takes place, compared to the stoichiometric H_2 uptake required for reducing the amount of Cu and/or Mn present in the catalyst. Consistently, the estimated amount of Ce^{4+} species seems to be enhanced when the amount of foreign metal(s) in the catalyst is higher, indicating an improved participation or role of ceria during the reduction process. In this sense, the results highlight the positive effect of Mn and Cu on enhancing the reducibility of CeO_2, probably by means of interactions taking place between the oxide phases present in the catalyst.

Table 3.3 Consumption of H_2 of the catalysts occurred during the H_2-TPR analyses and amount of Ce^{4+} (%) reduced. Adapted from (Marin Figueredo et al., 2020)

Catalyst	H_2 consumption (mmol g_{cat}^{-1})	Reduced Ce^{4+} (%)
CeO_2	0.61	20.9
$Ce_{95}Mn_5$	0.62	16.9[a]
$Ce_{85}Mn_{15}$	1.14	28.3[a]
$Ce_{55}Mn_{45}$	3.09	77.2[a]
$Ce_{95}Cu_5$	0.73	12.9[b]
$Ce_{85}Cu_{15}$	1.70	22.9[b]
$Ce_{55}Cu_{45}$	5.79	98.6[b]
$Ce_{95}Mn_{2.5}Cu_{2.5}$	0.61	4.7[c]
$Ce_{85}Mn_{7.5}Cu_{7.5}$	1.19	24.1[c]
$Ce_{55}Mn_{22.5}Cu_{22.5}$	3.96	56.6[c]
Mn_2O_3	9.22	-
CuO	17.34	-

[a] Reduced amount of Ce^{4+} (%) if the initial oxidation state of Mn is +3; [b] Reduced amount of Ce^{4+} (%) if the initial oxidation state of Cu is +2; [c] Reduced amount of Ce^{4+} (%) if the initial oxidation state of Mn and Cu are +3 and +2, respectively.

The profiles harvested during the O_2-TPD for the prepared catalysts analyses are summarized in Figure 3.6.

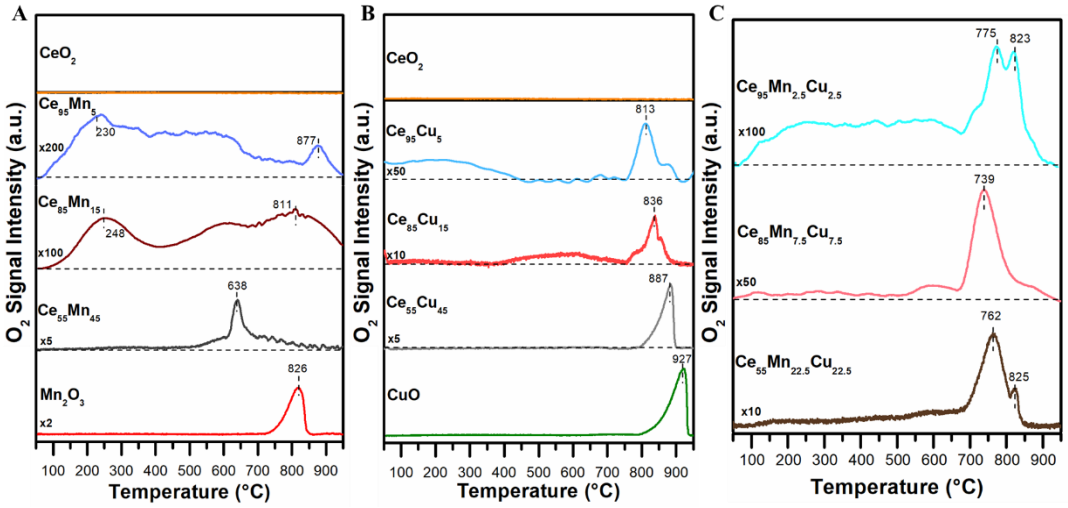

Figure 3.6 Desorption profiles of the (A) Ce-Mn, (B) Ce-Cu and (C) Ce-Mn-Cu sets of catalysts, obtained during O_2-TPD analyses. Reprinted from (Marin Figueredo et al., 2020).

The O_2 desorption signal harvested for the Ce-Mn set of catalysts (and of the parent Mn_2O_3) are included in section A of Figure 3.6. The Mn_2O_3 catalyst evi-

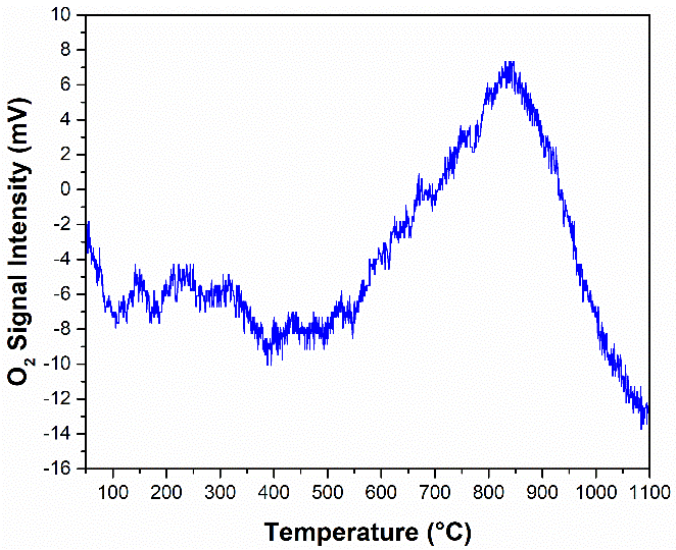

Figure 3.7 O_2 desorption profile of the CeO_2 catalyst pretreated for 30 min under a flow of O_2 at 750 °C. Reprinted from (Marin Figueredo et al., 2020).

denced a single-peak desorption signal centered at 826 °C. The amount of desorbed oxygen (ca. 1.09 mmol g^{-1}) was estimated by means of the integral area. The resulting value is in accordance with the theoretical amount of oxygen (1.06 mmol g^{-1}) that is released in the following reduction step: $Mn_2O_3 \rightarrow Mn_3O_4$.

Comparable values have been reported in the literature (Marco Piumetti, Fino, et al., 2015; Santos et al., 2010). Under the experimental conditions used, no relevant oxygen desorption could be harvested for the parent CeO_2. Therefore, in order to better study the O_2 desorption of CeO_2, the TPD analysis was carried out using the conditions described in the literature (Palmisano, Russo, Fino, Fino, & Badini, 2006). The profile resulting from the TPD was reported in Figure 3.7. The desorption signal observed at ca. 850 °C is corresponds to superficial oxygen species. The desorption profiles of the Ce-Mn set highlight that manganese improves the oxygen storage capacity of the catalyst. Accordingly, the literature reports that in binary Ce-Mn oxide systems, Ce promotes a higher oxidation state in Mn species at moderate temperatures (Imamura, Shono, Okamoto, Hamada, & Ishida, 1996). The desorption profiles of the Ce-Mn set of catalysts (see section A, Figure 3.6) evidenced rather complex behaviors. The signal observed below 400 °C is attributed to the desorption of chemisorbed oxygen (O_α) species. In fact, the complex desorption signal (multitude of peaks) in the low temperature range suggests an abundant amount of O_α species. On the other hand, the signal appeared at higher temperature is attributed to structural (lattice) oxygen (O_β) species (Liang,

Wu, Weng, & Xu, 2008). Particularly, the TPD profile of the $Ce_{55}Mn_{45}$ evidenced an intense signal located at ca. 638 °C attributed to the reduction of manganese species (Mn^{4+}). Instead, the desorption signal of the $Ce_{85}Mn_{15}$ and the $Ce_{95}Mn_5$ appeared above 800 °C, suggesting the contemporary presence of reduced manganese species (Mn^{3+} or Mn^{2+}) and Mn^{4+} cations. In fact, these results are in fair accordance with the results obtained in the XPS analyses (vide infra).

The aforementioned behavior agrees with TPD analyses carried out to commercial manganese oxides (MnO, Mn_2O_3 and MnO_2), as reported in Figure 3.8. For the MnO_2 sample, a release of oxygen (2.63 mmol g^{-1}) occurs at ca. 580 °C. The desorbed amount fairly agrees with the theoretical amount of oxygen (2.87 mmol g^{-1}) released during the following reduction step: $MnO_2 \rightarrow Mn_2O_3$. Instead, the integral area of the signal located at higher temperature (at ca. 811 °C) corresponded to a release of oxygen of 1.13 mmol g^{-1}. This amount of released oxygen coincides with the theoretical amount of oxygen that is released in the step: $Mn_2O_3 \rightarrow Mn_3O_4$ (1.06 mmol g^{-1}). Similarly, the TPD of the commercial Mn_2O_3 evidenced a single reduction signal at ca. 806 °C, and a consequent oxygen release of 1.13 mmol g^{-1}. This result highlights the range of temperatures (ca. 800 °C) at which the reduction of Mn^{3+} species may take place. Contrarily, the TPD profile of the MnO sample did not show desorption peaks. This suggests that the oxidation state of Mn^{2+} species remains unvaried during the TPD analysis.

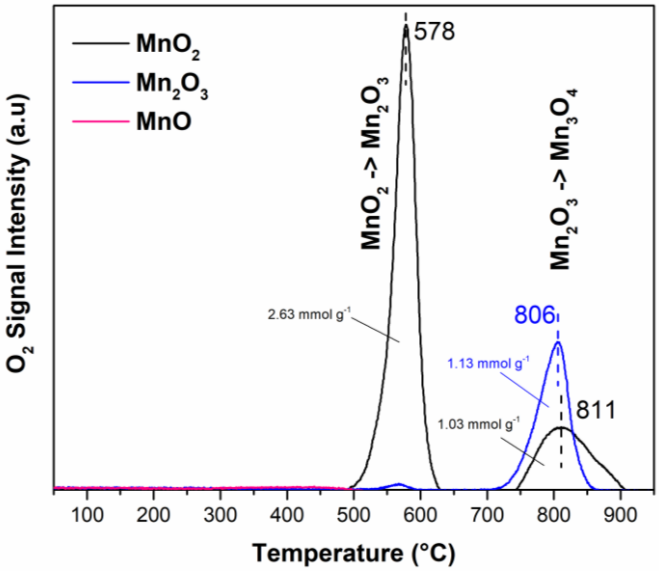

Figure 3.8 Desorption profiles of commercial manganese oxides during the O_2-TPD analyses. Reprinted from (Marin Figueredo et al., 2020).

The desorption profiles of the Ce-Cu set of catalysts (and of the parent CuO) are included in section B, Figure 3.6. The TPD profile of the parent CuO evidenced a single peak signal centered at ca. 927 °C. The integral area was evaluated, and corresponded to an oxygen release of 3.13 mmol g^{-1}. The calculated oxygen release agrees with the theoretical amount of oxygen released in the reduction step: CuO → Cu_2O (3.14 mmol g^{-1}). The desorption profiles of the mixed Ce-Cu oxides evidence the enhanced occurrence of O_α species according to higher amounts (at.%) of copper in the sample. Consequently, the presence of copper in the Ce-Cu binary oxide systems increased the population of chemisorbed oxygen species. Likewise, slightly higher amounts of O_β species seem to desorb from the catalysts when the copper atomic content is increased. Similar to the desorption profile of the parent CuO, a single peak signal was observed in the TPD of the $Ce_{55}Mn_{45}$. However, the latter signal occurred at a slightly lower temperature (ca. 887 °C) and achieved a lower signal intensity. Therefore, this suggests that the desorption signal can be attributed to the release of structural oxygen species from CuO_x phases, thus Cu^{2+} → Cu^+. Instead, the main desorption signals of the $Ce_{85}Cu_{15}$ and the $Ce_{95}Cu_5$ catalysts occurred at lower temperature and consisted in peaks of reduced intensity. This suggests that the lower the amount of Cu^{2+} species in mixed Ce-Cu oxide systems, the lower the temperature required for desorbing O_β species. Additionally, the wide signals that took place in the 400-700 °C range were attributed to the release of O_β from the mixed Ce-O-Cu system.

As reported in section C of Figure 3.6, the contemporaneous presence of Mn and Cu species in the ternary Ce-Mn-Cu system promotes significantly the desorption of chemisorbed O_α species. The signal appeared at ca. 750 °C and 823 °C were assigned to O_β species. Nevertheless, these intense signals cannot be assigned only to weakened metal-oxygen bonds in a ternary mixed oxide lattice. In fact, the desorption of oxygen from weakened Ce-O and Mn-O bonds occurs at similar temperatures. Furthermore, the release of oxygen from the mixed Ce-O-Cu lattice occurred as well in the same temperature region.

3.4 X-ray photoelectron spectroscopy

The harvested XPS spectra of the synthesized samples in the O 1*s* core level are included in section A, Figure 3.9. As a whole, three peak signals were observed for most samples. These peaks were assigned to different oxygen species. The signal located at lower binding energy (BE) thus at ca. 529.0–529.5 eV was ascribed to structural oxygen species (O_β species), thus lattice oxygen bonded to Ce (Platau,

Johansson, Hagström, Karlsson, & Hagström, 1977). Instead, the peaks centered at about 529.8 eV were attributed to the structural lattice-oxygen species bonded to Mn or to Cu (Biesinger, Lau, Gerson, & Smart, 2010; Biesinger et al., 2011). The signals appeared between 531.1 eV and 531.5 eV were attributed to oxygen species chemisorbed on the surface (O_α species), like O^-, or O_2^- and OH groups (Chen et al., 2017; Dupin, Gonbeau, Vinatier, & Levasseur, 2000). A signal of reduced intensity was observed at higher BE range (533.2-534.3 eV) in the XP spectra of the mixed oxides. This signal was ascribed to the presence of more electrophilic chemisorbed oxygen species (O_α), e.g. weakly adsorbed oxygen species (Deng, Dai, Lao, Shi, & Wang, 2015; Lin et al., 2018; Santos et al., 2010). The O_α/O_β ratio (see Table 3.4) was characterized by an increasing trend for the binary Ce–Mn catalysts. On the other hand, for the catalysts containing Cu (i.e. Ce–Cu and Ce–Mn–Cu) the same ratio seems to decrease and reach a minimum at the foreign metal content of 15 at.%. Compared to the parent CeO_2, a higher abundance of O_α species was observed in the mixed oxide samples, however, the parent Mn_2O_3 and CuO evidenced higher amounts of these chemisorbed species. The relative abundances of O_α (observed by means of XPS analyses) among the mixed oxide catalysts evidenced a trend that coincides with the oxygen released during the O_2-TPD analyses below 400 °C.

Table 3.4 Relative abundances (at.%) of oxygen species as derived from the analysis of the O 1*s* XPS spectra. Reprinted from (Marin Figueredo et al., 2020)

Catalyst	**O_α, OH BE (eV)**	**O_α (at.%)**	**O_β BE (eV)**	**O_β (at.%)**	**O_α/O_β**
CeO_2	531.1 ; 533.6	26.2	529.2	73.8	0.35
$Ce_{95}Mn_5$	531.4 ; 533.8	30.9	529.1	69.1	0.45
$Ce_{85}Mn_{15}$	531.3 ; 533.5	33.0	529.1	66.0	0.50
$Ce_{55}Mn_{45}$	531.3	39.4	529.5	60.6	0.65
$Ce_{95}Cu_5$	531.2 ; 533.8	39.5	529.0	60.5	0.65
$Ce_{85}Cu_{15}$	531.3 ; 534.3	30.0	529.2	70.0	0.43
$Ce_{55}Cu_{45}$	531.3 ; 533.2	33.6	529.4	66.4	0.51
$Ce_{95}Mn_{2.5}Cu_{2.5}$	531.3 ; 533.7	29.3	529.1	70.7	0.41
$Ce_{85}Mn_{7.5}Cu_{7.5}$	531.3 ; 533.4	28.0	529.1	72.0	0.39
$Ce_{55}Mn_{22.5}Cu_{22.5}$	531.4 ; 533.7	33.0	529.4	67.0	0.49
Mn_2O_3	531.1	44.2	529.8	55.8	0.79
CuO	531.5	47.2	529.8	52.8	0.90

The harvested Ce 3*d* core level spectra are reported in section B, Figure 3.9. As a whole, the spectra comprise a series of spin–orbit doublets “V” and “u”. Correspondingly, the doublets are related to the $3d_{5/2}$ and $3d_{3/2}$ regions. In the present work, the average BE positions of these signals are the following: V_0 at 882.0 eV; V_1 at 884.6 eV; V_2 at 888.4 eV; V_3 at 898.0 eV; and u_0 at 900.6 eV; u_1 at 902.0 eV; u_2 at 907.1 eV and u_3 at 916.3 eV. These signals can be used in order to

estimate the abundance of the Ce^{4+} and the Ce^{3+} species over the solid's surface. Accordingly, the doublets (V_0, u_0), (V_2, u_2) and (V_3, u_3) are assigned to Ce^{4+} species, instead, the doublet (V_1, u_1) is assigned to Ce^{3+} species (Chen et al., 2017; Mullins, 2015). The calculated relative abundances of the Ce^{x+} species are summarized in Table 3.5. Compared to the parent CeO_2, an increased amount of Ce^{3+} species was observed in the mixed oxide catalysts. In fact, the insertion of the studied foreign metals (Mn and/or Cu) in the structure of CeO_2 can lead to a distortion of the fluorite framework. As a consequence, such distortion can enhance the abundancy of structural defects and, therefore, the formation of new Ce^{3+} sites (Chen et al., 2017; Dosa et al., 2018; Machida, Uto, Kurogi, & Kijima, 2000).

Table 3.5 Relative abundances (at.%) of Ce^{x+} species as derived from the Ce 3*d* core level XPS spectra deconvolution. Reprinted from (Marin Figueredo et al., 2020)

Catalyst	**Ce^{4+} (at.%)**	**Ce^{3+} (at.%)**	**Ce^{4+}/Ce^{3+}**
CeO_2	85.03	14.97	5.68
$Ce_{95}Mn_5$	71.96	28.04	2.57
$Ce_{85}Mn_{15}$	79.18	20.82	3.80
$Ce_{55}Mn_{45}$	78.78	21.22	3.71
$Ce_{95}Cu_5$	72.13	27.87	2.59
$Ce_{85}Cu_{15}$	74.08	25.92	2.86
$Ce_{55}Cu_{45}$	74.80	25.20	2.97
$Ce_{95}Mn_{2.5}Cu_{2.5}$	76.33	23.67	3.22
$Ce_{85}Mn_{7.5}Cu_{7.5}$	78.12	21.88	3.57
$Ce_{55}Mn_{22.5}Cu_{22.5}$	77.65	22.35	3.47

The harvested Mn 2*p* XP spectra are included in section C, Figure 3.9. Spin orbit signals corresponding to the $2p_{1/2}$ level appeared in the BE range 647.5–657.5 eV. Instead, the signal corresponding to the $2p_{3/2}$ level occurred at about 638.5-647.5 eV. As evidenced in the literature, the deconvolution of the latter signal, thus the $2p_{3/2}$, may allow to estimate the relative abundances of the manganese species (Mn^{4+}, Mn^{3+} and Mn^{2+}) present over the surface of the sample (Biesinger et al., 2011; Marco Piumetti, Fino, et al., 2015). As expected, Mn^{3+} was the predominant specie present in the parent Mn_2O_3. The relative abundances of the Mn^{x+} species as derived from the deconvolution of the Mn 2*p* spectra are summarized in Table 3.6. As a whole, it was observed that the abundances of Mn^{x+} species varied according to the loading of Mn in the catalyst. Among the studied samples, the $Ce_{55}Mn_{45}$ evidenced the highest amount of Mn^{4+} species. Instead, an increased amount of re-

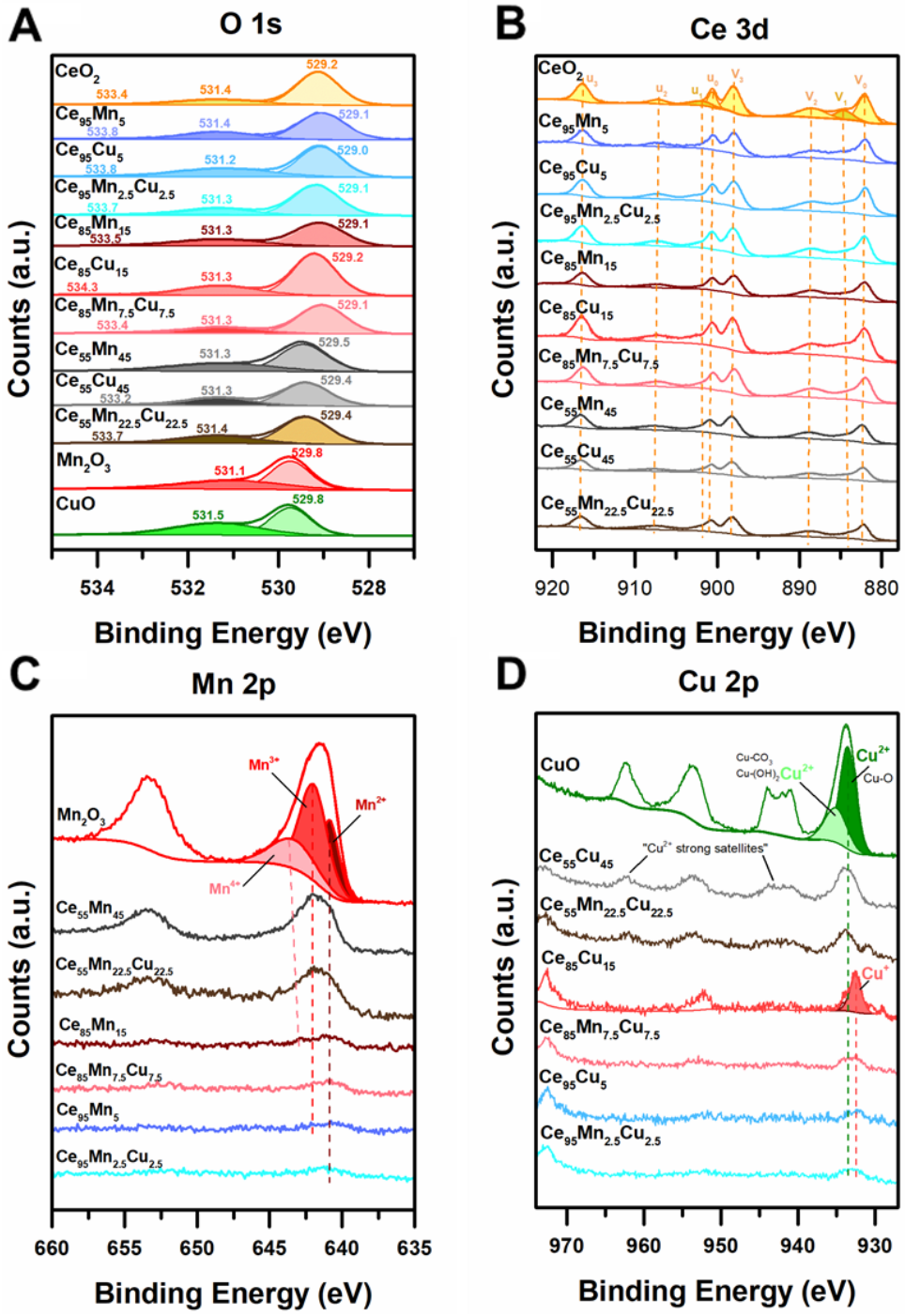

Figure 3.9 XPS powder catalysts spectra harvested in the O (1*s*), Ce (3*d*), Mn (2*p*) and Cu (2*p*) core level regions. Reprinted from (Marin Figueredo et al., 2020).

duced Mn^{2+} species was observed in the binary ($Ce_{95}Mn_5$ and $Ce_{85}Mn_{15}$) and ternary oxides ($Ce_{95}Mn_{2.5}Cu_{2.5}$ and $Ce_{85}Mn_{7.5}Cu_{7.5}$).

Table 3.6 Estimated relative abundances of Mn^{x+} species according to the deconvolution of the Mn 2*p* spectra. Reprinted from (Marin Figueredo et al., 2020)

Catalyst	Mn^{4+} BE (eV)	Mn^{4+} (at.%)	Mn^{3+} BE (eV)	Mn^{3+} (at.%)	Mn^{2+} BE (eV)	Mn^{2+} (at.%)	$\frac{Mn^{4+}}{Mn^{3+}}$	$\frac{Mn^{3+}}{Mn^{2+}}$
$Ce_{95}Mn_5$	-	-	642.2	26.15	640.4	73.85	-	0.35
$Ce_{85}Mn_{15}$	642.8	23.04	-	-	640.9	76.96	-	-
$Ce_{55}Mn_{45}$	642.9	36.23	641.9	49.65	640.7	14.12	0.73	3.52
$Ce_{95}Mn_{2.5}Cu_{2.5}$	-	-	-	-	641.1	100.00	-	-
$Ce_{85}Mn_{7.5}Cu_{7.5}$	-	-	641.6	51.41	640.4	48.59	0.00	1.06
$Ce_{55}Mn_{22.5}Cu_{22.5}$	642.6	30.70	642.2	29.40	640.8	39.89	1.04	0.74
Mn_2O_3	643.4	24.33	642.0	49.88	640.8	25.79	0.49	1.93

The spectra harvested in the Cu 2*p* core level are reported in section D, Figure 3.9. The spin orbit signal occurred between 930.0 eV and 940.0 eV is attributed to the $2p_{3/2}$ level. Instead, the signal appeared at about 950.0–960.0 eV belong to the $2p_{1/2}$ level. The literature reports that the deconvolution of the former signal and the eventual occurrence of shake-ups can be used to identify the Cu^{x+} species present over the surface of the sample (Biesinger et al., 2010; Kundakovic & Flytzani-Stephanopoulos, 1998; W. Liu & Flytzani-Stephanopoulos, 1995a). Accordingly, strong Cu^{2+} satellites at ca. 942.5 and 962.5 eV were identified for the parent CuO. As a consequence, the major peak in the $2p_{3/2}$ region was assigned to Cu^{2+}. The aforementioned signal can be deconvoluted into two contributions, as follows: the first centered at 933.6 eV, attributed to Cu bonded to lattice oxygen (Cu–O), the second centered at 935.2 eV and assigned to the copper hydroxide and/or copper carbonate species (Biesinger et al., 2010; Kundakovic & Flytzani-Stephanopoulos, 1998). The spectra of the $Ce_{55}Cu_{45}$ and $Ce_{55}Mn_{22.5}Cu_{22.5}$ suggest the predominance of Cu^{2+} species, bonded either to lattice oxygen or to carbonate/hydroxyl groups. Nevertheless, the spectra of the other mixed oxides containing copper evidenced a shift of the $2p_{1/2}$ signal toward lower a BE value (ca. 932.5 eV). This result indicates the enhanced presence of reduced Cu^{+} species over the surface of the catalyst. The literature reports that the reduction of Cu species is most likely induced due to interactions that take place among the metal cations (Biesinger et al., 2010; Marco Piumetti, Bensaid, Andana, Russo, et al., 2017).

Table 3.7 Surface element atomic composition of the mixed oxide catalysts as derived from the EDS technique. Differences on Mn and Cu at.% compositions derived by means of XPS and EDS techniques. Reprinted from (Marin Figueredo et al., 2020)

Catalyst	O (at.%)	Ce (at.%)	Cu (at.%)	Mn (at.%)	$\Delta Cu_{(XPS-EDS)}$ (at.%)	$\Delta Mn_{(XPS-EDS)}$ (at.%)
$Ce_{95}Mn_5$	76.8	20.9	-	2.3	-	0.5
$Ce_{85}Mn_{15}$	80.7	15.6	-	3.6	-	-0.1
$Ce_{55}Mn_{45}$	73.3	14.1	-	12.6	-	0.5
$Ce_{95}Cu_5$	75.2	19.4	5.4	-	3.3	-
$Ce_{85}Cu_{15}$	75.4	17.0	7.6	-	1.1	-
$Ce_{55}Cu_{45}$	73.8	11.2	15.0	-	-5.7	-
$Ce_{95}Mn_{2.5}Cu_{2.5}$	77.6	13.4	5.3	3.7	2.7	2.7
$Ce_{85}Mn_{7.5}Cu_{7.5}$	75.4	19.5	2.0	3.1	-0.7	0.1
$Ce_{55}Mn_{22.5}Cu_{22.5}$	69.3	11.3	12.4	7.0	1.1	-1.7

The atomic compositions of the elements in the catalysts (according to the XPS analyses) are reported in Table 3.7. As a whole, the elemental composition results obtained via XPS analyses seem to fairly agree with the data from EDS analyses, Table 3.7. Therefore, the results suggest the occurrence of a good dispersion of Mn and Cu in both the surface and bulk of the catalysts. Accordingly, the relative differences between the compositions obtained by means of both techniques (reported as ΔCu and ΔMn) are low. In this sense, an enrichment or diminution of Mn and/or Cu in the surface or the bulk phase cannot be stated.

3.5 Catalytic activity: Powders

3.5.1 Oxidation of propylene

The conversions (%) of propylene (sections A, C and E) and ethylene (sections B, D and F) during the catalytic tests for the synthesized catalysts are summarized in Figure 3.10. The non-catalytic conversion of propylene evidenced a light-off temperature at ca. 300 °C. In this sense, when no catalyst is present, the maximum propylene conversion achieved is approximately 4% at 350 °C. When the catalyst is present in the reactor, the oxidation reaction of C_3H_6 took place lower temperatures. Consistently, most catalysts achieved a complete conversion of propylene below 350 °C.

The catalytic performance of the catalysts, reported in terms of $T_{10\%}$, $T_{50\%}$ and $T_{90\%}$, i.e., the temperatures for completing 10%, 50% and 90% conversion of propylene, are included in Table 3.8. Moreover, the propylene oxidation reaction

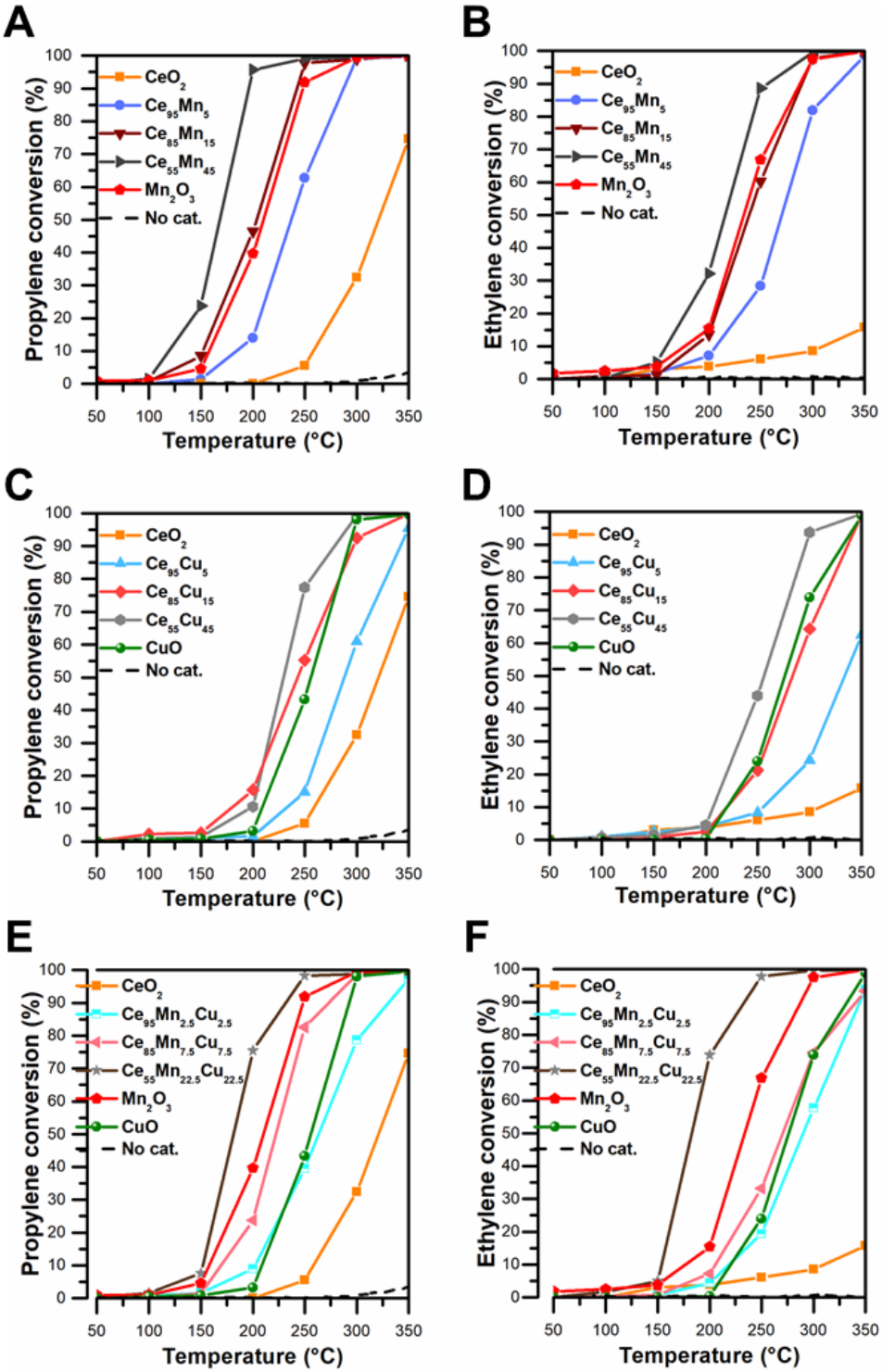

Figure 3.10 Conversions (%) of propylene (A, C, E) and ethylene (B, D, F) as a function of the temperature over the synthesized catalysts. Reprinted from (Marin Figueredo et al., 2020).

rate was reported. According to their $T_{x\%}$, the parent oxides evidenced the following increasing catalytic performance trend: CeO_2 < CuO < Mn_2O_3. Interestingly, better catalytic performances in propylene oxidation were observed when the foreign metals (Mn/Cu) are present in the catalyst. Thus highlighting that possible interactions between could be taking place between Ce, Mn and/or Cu in the mixed oxide structure. Moreover, beneficial interactions could also occur between the different oxide phases present on the surface of the catalyst (as observed by means of XRD analyses).

Table 3.8 Catalytic performances of the synthesized catalysts. Reprinted from (Marin Figueredo et al., 2020)

Catalyst	C_3H_6 oxidation				C_2H_4 oxidation			
	$T_{10\%}$ (°C)	$T_{50\%}$ (°C)	$T_{90\%}$ (°C)	r^a (µmol h^{-1} m^{-2})	$T_{10\%}$ (°C)	$T_{50\%}$ (°C)	$T_{90\%}$ (°C)	r^b (µmol h^{-1} m^{-2})
CeO_2	261	322	-	0.00	310	-	-	0.50
$Ce_{95}Mn_5$	193	237	283	0.11	210	270	313	0.32
$Ce_{85}Mn_{15}$	153	204	240	0.76	192	239	286	0.31
$Ce_{55}Mn_{45}$	130	168	194	3.54	163	216	252	1.21
$Ce_{95}Cu_5$	240	288	342	0.06	260	334	-	0.20
$Ce_{85}Cu_{15}$	186	243	295	0.34	227	283	337	0.26
$Ce_{55}Cu_{45}$	199	229	270	0.30	210	256	295	0.30
$Ce_{95}Mn_{2.5}Cu_{2.5}$	203	264	329	0.73	227	290	344	1.19
$Ce_{85}Mn_{7.5}Cu_{7.5}$	178	222	262	0.12	208	270	340	0.29
$Ce_{55}Mn_{22.5}Cu_{22.5}$	153	181	223	1.55	156	183	225	2.75
Mn_2O_3	161	210	248	1.26	190	233	283	1.09
CuO	212	257	290	3.04	227	276	330	1.10

[a] Propylene reaction rates, calculated at 150 °C, [b] Ethylene reaction rates, calculated at 160 °C

The insertion of Mn and/or Cu atoms inside the structure of CeO_2 may promote the occurrence of oxygen defects. As a consequence, the mobility of lattice oxygen can be enhanced, leading to an improved reducibility of the catalyst, as evidenced by means of TPR analyses. Noteworthy, an enhancement of both the catalytic performance and the surface reducibility were observed when the foreign metal loading increased. This achievement confirms the beneficial effect of substituting Ce species with transition metals. Instead, XRD analyses evidenced that the size of crystallites was decreased when the metal loading was higher. Remarkably, a good correlation was observed between the catalytic performances of the mixed oxide

catalysts and their size of crystallites. Accordingly, the lower the size of crystallites, the better the catalytic performances.

The calculated reaction rates (estimated at 150 °C) highlight the improved catalytic activity of the mixed oxides compared to the parent CeO_2 and, occasionally, better than Mn_2O_3 and CuO. The catalyst that exhibited the best catalytic performance in the oxidation of propylene, i.e. the $Ce_{55}Mn_{45}$, carried out the complete C_3H_6 conversion at ca. 250 °C. The remarkable catalytic performance is probably the result of phase interactions taking place among MnO_x and CeO_x that, in turn, further improve the redox ability of the aforementioned catalyst. Therefore, the increasing overall catalytic performance trend for the mixed oxide systems can be outlined, as follows: Ce–Cu < Ce–Mn–Cu < Ce–Mn.

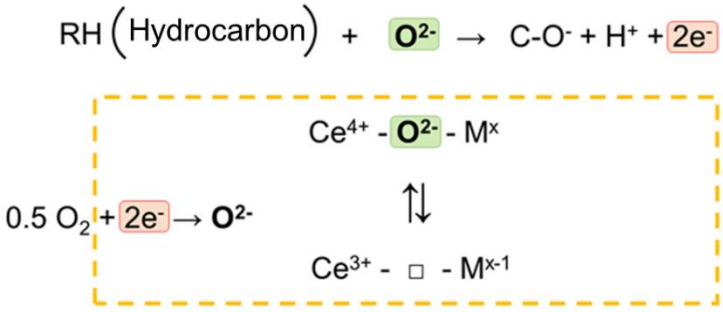

Figure 3.11 Redox cycle occurring in ceria-based catalysts, where M^x = foreign metal ; □ = oxygen vacancy. Adapted from (Marin Figueredo et al., 2020).

The catalytic results achieved, for the first time to our knowledge, highlight that the presence of Mn species in mixed-ceria systems synthesized by means of the SCS technique can enhance the total oxidation of C_3H_6.

The mechanism for the propylene oxidation reaction over metal oxide catalysts has been discussed in the literature as follows: firstly, the VOC molecule is adsorbed on the surface of the catalyst and, secondly, a symmetric allylic intermediate is formed due to the occurrence of the H-abstraction. Afterwards, the oxidation takes place after the release of structural (lattice) oxygen (O^{2-}), that leads to the formation of an allyl alkoxide intermediate. Additional H-abstraction occurs, and the formation of an aldehyde takes place after the formation of the carbonyl bond (Reitz & Solomon, 1998). Considering the oxidation of VOCs over ceria-based systems, the reaction mechanism most likely takes place via the Mars–van Krevelen-type mechanism (see the scheme reported in Figure 3.11, adapted from (Marco Piumetti, Bensaid, Andana, Russo, et al., 2017)). Nevertheless, the con-

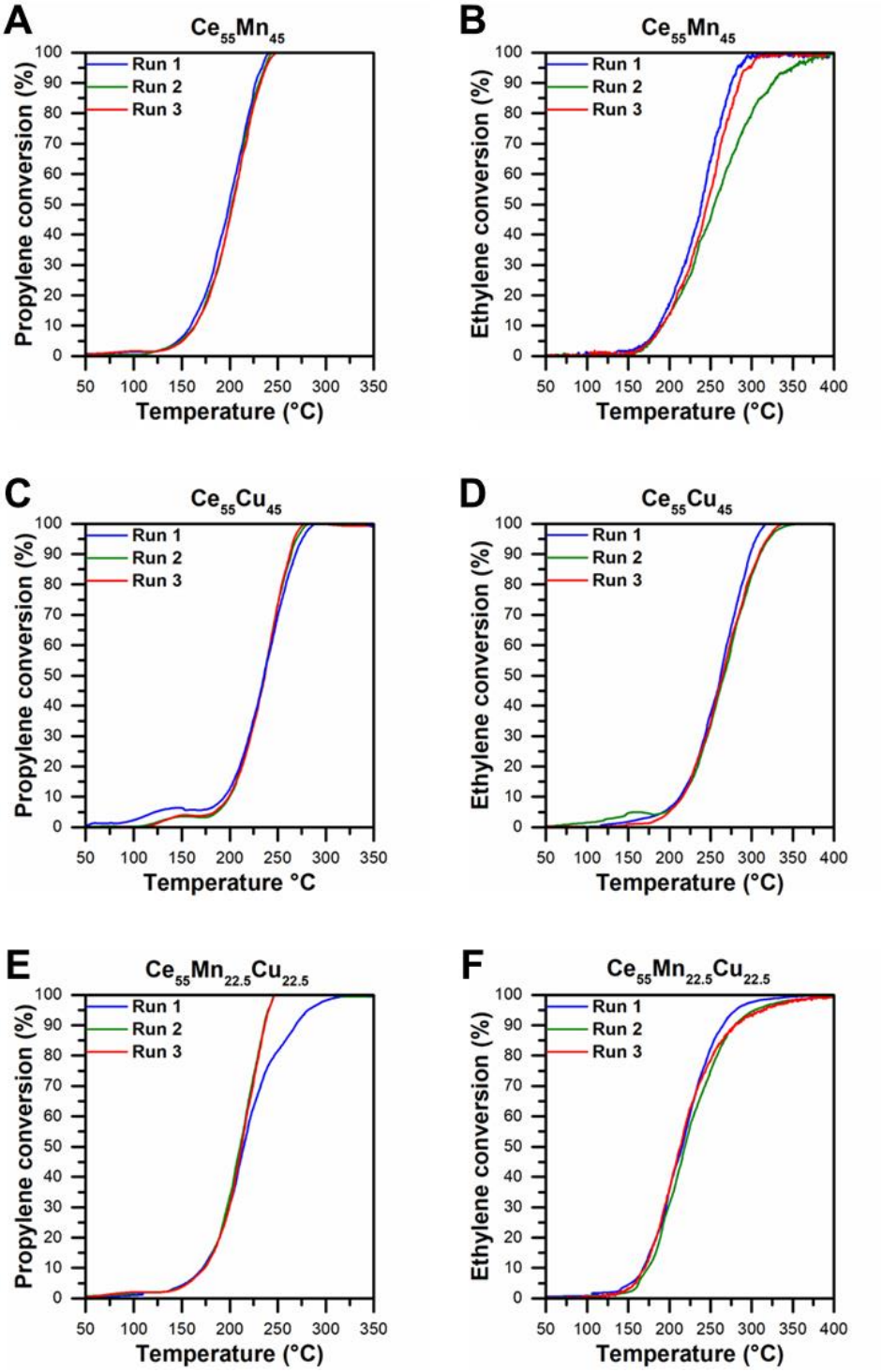

Figure 3.12 Catalytic activity reproducibility study for the (A, C, E) C_3H_6 and (B, D, F) C_2H_4 oxidation reactions over the $Ce_{55}Mn_{45}$, $Ce_{55}Cu_{45}$ and the $Ce_{55}Mn_{22.5}Cu_{22.5}$ samples. Reprinted from (Marin Figueredo et al., 2020).

junction of abundant surface-weakly-bonded oxygen species and the occurrence of spillover phenomena can promote the oxidation reaction of adsorbed organic molecules (Santos, Pereira, Órfão, & Figueiredo, 2009; Wood, Wise, & Yolles, 1969) Therefore, this scenario may lead to an overall enhancement of the catalytic activity.

Catalytic stability tests were carried out for the propylene oxidation reaction over the most promising catalysts, thus the $Ce_{55}Cu_{45}$, $Ce_{55}Mn_{22.5}Cu_{22.5}$ and the $Ce_{55}Mn_{45}$ catalysts (see Figure 3.12). As a whole, reproducible catalytic performances were obtained after three catalytic runs for all the catalysts. The conversion observed at ca. 150 °C during the tests of the $Ce_{55}Cu_{45}$ was ascribed to a fast release of CO_x produced at low temperatures. Noteworthy, catalytic tests in presence of humidity (RH 100%) were performed over the most promising catalyst in propylene oxidation, i.e. the $Ce_{55}Mn_{45}$ (see section A of Figure 3.13). Though the catalyst exhibited worse performances for the oxidation reaction, stable catalytic performances were verified after consecutive catalytic tests. This indicates that mixed CeO_2 systems could be less performing under gaseous streams containing water. The worsened performance could be related to different causes, for example, local thermal phenomena in the particles of the catalyst, reduced accessibility of the active sites, etc.

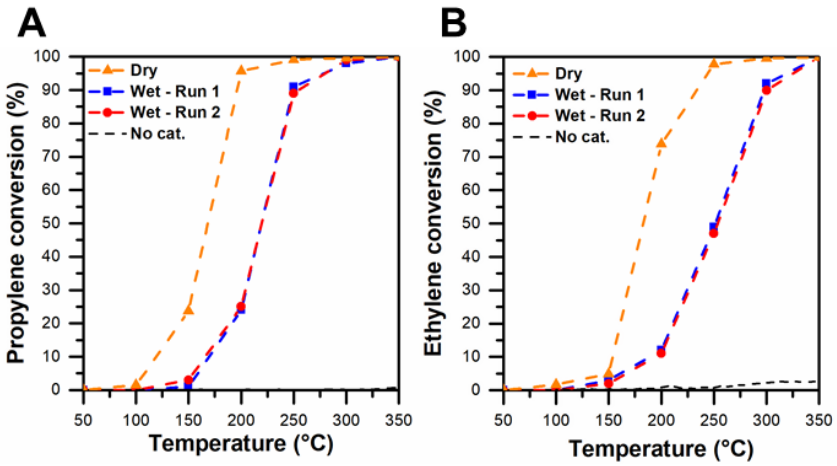

Figure 3.13 Conversion (%) of propylene over the (A) $Ce_{55}Mn_{45}$ catalyst and of ethylene over the (B) $Ce_{55}Mn_{22.5}Cu_{22.5}$ catalyst under wet-conditions. Reprinted from (Marin Figueredo et al., 2020).

Additionally, kinetic studies were carried out over the $Ce_{55}Mn_{45}$ catalyst for the C_3H_6 oxidation reaction at 150 °C (not reported for the sake of brevity), under different VOC inlet concentrations (200, 400, 600 and 900 ppm). The results

highlight that there is an increasing linear dependence of the C_3H_6 reaction rate (in μmol VOC h^{-1}) on the inlet concentration of the VOC.

3.5.2 Oxidation of ethylene

The performances observed during the ethylene catalytic oxidation screenings are shown in sections B, D and F of Figure 3.10. At the highest temperature studied (350 °C), a minimal conversion of ethylene (< 1%) could be observed in absence of a catalyst. The data reported in Table 3.8 evidences that higher reaction temperatures were required for the ethylene oxidation reaction, respect to those required for the abatement of propylene. This result remarks the higher stability of ethylene and thus its lower ability to be oxidized. Regarding the catalytic performance of the parent oxides (CeO_2, Mn_2O_3 and CuO), a similar trend (respect to propylene oxidation) was observed, as follows: CeO_2 < CuO < Mn_2O_3. Respect to the parent CeO_2, the mixed oxides evidenced improved performances according to the foreign metal loadings (as observed in the oxidation of propylene). Similar to the propylene oxidation reaction case, the possible interactions taking place between Ce, Cu and/or Mn species inside the catalysts or among the different phases seem equally beneficial for the oxidation of C_2H_4.

The $Ce_{55}Mn_{22.5}Cu_{22.5}$ and the $Ce_{55}Mn_{45}$ catalysts evidenced the best catalytic activities toward the oxidation of ethylene at 160 °C (see Table 3.8), achieving oxidation rates of 2.75 and 1.21 μmol h^{-1} m^{-2}, respectively. Accordingly, the $Ce_{55}Mn_{22.5}Cu_{22.5}$ catalyst accomplished the total conversion of C_2H_4 at ca. 250 °C. As discussed previously (vide supra), this achievement is most likely related to interactions occurring among the various active phases present in the $Ce_{55}Mn_{22.5}Cu_{22.5}$ catalyst. The catalytic results achieved, for the first time to our knowledge, evidence that cerium-mixed oxides containing Mn and Cu species synthesized by means of the SCS technique can enhance the total oxidation of C_2H_4. As in the C_3H_6 oxidation reaction (and in many other VOC oxidations), the oxidation of C_2H_4 may be modelled via a redox-cycle mechanism (thus, the Mars–van Krevelen reaction mechanism). In this sense, surface oxygen species play a key role in the oxidation reaction. For the ethylene oxidation reaction mechanism, the literature reports that a mild oxidation occurs on the surface of CeO_2, leading to the formation of formate species as intermediates. Afterwards, the formate species are oxidized, forming CO and CO_2 (C. Li, Xin, & Guo, 1992; Njagi, Genuino, King'Ondu, Dharmarathna, & Suib, 2012).

In order to assess the stability of the catalytic performance for C_2H_4 oxidation, reproducibility tests were carried out (consecutively) over the most promising catalysts, thus the $Ce_{55}Mn_{45}$, the $Ce_{55}Mn_{22.5}Cu_{22.5}$ and the $Ce_{55}Cu_{45}$ (see sections B,

D and F of Figure 3.12). The complete conversion of ethylene over the catalysts was verified after three catalytic runs at 350 °C.

As reported for the abatement of C_3H_6, the oxidation of C_2H_4 under wet-conditions was evaluated over the most promising catalyst, i.e. the $Ce_{55}Mn_{22.5}Cu_{22.5}$ (see section B of Figure 3.13). Though the catalyst exhibited worse performances for the oxidation reaction, comparable catalytic performances were verified after two consecutive catalytic tests in wet condition. This behavior remarks the findings observed for the propylene oxidation reaction (vide supra).

Moreover, a kinetic analysis was performed for the oxidation of ethylene over the $Ce_{55}Mn_{22.5}Cu_{22.5}$ catalyst at 160 °C (not reported for the sake of brevity), changing the VOC concentrations in the inlet (200, 400, 600 and 900 ppm). The test evidenced that the oxidation rate of ethylene does not change when the VOC inlet concentration varies. This finding suggests that the mechanism is zero order-type, respect to the ethylene.

3.6 Catalytic activity: Catalyzed monoliths

The most promising catalysts investigated in this work (the $Ce_{55}Mn_{45}$ and $Ce_{55}Mn_{22.5}Cu_{22.5}$) were deposited over SiC monoliths by means of an in-situ synthesis, in order to evaluate their applicability in industrial activities. A cross-sectional cut was performed over the $Ce_{55}Mn_{22.5}Cu_{22.5}$–SiC, in order to evidence a monolith's inner channel at different magnifications (see Figure 3.14). The micrograph on the right was acquired using the back-scattered electron mode. This allowed to evidence the catalytic washcoat in lighter color, while the SiC grains are observed in dark color. The central image is focused on the monolith's inner channel wall and shows the catalytic washcoat. This evidences that the in-situ synthesis formed effectively a thin catalytic layer with an average thickness of 326 nm. EDS maps were carried out (not reported for brevity), and a fairly homogeneous distribution of the elements over the catalytic surface was verified.

Consecutive catalytic tests (for ethylene or propylene oxidation reaction) carried out over the $Ce_{55}Mn_{45}$–SiC monolith are summarized in sections A and B of Figure 3.15. The monolith evidenced to be effective for the oxidation of the VOC probe molecules. The complete catalytic conversion of propylene to CO_2 was achieved at 500 °C, while for ethylene 600 °C were reached. Instead, the VOC conversion in absence of catalyst was observed at about 670 °C, and resulted mostly in the formation of CO (incomplete thermal oxidation). Moreover, the catalyzed monolith evidenced comparable catalytic performances during three consecutive

catalytic runs. This result highlights a good catalyst stability for the C_3H_6 and C_2H_4 oxidation reactions.

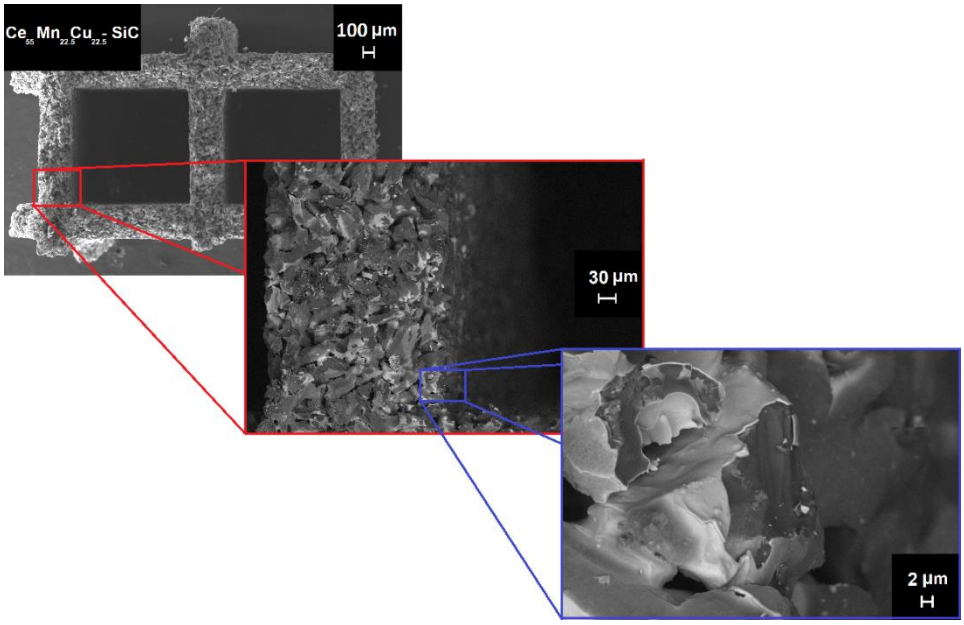

Figure 3.14 FESEM micrographs of the $Ce_{55}Mn_{22.5}Cu_{22.5}$–SiC at various magnifications. Reprinted from (Marin Figueredo et al., 2020).

Consecutive tests for the oxidation of the VOCs were carried out as well over the $Ce_{55}Mn_{22.5}Cu_{22.5}$–SiC monolith (see section C and D of Figure 3.15). The catalytic results evidenced that the VOC oxidation over the $Ce_{55}Mn_{22.5}Cu_{22.5}$–SiC took place mostly at temperatures lower than those required for the oxidation over the $Ce_{55}Mn_{45}$–SiC. Moreover, the $Ce_{55}Mn_{22.5}Cu_{22.5}$–SiC demonstrated stable catalytic performances after consecutive catalytic runs.

Stability time-on-stream (TOS) tests were carried out over the $Ce_{55}Mn_{45}$–SiC monolith (see sections A, B of Figure 3.16). For the TOS tests, the following isothermal conditions were investigated. (1) High temperature measurements, at 470 and 590 °C during the oxidation of propylene and ethylene, respectively (in order to nearly achieve the complete oxidation of the VOC). (2) Low temperature measurements, at about 372 and 471 °C for the oxidation of propylene and ethylene, respectively (in order to achieve ca. 50% conversion). Moreover, similar stability time-on-stream (TOS) tests were performed over the $Ce_{55}Mn_{22.5}Cu_{22.5}$–SiC under isothermal conditions (see sections C, D of Figure 3.16). As a whole, fairly stable conversions of C_3H_6 and of C_2H_4 were observed over 4 h of TOS. Consistently, the good performances suggest promising catalytic and structural stability of the monoliths. Additional long term-stability studies were carried out under isothermal

conditions for the $Ce_{55}Mn_{22.5}Cu_{22.5}$–SiC monolith for the oxidation VOCs (not reported for brevity). The aforementioned studies confirmed a good catalytic stability during two catalytic runs over 12 h TOS.

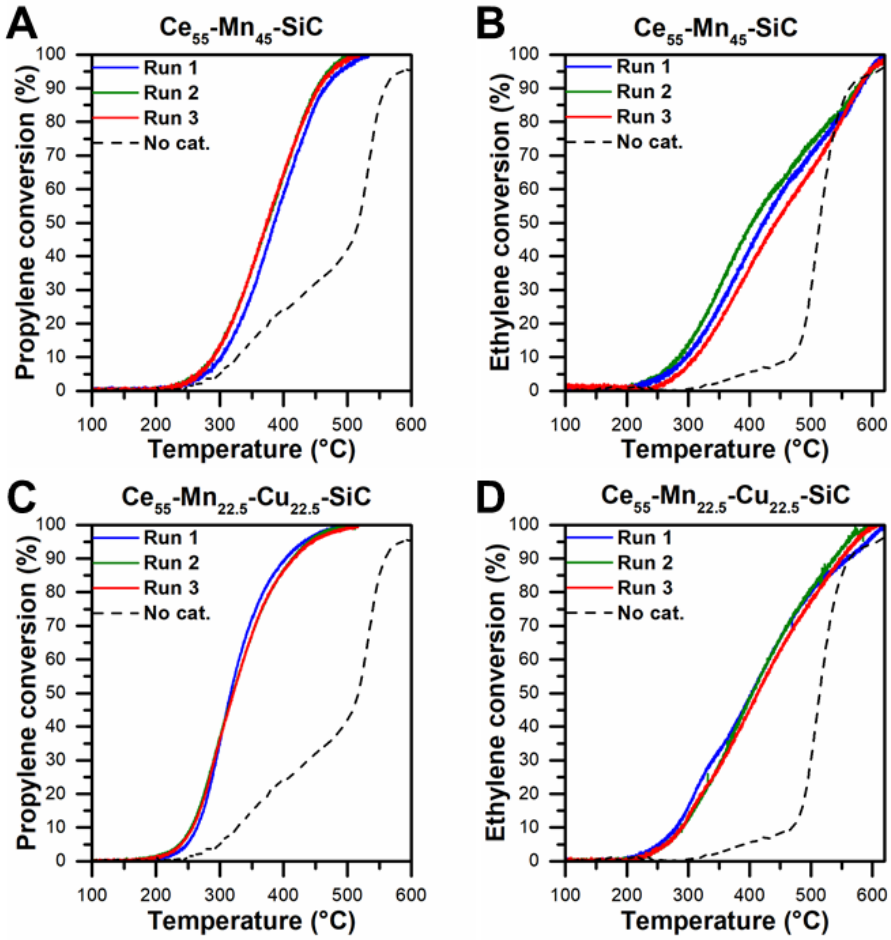

Figure 3.15 Conversions (%) of VOCs over (A, B) the $Ce_{55}Mn_{45}$–SiC and (C, D) the $Ce_{55}Mn_{22.5}Cu_{22.5}$–SiC monoliths. Reprinted from (Marin Figueredo et al., 2020).

Additional catalytic tests over the catalyzed monoliths were carried out under different operating conditions. Consistently, the experiments were performed varying the GHSV parameter (namely, 1000; 4335; 9000 and 19,000 h^{-1}) and were summarized in Figure 3.17. As a whole, after changing the GHSV parameter, the following trend was observed for the catalytic performances in VOC oxidation: the lower the GHSV the higher the VOC conversion. In fact, catalytic performances closer to those of the powder catalysts were observed at 1000 h^{-1}, due to the increased residence time of the VOCs inside the channels of the monolith. On the

other hand, the worst catalytic performances over the monoliths were observed at 19,000 h^{-1}.

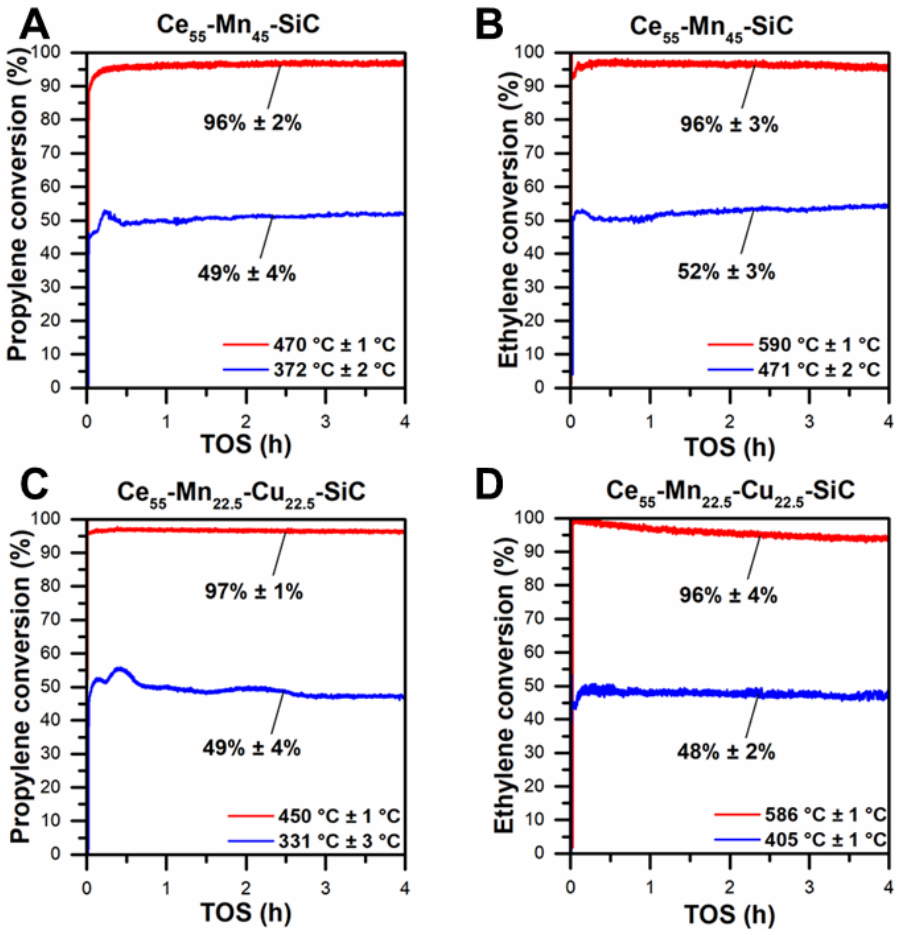

Figure 3.16 Conversions (%) of VOCs over (A, B) the $Ce_{55}Mn_{45}$–SiC and (C, D) the $Ce_{55}Mn_{22.5}Cu_{22.5}$–SiC monolith during time-on-stream catalytic tests. Reprinted from (Marin Figueredo et al., 2020).

Additional catalytic tests were carried out (at GHSV = 4335 h^{-1}) with the aim of evaluating the catalytic performance of the monoliths using the same W/F of the powder catalysts. The results evidence that worse catalytic performances are observed for the monoliths, compared to those of the powder samples (see Figure 3.10). Accordingly, the results suggest that parameters like a different catalytic set-up, and the fluid dynamics in the reactor play a key role on the overall catalytic activity (Maria R. Morales, Yeste, Vidal, Gatica, & Cadus, 2017; X. Zhang & Wu, 2016). Accordingly, these results highlight the possibility of developing scaled-up catalytic systems by means of the novel in-situ SCS, which allows to wash-coat the monoliths and to deposit cerium-mixed oxides.

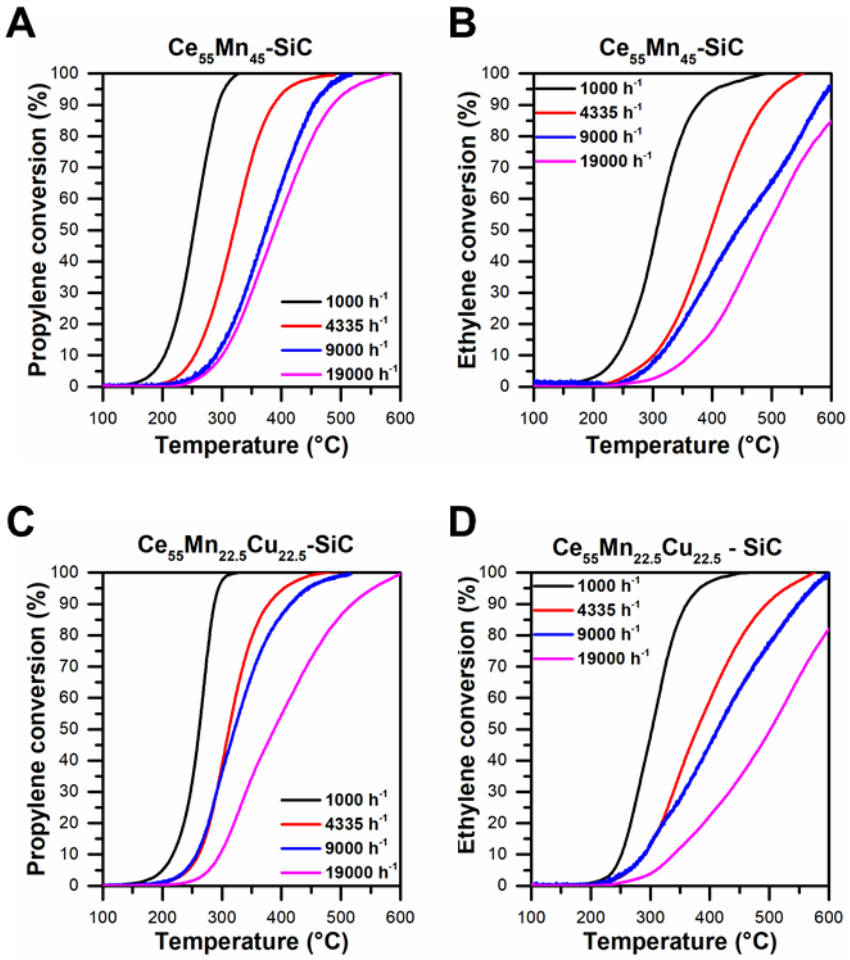

Figure 3.17 Conversions (%) of VOCs over (A, B) the $Ce_{55}Mn_{45}$–SiC and (C, D) the $Ce_{55}Mn_{22.5}Cu_{22.5}$–SiC monoliths using four different GHSV. Reprinted from (Marin Figueredo et al., 2020).

3.7 Conclusions

For this chapter, various sets of mixed oxide catalysts were prepared by means of the solution combustion synthesis (SCS). Specifically, two binary oxide sets (Ce-Mn and Ce-Cu) and one of ternary oxides (Ce-Mn-Cu). Each set comprised catalysts containing 5, 15 and 45 at.% of foreign metal loading. The catalytic results highlighted the $Ce_{55}Mn_{45}$ as the most performing catalyst for the propylene oxidation reaction, due to possible interactions taking place MnO_x and CeO_x species. Instead, the ternary $Ce_{55}Mn_{22.5}Cu_{22.5}$ evidenced the best catalytic activity for the ethylene oxidation reaction, attributed to probable interactions occurring between the CeO_x, $MnCuO_x$ and CuO_x species. Consistently with these results, the

enhancement of the catalytic activity can be correlated to the improved reducibility of the catalysts.

Moreover, a novel in-situ SCS was used in order to catalyze two monoliths with the most promising powders studied (the $Ce_{55}Mn_{45}$ and the $Ce_{55}Mn_{22.5}Cu_{22.5}$). The catalytic performances of the monoliths were investigated in a bench-scale reactor. The results evidenced stable catalytic performances for the oxidation of both VOCs (propylene and ethylene) after 4 h time-on stream.

Chapter 4

Porous Manganese Oxides Doped with Fe and Cu synthesized via Sol-Gel method for the Catalytic Oxidation of Volatile Organic Compounds

4.1 Introduction

For this chapter, a set of copper-iron-doped manganese oxides was synthesized through the citrate sol-gel preparation technique. The technique allowed to synthesize mesoporous materials that evidenced promising catalytic performances in VOC oxidation reactions at relatively low temperatures. Moreover, catalytic performance reproducibility analyses were performed by means of consecutive VOC catalytic oxidation test.

The procedure carried out during the synthesis, along with the set of prepared catalysts is reported in section 2.2.2. The study of the physico-chemical properties of the synthesized catalysts was carried out using several characterization techniques (as reported in section 2.3). The powder catalysts were prepared and tested for the ethylene and propylene oxidation reactions.

This chapter includes data resulting from my personal research published in Marin Figueredo, M.J., Piumetti, M., Bensaid, S., Fino, D., Russo, N. (2021). Chapter 2: Catalytic Oxidation of Volatile Organic Compounds over Porous Manganese Oxides Prepared via Sol-Gel Method, *Nanostructured Catalysts for Environmental Applications* (p. 59-78). Springer Nature Switzerland AG.

4.2 Material structural and textural properties

The changes in the physicochemical properties due to the incorporation of the foreign metals (i.e., Cu or/and Fe) inside the Mn_2O_3 structure are assessed in this section. Accordingly, the diffraction patterns harvested for the prepared oxide catalysts (thus the Mn_2O_3, $MnCu_{15}$, $MnFe_{15}$, and $MnCu_{7.5}Fe_{7.5}$) by means of X-ray diffraction technique are summarized in section a of Figure 4.1.

Table 4.1 Structural and textural properties of the catalyst, according to the results obtained in N_2 physisorption at -196 °C and XRD analyses. Adapted by permission from Springer Nature Customer Service Centre GmbH: Springer Cham, Nanostructured Catalysts for Environmental Applications by Piumetti M., Bensaid S. (eds). © Springer Nature Switzerland AG 2021

Sample	S_{BET}[a] ($m^2\ g^{-1}$)	V_P[b] ($cm^3\ g^{-1}$)	D_P[c] (nm)	CS[d] (nm)	a[e] (nm)
Mn_2O_3	15	0.12	32	67	0.937
$MnCu_{15}$	14	0.10	30	67	0.937
$MnFe_{15}$	11	0.09	29	65	0.941
$MnCu_{7.5}Fe_{7.5}$	8	0.07	35	62	0.939
Fe_2O_3	11	0.06	23	57	-
CuO	3	0.01	14	34	-

[a]Specific surface area estimated by means of the BET method

[b]Calculated cumulative volume of pores according to the BJH method

[c]Calculated pore diameter according to the BJH method

[d]Crystallite size estimated by means of the Scherrer formula

[e]Cubic cell parameter

As a whole, the diffraction patterns of the samples consisted in the cubic crystal system of Mn_2O_3 (reference code 00-041-1442). Accordingly, this finding proposes that the foreign metal ions (thus Fe and/or Cu) are located inside the structure of Mn_2O_3. Consequently, this suggests the occurrence of solid solutions.

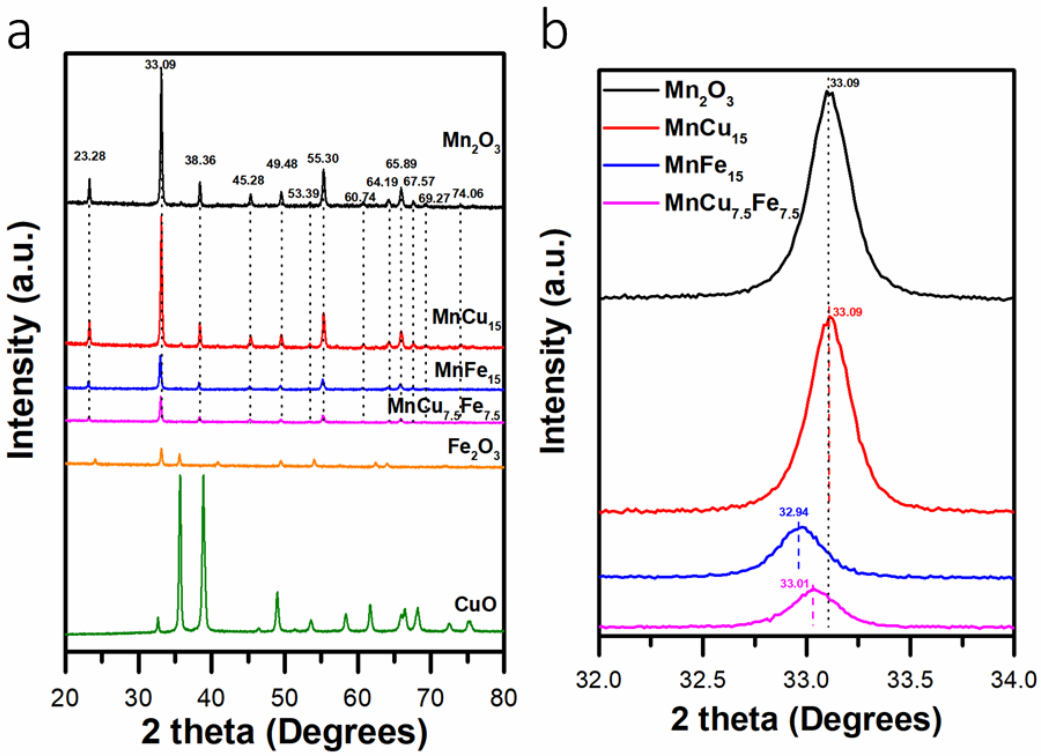

Figure 4.1 Diffraction patterns for the prepared samples harvested during X-ray diffraction analyses (a) and the corresponding magnifications (b). Reprinted by permission from Springer Nature Customer Service Centre GmbH: Springer Cham, Nanostructured Catalysts for Environmental Applications by Piumetti M., Bensaid S. (eds). © Springer Nature Switzerland AG 2021.

The magnifications reported in section b of Figure 4.1, evidence a translation of the diffraction peak with signal maximum at 33.09° to a lower 2θ value for the catalysts containing iron (thus, the $MnFe_{15}$ and $MnCu_{7.5}Fe_{7.5}$). Accordingly, the finding proposes that the Mn_2O_3 system expanded. This can be attributed to strain effects produced by the insertion of bigger Fe ions, in terms of ionic radii [r_{ion} of Fe^{2+}/Fe^{3+} (coordination number or CN = 6) is 0.061/0.055 nm], compared to both Mn species [r_{ion} of Mn^{3+}/Mn^{4+} (CN = 6) is 0.058/0.053 nm] and Cu species [r_{ion} of Cu^{+}/Cu^{2+} (CN = 6) is 0.077/0.073 nm] (Shannon, 1976).

Accordingly, the calculated lattice parameter (*a*, for a cubic cell) was observed to increase when the amount of Fe in the catalyst is higher (see Table 4.1). As well, a slight reduction of the crystallite size was observed (according to the values obtained by means of Scherrer formula) after the incorporation of Fe ions in the structure of Mn_2O_3. Instead, the presence of both copper and iron ions coincide with the formation of particles of ca. 62 nm. The diffraction observed for the synthesized CuO (green line) and Fe_2O_3 (orange line) corresponded to the crystalline systems of the following reference patterns: CuO with ref. code 01-072-0629; α-Fe_2O_3 with ref. code 00-024-0072.

Concerning the BET specific surface areas, the calculated values vary in the range 8-15 $m^2\ g^{-1}$. Accordingly, it seems that inserting iron or copper ions in the crystal system of Mn_2O_3 promotes a decrease of the S_{BET}. For the mixed samples, the cumulative volume of pores varied between 0.07-0.10 $cm^3\ g^{-1}$, while the pore width varied between 29-35 nm. Thus, evidencing a general decreasing trend when manganese and copper ions were inserted inside the structure of Mn_2O_3. The S_{BET} values obtained for the CuO and Fe_2O_3 catalysts were, respectively, 3 and 11 $m^2\ g^{-1}$. Moreover, lower D_P and V_P values were observed, compared to the manganese-containing samples.

The morphology of each catalyst, as observed during FESEM analyzes, are shown in Figure 4.2. As a whole, sheet-like structures are observed. These structures consisted in hollowed structures with a thick external shell. This finding, along with the calculated pore diameters, confirmed that the sol-gel procedure led to the formation of mesoporous structures. Moreover, the pored observed in the micrographs evidence diameters that can be compared to those obtained in BET calculations. Conversely, the image of the Fe_2O_3 sample evidence a more compact sheet structure with visible smaller pores. The micrograph of the CuO shows the formation of a structure formed by aggregated of nanoparticles, thus suggesting that the measurement of the pore width (according to the S_{BET} analysis) is interparticle.

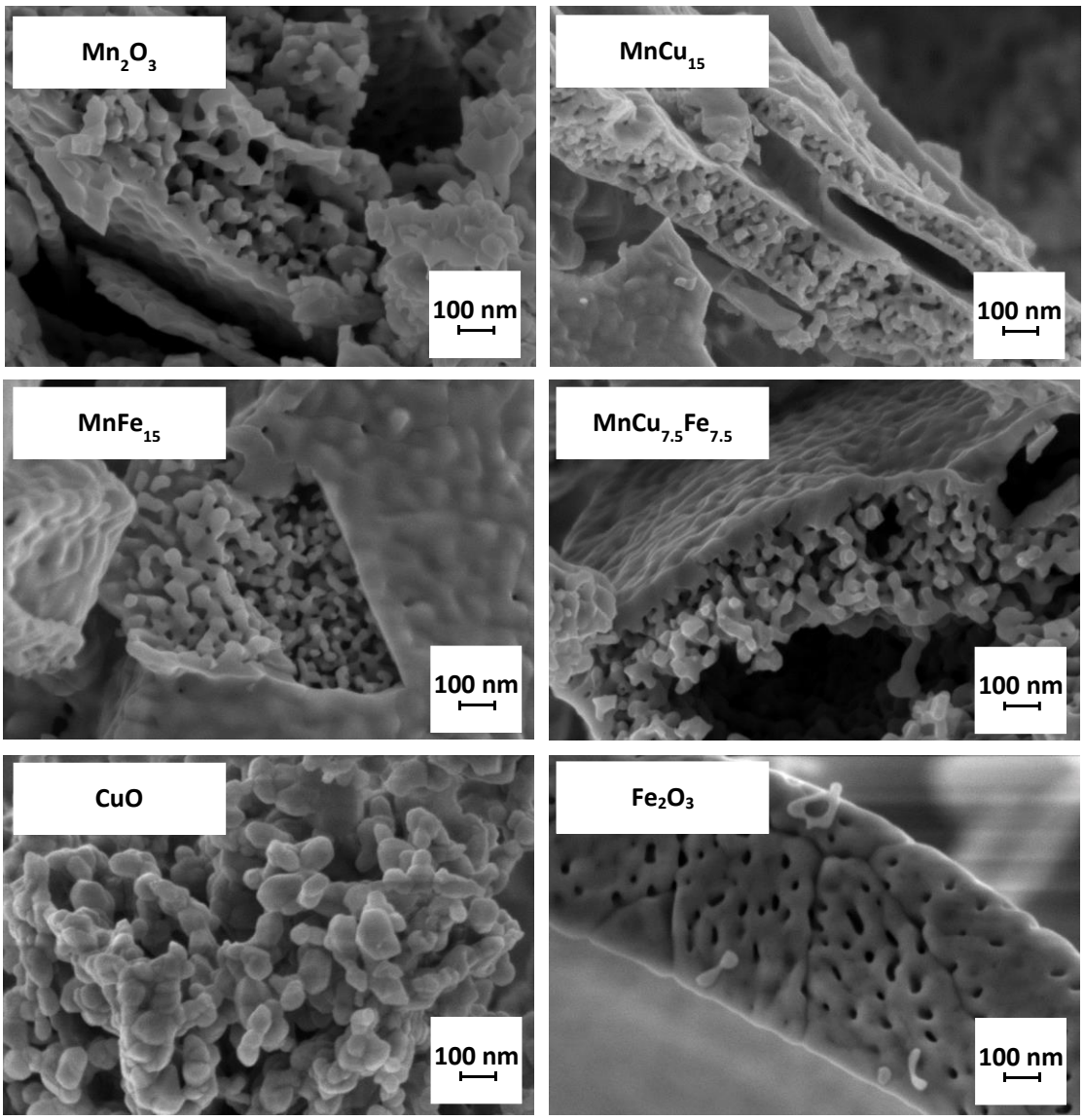

Figure 4.2 FESEM images of the synthesized catalysts. Reprinted by permission from Springer Nature Customer Service Centre GmbH: Springer Cham, Nanostructured Catalysts for Environmental Applications by Piumetti M., Bensaid S. (eds). © Springer Nature Switzerland AG 2021.

4.3 Temperature-programmed reduction analysis (H_2-TPR)

The reduction profiles harvested during the H_2-TPR analyses are shown in Figure 4.3. The first reduction signal for the Mn_2O_3 catalyst appeared at ca. 200 °C. As a whole, two intense peaks were observed: one at the lower temperature (ca. 351 °C), and another at higher temperature (ca. 487 °C). The former reduction signal was assigned to the step: $Mn_2O_3 \rightarrow Mn_3O_4$. Instead, the latter signal corresponds to the following step: $Mn_3O_4 \rightarrow MnO$ (Aguilera, Perez, Molina, & Moreno, 2011; Delimaris & Ioannides, 2008; Kapteijn et al., 1994; Marco Piumetti, Fino, et al., 2015). Noteworthy, the overall H_2-uptake (7.16 mmol g^{-1}), estimated by means of the signal deconvolution, resulted in a consumption value higher than the theoretical hydrogen amount needed for the reduction of Mn_2O_3 (6.33 mmol g^{-1}). Nevertheless, the consumption value is under the H_2-uptake needed for reducing MnO_2 (11.50 mmol g^{-1}). This suggests that a minor amount of Mn^{4+} species are present in the sample coupled with Mn^{3+} in the Mn_2O_3 catalyst.

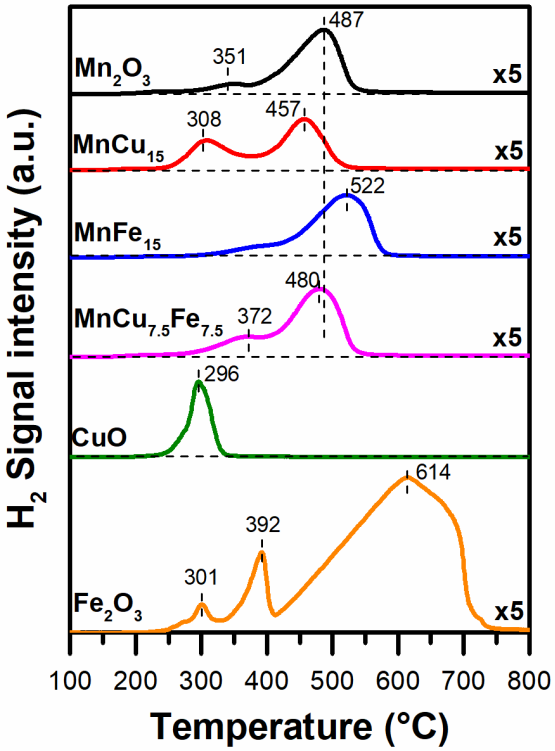

Figure 4.3 Reduction profiles harvested during H_2-TPR technique. Reprinted by permission from Springer Nature Customer Service Centre GmbH: Springer Cham, Nanostructured Catalysts for Environmental Applications by Piumetti M., Bensaid S. (eds). © Springer Nature Switzerland AG 2021.

The signal harvested during CuO reduction consisted in a sharp peak centered at 296 °C, as reported in the literature (G. Avgouropoulos, Ioannides, & Matralis, 2005; Delimaris & Ioannides, 2009; Marco Piumetti, Bensaid, Andana, Russo, et al., 2017). Conversely, a complex reduction behavior was observed for the Fe_2O_3 sample. As reported in the literature, the reduction signal appeared at 301 °C seems attributable to the hydroxylated oxide. Instead, the deconvolution of the signal located at about 392 °C revealed a H_2-uptake of ca. 2.35 mmol g^{-1}, which is in fair agreement with the theoretical consumption (2.09 mmol g^{-1}) during the following step: $Fe_2O_3 \rightarrow Fe_3O_4$. The reduction signal appeared at higher temperature values was assigned to the following steps: $Fe_3O_4 \rightarrow FeO \rightarrow Fe$ (Munteanu, Ilieva, & Andreeva, 1997; Zieliński, Zglinicka, Znak, & Kaszkur, 2010).

Regarding the reduction signals of the $MnCu_{15}$ and the $MnFe_{15}$, a two-peak behavior similar to that of the parent Mn_2O_3 was observed in both cases. In this sense, the $MnCu_{15}$ (see red line, Figure 4.3) evidenced reduction peaks that took place at temperatures (at about 308 and 487 °C) below to those of the parent Mn_2O_3. The signal occurred at lower temperature appeared close to the temperature needed for the reduction of Cu^{2+} species, therefore it was assigned to the reduction of both Mn^{3+} and Cu^{2+} species. Moreover, the reduction of manganese species continues at higher temperatures. These findings suggest that Mn^{3+} species were effectively substituted by copper species in the lattice (Aguilera et al., 2011; Wöllner et al., 1993).

As a whole, the reduction profile of the $MnFe_{15}$ catalyst (see blue line, Figure 4.3) started at about 300 °C and achieved a signal maximum at about 522 °C. Such reduction behavior is similar to the one observed in the parent Mn_2O_3. However, the reduction profile translated slightly to higher temperatures. Consistently, these results suggest that incorporating Fe^{x+} species enhanced the formation of a more stable oxide structure, i.e., a structure more resistant to the reduction. Other authors reported that the reduction signal appeared at temperatures under 530 °C is ascribed to the following reduction steps: $Mn^{3+} \rightarrow Mn^{2+}$ and $Fe^{3+} \rightarrow Fe^{2+}$. Instead, the signal located at higher temperatures is attributed to the following reduction: $Fe^{2+} \rightarrow Fe$ (Leith & Howden, 1988; T. Li et al., 2007).

The reduction curve of the $MnCu_{7.5}Fe_{7.5}$ catalyst (see magenta line, Figure 4.3) is rather similar to the reduction curve of the parent Mn_2O_3. However, it was observed that the maximum peak value slightly translated to a lower temperature. Moreover, an enhanced signal intensity (thus a higher H_2 uptake) occurred at about 372 °C. Interestingly, this appears an intermediate case respect to the $MnFe_{15}$ and

$MnCu_{15}$ catalysts. In this sense, the reduction signal occurred in the lower temperature region was ascribed to the copper species present in the catalyst to Cu^0. As well, the same signal was assigned to the initial reduction of the Mn^{3+} and Fe^{3+} species to Mn^{2+} and Fe^{2+}, respectively. Finally, the reduction signal appeared at about 480 °C was attributed to the further reduction of the manganese and iron species.

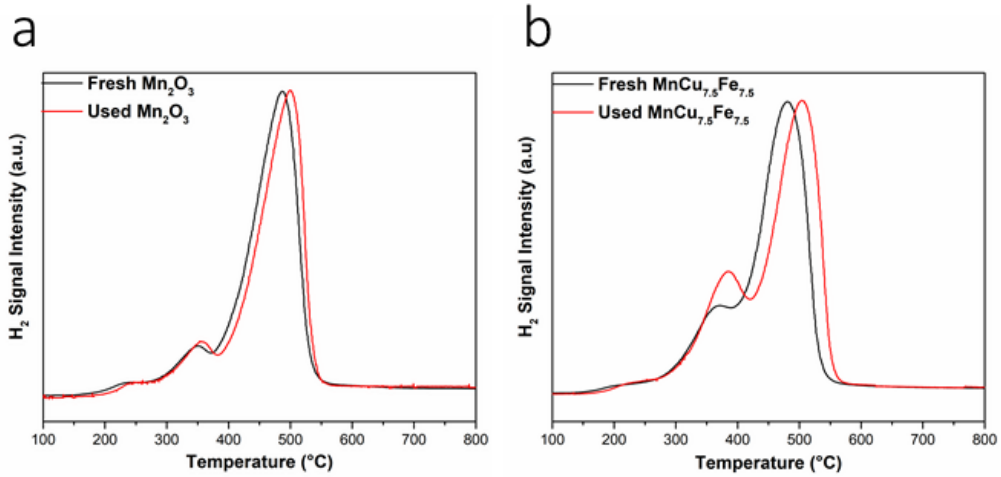

Figure 4.4 H_2-TPR profiles of the Mn_2O_3 (a) and $MnCu_{7.5}Fe_{7.5}$ (b) before and after catalytic testing. Reprinted by permission from Springer Nature Customer Service Centre GmbH: Springer Cham, Nanostructured Catalysts for Environmental Applications by Piumetti M., Bensaid S. (eds). © Springer Nature Switzerland AG 2021.

Additionally, the eventual variation of the reducibility in the most promising catalysts was investigated (Mn_2O_3 and $MnCu_{7.5}Fe_{7.5}$). For this analysis, the catalysts were harvested after their use in catalytic tests for the abatement of the probe VOC molecules, in other words, propylene and ethylene. Accordingly, the reduction signals reported in Figure 4.4 include the reduction of the fresh and used catalysts (black and red lines, respectively). As observed in section a, the Mn_2O_3 catalyst showed similar reduction behavior before and after the catalytic test. However, after catalytic testing the reduction signal takes place slightly higher temperatures. This can be attributed to the reduction of larger particles of MnO_x (Kundakovic & Flytzani-Stephanopoulos, 1998), which formation can be enhanced the relatively high temperatures (ca. 300 °C) reached during the catalytic screenings.

Similarly, the reduction signal of the used $MnCu_{7.5}Fe_{7.5}$ (reported in section b, Figure 4.4), is translated to slightly higher temperatures, compared to the fresh

catalyst. The finding suggests that bigger particles appeared as well in the case of the $MnCu_{7.5}Fe_{7.5}$. Noteworthy, the enhanced peak signal occurred at about 384 °C (see red line) indicates that a higher number of species are reducing in that temperature range, therefore of Mn^{3+}, Fe^{3+} or Cu^{2+} species. Since the initial oxidation state of copper species (as observed in XPS analysis, vide infra) is 2+, this finding proposes that either Fe^{2+}or Mn^{2+} species were oxidized to Fe^{3+}or Mn^{3+}, respectively, throughout the catalytic abatement test.

4.4 X-ray photoelectron spectroscopy

The various spectra of harvested via the X-ray photoelectron spectroscopy technique are reported in Figure 4.5. The XP spectra summarized in section a correspond to the O 1*s* core level. As a whole, the spectra evidenced two peaks, each one ascribed to different oxygen species. Accordingly, the signal appeared at binding energy (BE) values between 529.5-529.8 eV is ascribed to the O^{2-} specie, therefore oxygen present in the lattice of Mn_2O_3 (O_β-species). Accordingly, these oxygens are bonded to Mn, Cu, or Fe (Moulder, Stickle, Sobol, & Bomben, 1992). Instead, the signals appeared in the 531.1–531.4 eV region were ascribed to O^-, O_2^- species, thus, chemisorbed oxygen species (O_α-type), and to OH groups (Kim & Shim, 2010; Santos et al., 2010).

Table 4.2 Relative abundances of oxygen species (at.%) and their ratio, as estimated from the O 1*s* core level XP spectra deconvolution. Adapted by permission from Springer Nature Customer Service Centre GmbH: Springer Cham, Nanostructured Catalysts for Environmental Applications by Piumetti M., Bensaid S. (eds). © Springer Nature Switzerland AG 2021

Sample	O_α ,OH BE (eV)	O_α (at.%)	O_β BE (eV)	O_β (at.%)	O_α/O_β
Mn_2O_3	531.4	57.7	529.8	42.3	1.36
$MnCu_{15}$	531.2	38.3	529.6	61.7	0.62
$MnFe_{15}$	531.1	31.8	529.7	68.2	0.47
$MnCu_{7.5}Fe_{7.5}$	531.1	38.3	529.5	61.7	0.62
CuO	531.4	35.3	529.7	64.7	0.55
Fe_2O_3	531.4	28.4	529.8	71.6	0.40

As reported in Table 4.2, the sample with highest occurrence of chemisorbed species (therefore with the highest O_α/O_β) is the parent Mn_2O_3. Subsequently, the $MnCu_{7.5}Fe_{7.5}$ and the $MnCu_{15}$ catalysts and the CuO, which evidenced an intermediate value for the same ratio (0.62 and 0.55, respectively). The lowest values for the O_α/O_β ratio were observed in the $MnFe_{15}$ and the Fe_2O_3 catalysts, evidencing the reduced population of chemisorbed species in these samples.

The spectra shown in section b of Figure 4.5, were collected in the Mn 2*p* core level (along with the corresponding deconvolution). The spin signal attributed to the $2p_{3/2}$ level appeared at about 638.0-647.5 eV. Instead, in the 647.5-655.5 eV range the signal corresponds to the $2p_{1/2}$ level. As reported other published investigations, the relative abundance the manganese species (Mn^{2+}, Mn^{3+}, and Mn^{4+}) present in the samples can be estimated by means of the deconvolution of the $2p_{3/2}$ level, (Biesinger et al., 2011; Marco Piumetti, Fino, et al., 2015; Santos et al., 2010). The estimated abundances of the manganese species are reported in Table 4.3. Compared to the parent Mn_2O_3, an increased population of Mn^{4+} species is observed when copper and iron species are present in the oxides. This reveals that inserting Fe or/and Cu promoted the occurrence of oxidized Mn^{4+} species. Meanwhile, the deconvolution highlights the presence of an increased number of reduced manganese species (i.e. Mn^{2+}) in the $MnCu_{15}$ catalyst.

Table 4.3 Relative abundances of Mn^{x+} species over the synthesized materials and BE values according to the Mn 2*p* core level spectra deconvolution. Adapted by permission from Springer Nature Customer Service Centre GmbH: Springer Cham, Nanostructured Catalysts for Environmental Applications by Piumetti M., Bensaid S. (eds). © Springer Nature Switzerland AG 2021

Sample	**Mn^{4+} BE (eV)**	**Mn^{4+} (at.%)**	**Mn^{3+} BE (eV)**	**Mn^{3+} (at.%)**	**Mn^{2+} BE (eV)**	**Mn^{2+} (at.%)**	**$\frac{Mn^{4+}}{Mn^{3+}}$**	**$\frac{Mn^{3+}}{Mn^{2+}}$**
Mn_2O_3	644.8	5.5	642.0	75.3	640.9	19.2	0.07	3.92
$MnCu_{15}$	644.1	13.7	642.1	51.3	640.8	35.1	0.27	1.46
$MnFe_{15}$	644.2	13.9	642.0	60.6	640.8	25.5	0.23	2.38
$MnCu_{7.5}Fe_{7.5}$	644.2	14.9	641.8	62.2	640.7	22.9	0.24	2.71

The XP spectra shown in section c (and the deconvolution), Figure 4.5 correspond to the Cu 2*p* core level. The signal appeared between 930.0-939.0 eV corresponds to the $2p_{3/2}$ level. The eventual occurrence of Cu^{2+} species is indicated by their corresponding "shake-ups" that are observed in the BE range 940.0-946.0 eV. Additionally, a deconvolution of the signal ascribed to the $2p_{3/2}$ level can aid in the relative quantification of Cu species present in the catalysts (Biesinger et al., 2010; W. Liu & Flytzani-Stephanopoulos, 1995b; Moulder et al., 1992; Marco Piumetti, Bensaid, Andana, Russo, et al., 2017). In this sense, the CuO evidenced three signals that contributed to the $2p_{3/2}$ level. The signal appeared at ca. 934.8 is

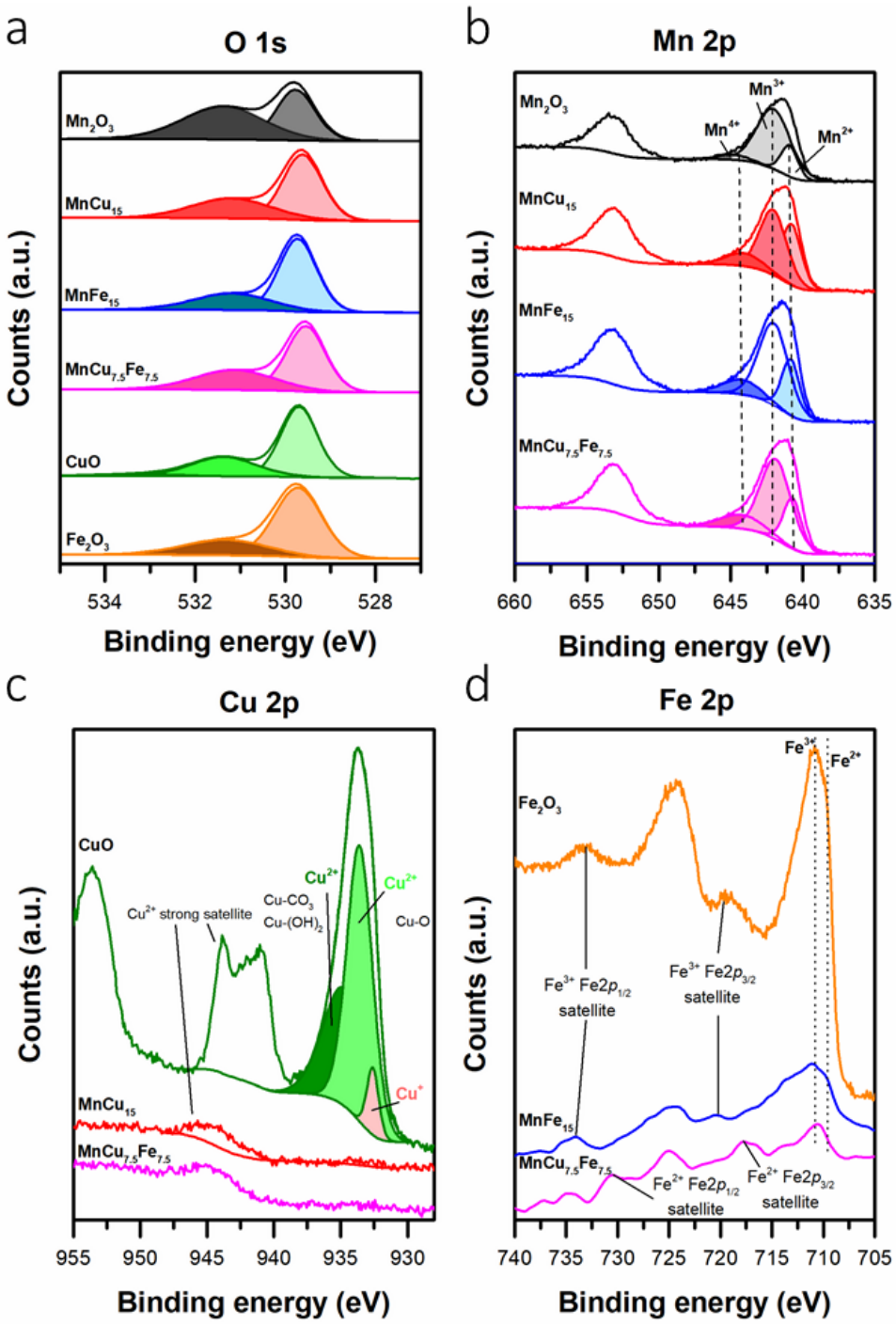

Figure 4.5 XPS spectra harvested in the O (1*s*), Mn (2*p*), Cu (2*p*), and Fe (2*p*) core level. Reprinted by permission from Springer Nature Customer Service Centre GmbH: Springer Cham, Nanostructured Catalysts for Environmental Applications by Piumetti M., Bensaid S. (eds). © Springer Nature Switzerland AG 2021.

assigned to copper carbonates and/or hydroxide. While the signal located at 933.6 eV corresponds to the Cu-O bond in the lattice. Noteworthy, the deconvolution showed a contribution (6.3 at.%) at ca. 932.6 eV, associated to reduced Cu^{+} species (Biesinger et al., 2010; Kundakovic & Flytzani-Stephanopoulos, 1998). The spectrum intensity of the $MnCu_{7.5}Fe_{7.5}$ and the $MnCu_{15}$ and samples increased mostly in the zone ascribed to the strong Cu^{2+} satellite. Therefore, highlighting that the oxidation state of the copper present in those catalysts is +2.

The spectra harvested in the Fe 2*p* core level are reported in section d, Figure 4.5. The spectrum signal ascribed to the $2p_{3/2}$ level appeared between 707.5 and 714.8 eV, instead, between 721.7 and 728.5 eV the signal corresponds to the $2p_{1/2}$ level. The position of each signal, and the corresponding satellites can aid to identify the oxidation state of the iron species in the catalyst (Biesinger et al., 2011; Yamashita & Hayes, 2008). Intense spectrum signals were observed at 710.6, 711.0 and 710.8 eV for the Fe_2O_3, $MnFe_{15}$ and $MnCu_{7.5}Fe_{7.5}$ catalysts, respectively. Accordingly, the appeared signal and the satellites corresponding to Fe^{3+} species unequivocally reveal the predominance of the Fe^{3+} species in the mentioned catalysts. Conversely, though the contribution of the reduced iron species (thus the Fe^{2+}) in the $2p_{3/2}$ level is not evident, the presence of the corresponding satellites seems detectable in the spectrum harvested for the $MnCu_{7.5}Fe_{7.5}$ sample. Remarkably, in the $MnCu_{7.5}Fe_{7.5}$ catalyst the occurrence of the Fe^{2+} reduced species coincides with an increased number of oxidized Mn^{4+} species (vide supra). This proposes that the formation of Fe^{2+} species could be promoted by the simultaneous substitution of Mn^{3+} species with Fe and Cu species in the lattice.

4.5 Catalytic activity

The catalytic conversion of C_3H_6 over the prepared catalysts is reported in Figure 4.6. Noteworthy, when no catalyst was present in the reactor, only 9% conversion of the VOC was achieved at the maximum tested temperature (400 °C), by means of thermal oxidation. Conversely, the presence of the synthesized catalysts was beneficial for the propylene conversion. In fact, the VOC total conversion occurred at temperatures significantly lower than 400 °C.

The Table 4.4 reports the catalytic performances of the prepared catalysts, in terms of the calculated reaction rates of the VOCs. Moreover, the temperatures required for achieving 10%, 50%, and 90% conversion of the corresponding VOC (i.e., $T_{10\%}$, $T_{50\%}$, and $T_{90\%}$) in carbon dioxide are reported. As a whole, the conver-

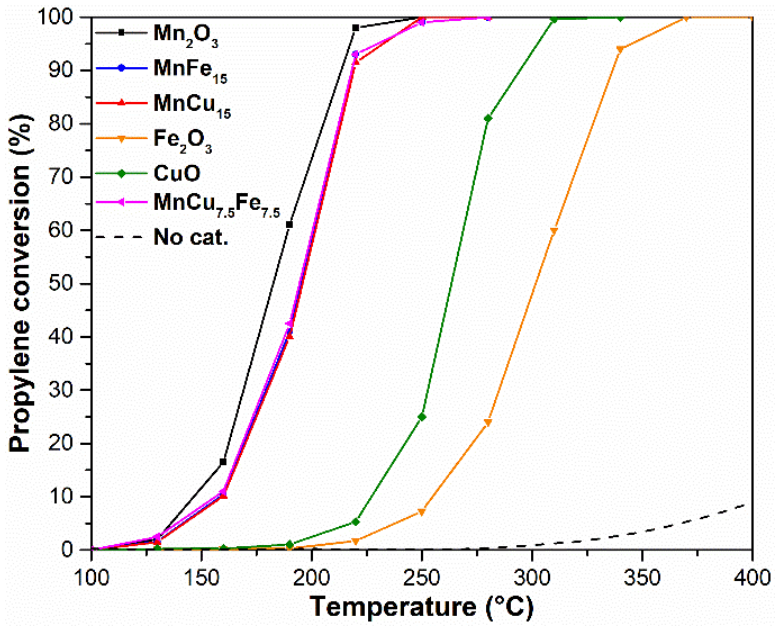

Figure 4.6 Conversion (%) of propylene over the synthesized catalysts as a function of the temperature. Reprinted by permission from Springer Nature Customer Service Centre GmbH: Springer Cham, Nanostructured Catalysts for Environmental Applications by Piumetti M., Bensaid S. (eds). © Springer Nature Switzerland AG 2021.

sion of the studied VOCs over the prepared Mn_2O_3 (black line) occurred at lower temperature values, compared to the Fe_2O_3 (orange line) and CuO (green line) catalysts. Consequently, a decreasing trend for the catalytic activity can be outlined: Mn_2O_3 > CuO > Fe_2O_3. Regarding the prepared manganese oxides, the propylene conversion took place at temperatures slightly higher, compared to parent Mn_2O_3 (in other words, the reaction takes place at higher $T_{10\%}$, $T_{50\%}$, and $T_{90\%}$). The catalytic performances observed are rather similar along the investigated temperature range. Nevertheless, a catalytic kinetic assessment is carried out at low conversion values (at ca. the light-off temperatures), since at higher temperatures other phenomena take place (e.g., mass-transfer phenomena) (M. Piumetti & Russo, 2017). In this sense, the data reported in Table 2.4 reveals that only the $MnCu_{15}$ and the $MnFe_{15}$ presented lower rates of propylene oxidation (r_p) at 130 °C, compared to the parent Mn_2O_3, and therefore, a worsening of the catalytic activity. Consistently, the $MnFe_{15}$ and $MnCu_{15}$ evidenced almost equivalent catalytic activities. Noteworthy, the best r_p value was achieved by the $MnCu_{7.5}Fe_{7.5}$ catalyst (1.47 μmol h^{-1} m^{-2}), in spite of presenting a S_{BET} lower than the parent Mn_2O_3. In this sense, the catalytic performance trend can be outlined, as follows: $MnCu_{7.5}Fe_{7.5}$ > Mn_2O_3 > $MnFe_{15}$ ≈ $MnCu_{15}$.

Table 4.4 Summary of the performances of the synthesized catalysts in the propylene and ethylene oxidation reactions. Adapted by permission from Springer Nature Customer Service Centre GmbH: Springer Cham, Nanostructured Catalysts for Environmental Applications by Piumetti M., Bensaid S. (eds). © Springer Nature Switzerland AG 2021

Sample	Propylene oxidation				Ethylene oxidation			
	$T_{10\%}$ (°C)	$T_{50\%}$ (°C)	$T_{90\%}$ (°C)	r_p[a] (μmol $h^{-1}m^{-2}$)	$T_{10\%}$ (°C)	$T_{50\%}$ (°C)	$T_{90\%}$ (°C)	r_e[b] (μmol $h^{-1}m^{-2}$)
Mn_2O_3	152	183	212	0.94	168	204	237	1.67
$MnCu_{15}$	160	196	219	0.51	176	222	250	1.69
$MnFe_{15}$	159	196	217	0.60	175	213	243	1.53
$MnCu_{7.5}Fe_{7.5}$	158	195	217	1.47	165	208	244	4.41
CuO	231	263	289	0.25	235	271	303	0.85
Fe_2O_3	257	302	335	0.05	281	342	386	0.22

[a]Calculated at 130 °C, [b]Calculated at 160 °C

The performance of the catalysts in the ethylene oxidation reaction is reported in Figure 4.7. In absence of catalyst (see black-dashed line), a maximum conversion of 1.2% was achieved at the highest temperature investigated, i.e., at 400 °C. The parent oxide catalysts (Mn_2O_3, CuO and Fe_2O_3) evidenced similar catalytic performances to those observed in the oxidation of propylene, therefore the catalytic activity trend is: Mn_2O_3 > CuO > Fe_2O_3. The ethylene oxidation reaction took place at higher temperatures compared to those required for the oxidation of propylene, thus demonstrating the higher stability of the former molecule.

Accordingly, the higher stability of ethylene towards oxidation (respect to propylene) allows to better investigate the catalytic performances of the prepared powders. At high temperatures (T > 190 °C), the parent Mn_2O_3 evidenced a better performance, compared to the doped manganese oxides. Nevertheless, the reaction rates for the catalytic oxidation of ethylene (r_e) at 160 °C (reported in Table 4.4) highlight that Mn_2O_3 and the $MnCu_{15}$ evidenced rather similar catalytic activities. Instead, the insertion of Fe species in the structure of Mn_2O_3 seems to cause a slight decrease of the catalytic activity of the manganese species. In this sense, the results suggest that better interactions occur among the Mn and Cu species, whereas those taking place only between Mn and Fe species can, apparently, compromise the activity of the catalyst. The possible role of beneficial interactions taking place among Cu and Mn species for the ethylene oxidation reaction was reported/observed as well in a previous investigation (Marin Figueredo et al., 2020). Noteworthy, the $MnCu_{7.5}Fe_{7.5}$ catalyst evidenced the highest rate (4.41 μmol h^{-1} m^{-}

^{2}) for the ethylene catalytic oxidation reaction. This remarkable finding remarks the possibility that beneficial interactions may occur between all three Cu, Fe and Mn species, in Mn-Cu-Fe-O_x catalysts synthesized by means of the sol-gel technique. Moreover, the catalytic activity of the mentioned catalyst for the oxidation of C_2H_4 seems strongly related to: (i) the elevated amount of chemisorbed oxygen and (ii) improved low-temperature reducibility (as observed for the C_3H_6 oxidation reaction). Accordingly, a trend for the catalytic activity in the C_2H_4 oxidation reaction can be outlined: $MnCu_{7.5}Fe_{7.5}$ > Mn_2O_3 > $MnCu_{15}$ > $MnFe_{15}$.

The literature reports that a high number of oxygen species (chemisorbed on

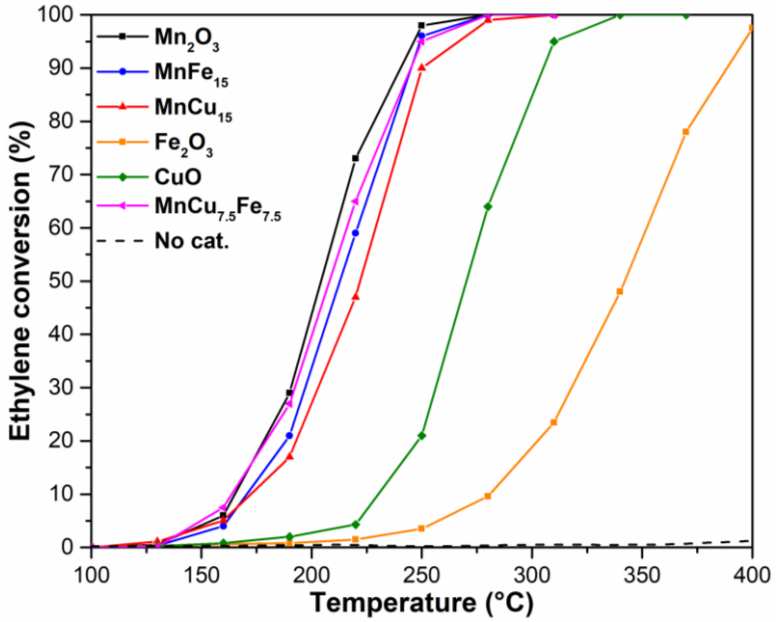

Figure 4.7 Conversion (%) of ethylene over the synthesized catalysts as a function of the temperature. Reprinted by permission from Springer Nature Customer Service Centre GmbH: Springer Cham, Nanostructured Catalysts for Environmental Applications by Piumetti M., Bensaid S. (eds). © Springer Nature Switzerland AG 2021.

the catalytic surface) is beneficial for the VOC catalytic oxidation reaction, attributable to their better mobility compared to the oxygens located in the lattice (Kim & Shim, 2010; Marco Piumetti, Fino, et al., 2015; Santos et al., 2010). Accordingly, the improved catalytic performance of the $MnCu_{7.5}Fe_{7.5}$ catalyst may be associated to the elevated population of weakly-bonded oxygen species, in other words O_α-species, as revealed by XPS studies (reported in Table 4.2).

Moreover, the presence of coupled Mn species in the catalysts with various oxidation states (thus, $Mn^{2+}|Mn^{3+}|Mn^{3+}$), has been associated to improvements of the activity in MnO_x catalysts (Marco Piumetti, Fino, et al., 2015; Santos et al., 2010). Nevertheless, the catalytic enhancement of the synthesized catalysts for the propylene reaction seems to be lessened by the elevated number of reduced manganese species (Mn^{2+}, see Table 4.3). Moreover, and consistently with the literature, the improved low-temperature reducibility of the $MnCu_{7.5}Fe_{7.5}$ catalyst (as observed during the reducibility studies, vide supra) can be the key factor leading to the marked catalytic enhancement in VOC oxidation (Aguilera et al., 2011; Genuino et al., 2012; Kamal et al., 2016; Marin Figueredo et al., 2020; Njagi et al., 2012; Santos et al., 2010). In this sense, the results confirm inserting Fe and Cu species in the structure of Mn_2O_3 by means of the sol-gel technique may improve its catalytic activity for the ethylene and propylene oxidation reactions, and therefore for a wide group of volatile organic compounds.

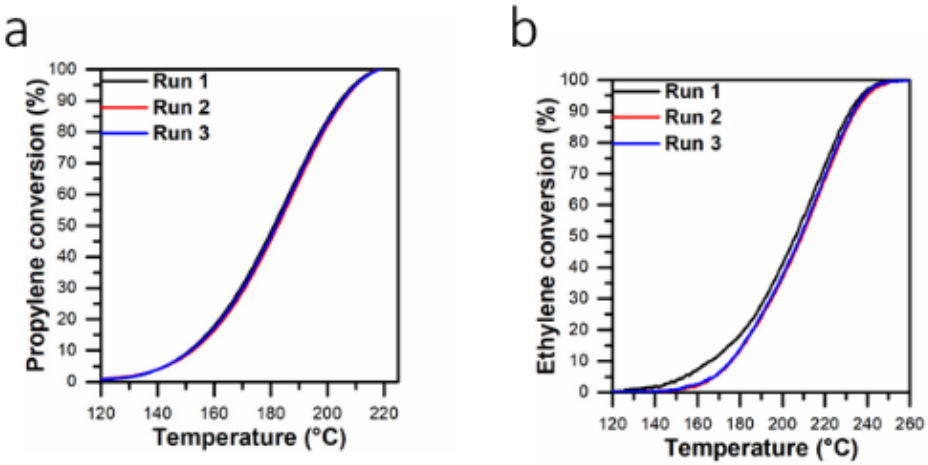

Figure 4.8 Catalytic stability screening for the (a) propylene and (b) ethylene oxidation reactions over the Mn_2O_3 catalyst. Reprinted by permission from Springer Nature Customer Service Centre GmbH: Springer Cham, Nanostructured Catalysts for Environmental Applications by Piumetti M., Bensaid S. (eds). © Springer Nature Switzerland AG 2021.

In addition, one of the most promising catalysts, i.e. the parent Mn_2O_3 was used in tests of consecutive VOC oxidation cycles, with the aim of evaluating the reproducibility of the catalytic conversion after continuous testing, and therefore, the catalytic stability. The resulting conversions of C_3H_6 and C_2H_4 are reported in Figure 4.8.

The results evidence that a reproducible behavior of the propylene conversion occurs after three consecutive catalytic runs. Therefore, no noticeable variation of the catalytic performance took place. Regarding the stability study for the oxidation of ethylene, the light-off conversion occurred at lower temperatures only in the first run. Nevertheless, the catalytic performance stabilized after the three-test oxidation cycle. In this sense, these analyses reveal that stable catalytic performances can be expected from the investigated catalyst.

4.6 Conclusions

For this chapter, transition metal oxides (Mn_2O_3, Fe_2O_3 and CuO) and doped manganese oxides ($MnCu_{7.5}Fe_{7.5}$, $MnFe_{15}$, and $MnCu_{15}$) were prepared by means of a facile sol-gel synthesis. The syntheses were carried out using typical chemical compounds, i.e. citric acid and metal nitrates. The physico-chemical properties of the prepared samples were studied using complementary characterization techniques: N_2-physisorption at -196 °C, FESEM, XRD, H_2-TPR, and XPS.

The first results revealed that the sol-gel synthesis allowed to prepare mesoporous structures, consisting in the crystalline structure of the parent Mn_2O_3 sample. The shifting of the XRD diffractograms allowed to estimate the variation of the cubic cell parameter, and as a consequence to demonstrate that the transition metals (Fe and/or Cu) inserted in the structure of Mn_2O_3. The catalytic screenings carried out revealed the excellent catalytic performances and activities of the Mn_2O_3 and $MnCu_{7.5}Fe_{7.5}$ catalysts for both the ethylene and propylene oxidation reactions. The results highlighted that the improved activity in the catalytic oxidation reactions of the probe VOC molecules is strongly related to the following key aspects: (i) a high number of surface-chemisorbed oxygen species and (ii) the improved low-temperature reducibility of the oxide catalyst. Consistently, an excellent performance was observed in the Mn_2O_3 catalyst. Moreover, synergistic interactions between Mn, Fe and Cu species present in $MnCu_{7.5}Fe_{7.5}$ most likely assured an outstanding catalytic activity, compared to the other catalysts prepared. Additionally, the Mn_2O_3 catalyst evidenced a good and stable catalytic performance in the investigated VOC oxidation reactions in a cycle of three consecutive catalytic runs.

Chapter 5

Fe and Cu doped Manganese Oxides Prepared with the Sol-Gel technique for the Catalytic Abatement of VOCs and Soot

5.1 Introduction

For this chapter, a set of Cu or Fe doped-MnO_x catalysts was prepared by means of two the sol-gel (SG) technique using the corresponding metal nitrates and citric acid. The synthesized catalysts showed a good catalytic activity for the catalytic oxidation of particulate matter under "loose" contact conditions. Moreover, the catalysts were investigated in catalytic propylene (as VOC probe molecule) abatement tests. Additionally, novel catalytic oxidation tests for the simultaneous elimination of carbonaceous matter and propylene under a gaseous stream containing 5 vol.% of water were performed.

The procedure used for the synthesis of the catalytic materials (sol-gel synthesis), along with the set of prepared catalysts is reported in section 2.2.2. The study of the physico-chemical properties of the synthesized catalysts was carried out using several characterization techniques (as reported in section 2.3).

This chapter includes data resulting from my personal research and was published in: Marin Figueredo, M.J., Piumetti, M., Fino, D., Russo N., Cocuzza,

C., Bensaid, S. (2021). Catalytic Oxidation of Soot and Volatile Organic Compounds over Cu and Fe Doped Manganese Oxide Prepared via Sol-Gel Synthesis. *SAE Technical Papers*, 1, pages 18. The publication and the copyright license are consultable at the following link: https://saemobilus.sae.org/content/2021-24-0088/.

5.2 Material structural and textural properties

The micrographs reported in Figure 5.1 show the morphologies of catalysts prepared through the sol-gel synthesis. In accordance with previous investigations, both the FESEM images and the calculated average pore diameters (as reported in Table 5.1, vide infra) highlight that the synthesized catalysts consist in mesoporous structures (Marco Piumetti, Fino, et al., 2015). Interestingly, the morphologies observed evidence a "flake-like" arrangement consisting in a thick external wall that encloses a void interior, resembling a honeycomb structure. The BET specific surface areas calculated by means of the data harvested in the N_2 physisorption analyses are summarized in Table 5.1. The S_{BET} of the metal-doped catalysts was observed to slightly decrease, compared to the parent Mn_2O_3. Similarly, the cumulative pore volume (V_P=0.09-0.11 $cm^3\ g^{-1}$) evidenced a slight decreasing trend when the insertion of the foreign metals inside the MnO_x structure was carried out.

The calculated size of crystallites (according to Scherrer formula) was observed to decrease when Fe and Cu were separately inserted in the MnO_x structure. Nevertheless, when the metals were present in the system contemporarily, the crystallite size remained did not change. The diffractograms harvested during the XRD analyses are reported in section a of Figure 5.2. As a whole, the profiles correspond to the diffraction pattern characteristic of the manganese oxide (III) in a cubic crystal system (with reference code 01-078-0390). This finding proposes that, during the synthesis procedure, the formation of other oxide phases (e.g. CuO or Fe_2O_3) did not occur and, as a consequence, foreign metals were incorporated in the MnO_x crystalline structure. Magnifications of the maximum diffraction signal are summarized in section b of Figure 5.2. The latter evidences that the single insertion of Fe or Cu species relocated the most intense diffraction peak from 32.83° to lower 2θ values (32.79° and 32.71° respectively). In this sense, these results highlight that an expansion of the crystalline structure (of Mn_2O_3) occurred. This can be attributes to the presence of the foreign metal species that induce strain in the crystalline system, because of their bigger ionic radii [r_{ionCu} Cu^+/Cu^{2+} = 0.077/0.073 nm with coordination number (CN) = 6, whereas r_{ionFe} Fe^{2+}/Fe^{3+} =

0.061/0.055 nm with CN=6]. Instead, for Mn ions [r_{ionMn} Mn^{3+}/Mn^{4+} = 0.058/0.053 nm with CN=6] (Shannon, 1976).

Table 5.1 Textural and structural properties, estimated from the resulting data of the N_2 physisorption at -196 °C and X-ray diffraction techniques, for the fresh and aged catalysts. Adapted from (Marin Figueredo, Piumetti, Fino, et al., 2021)

Sample	S_{BET}[a] (m^2 g^{-1})	V_P[b] (cm^3 g^{-1})	D_P[c] (nm)	CS[d] (nm)	*a*[e] (nm)
Mn_2O_3	13	0.11	32	73	0.945
$MnCu_{7.5}Fe_{7.5}$	12	0.11	37	73	0.944
$MnCu_{15}$	12	0.10	33	56	0.946
$MnFe_{15}$	10	0.09	34	69	0.948
Aged-Mn_2O_3	6	0.02	12	108	0.947
Aged-$MnCu_{7.5}Fe_{7.5}$	6	0.02	15	112	0.945

[a]Specific surface area calculated by means of the BET method, [b]Cumulative volume of pores, [c]Average pore diameter calculated according to the BJH method, [d]Size of crystallites calculated by means of the Scherrer's formula, [e]Cubic cell parameter

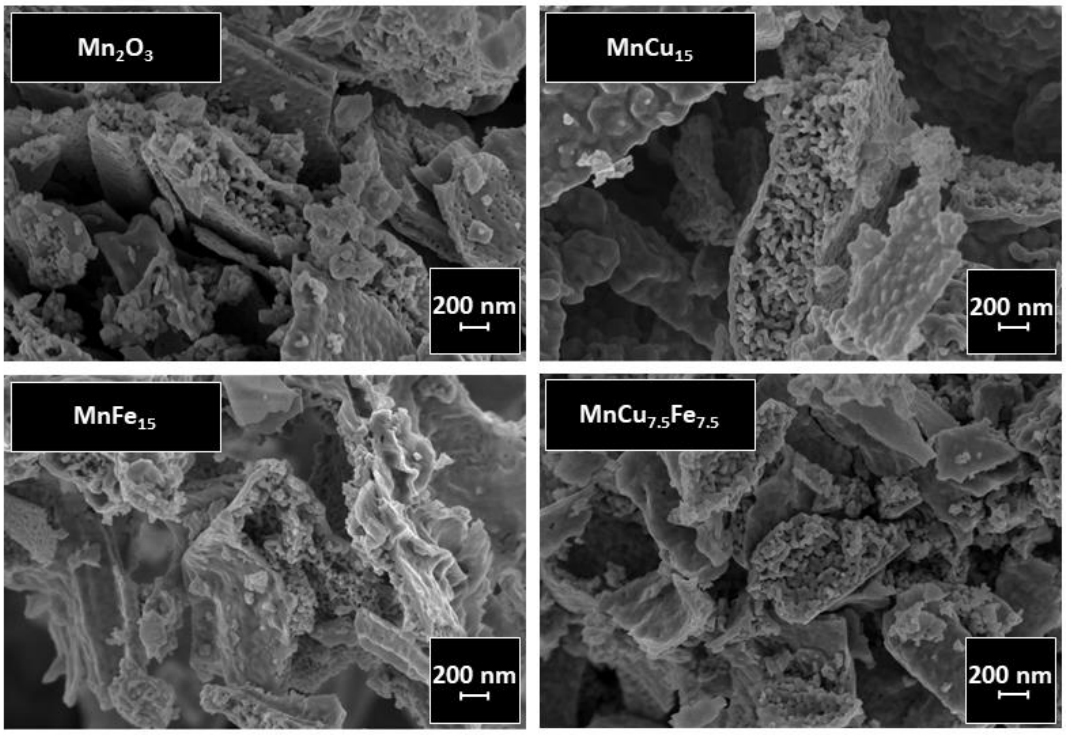

Figure 5.1 FESEM micrographs of the synthesized catalysts. Reprinted from (Marin Figueredo, Piumetti, Fino, et al., 2021).

Moreover, the changes in terms of textural properties (of the Mn_2O_3 and the $MnCu_{7.5}Fe_{7.5}$ catalyst) subsequent to a thermal-ageing procedure are included in Table 5.1. It shows that the S_{BET} was reduced for both catalysts, thus reaching values of ca. 6 m^2 g^{-1}. Additionally, the cumulative volume and diameter of the pores evidenced a marked decrease. These variations occurred probably due to a sintering process of the particles that may occur due to the severe thermal aging conditions used (750 °C, 4 h). As well, the crystalline properties varied, thus evidencing an enhancement of size of crystallites and the cubic cell parameter.

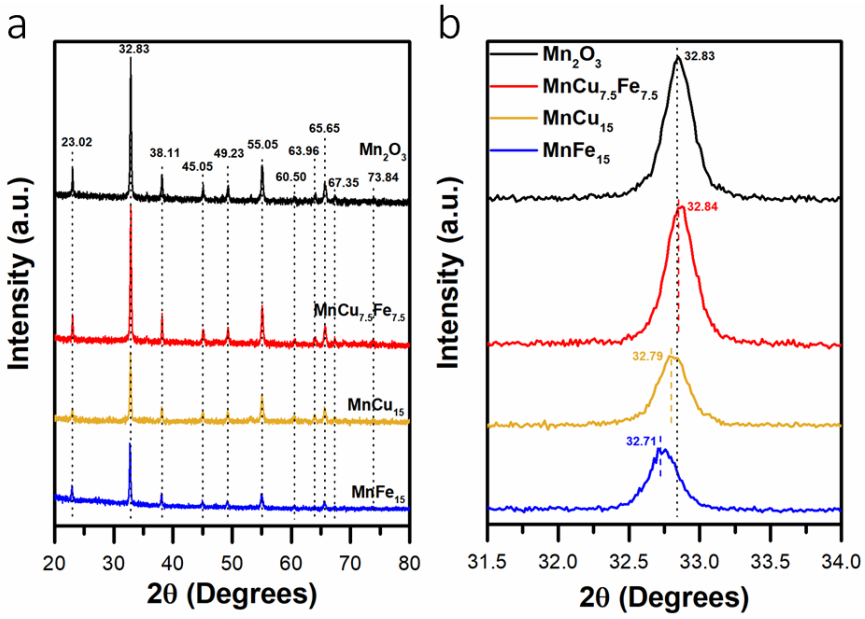

Figure 5.2 (a) XRD diffractograms of the synthesized samples and (b) magnification of most the most intense signal. Reprinted from (Marin Figueredo, Piumetti, Fino, et al., 2021).

5.3 Temperature-programmed analyses (H_2-TPR and soot-TPR)

The profiles corresponding to the consumption of H_2 of the prepared oxides, as a function of the temperature are summarized in Figure 5.3. The Mn_2O_3 catalyst (black line) evidences two reduction maxima located at 352 °C and 486 °C. The former is attributed to the reduction step: $Mn_2O_3 \rightarrow Mn_3O_4$. Instead, the latter is ascribed to the reduction step: $Mn_3O_4 \rightarrow MnO$ (Delimaris & Ioannides, 2008; Marco Piumetti, Fino, et al., 2015; Santos et al., 2010). Interestingly, the H_2 consumption (calculated by means of signal deconvolution) is equivalent to 6.99 mmol g^{-1} (reported in Table 5.2). Nevertheless, the theoretical consumptions for the $Mn_2O_3 \rightarrow MnO$ step and the $MnO_2 \rightarrow MnO$ are: 6.33 mmol g^{-1} and 11.50 mmol g^{-}

[1], respectively. Accordingly, this finding indicates that Mn^{4+} cations are present in the analyzed catalyst, leading to the slight increase in H_2-uptake, compared to the theoretical amount.

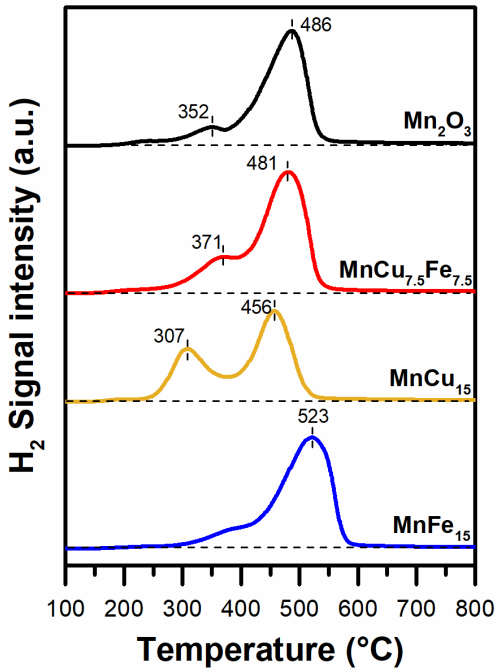

Figure 5.3 H_2-TPR analyses of the synthesized catalysts. Reprinted from (Marin Figueredo, Piumetti, Fino, et al., 2021).

The reduction signal of the $MnCu_{15}$ (magenta line), evidenced two intense peaks with maxima occurring at 307 °C and 456 °C. This highlights that the formation of the mixed Mn-O-Cu lattice promotes the reduction of the parent Mn_2O_3 at lower temperatures. The literature reports that the reduction of Cu species may occur at ca. 210-300 °C (Marin Figueredo et al., 2020), therefore, the reduction signal appeared at 307 °C was attributed to the reduction of both Cu^{x+} and Mn^{3+} species. Instead, the reduction that takes place at higher temperature was assigned to the further reduction of Mn^{3+} cations. Accordingly, the $MnCu_{15}$ showed the best low-temperature reducibility, compared to the other prepared samples. This finding highlights the positive effect of Cu species doping the parent Mn_2O_3.

The reduction profile of the $MnFe_{15}$ (blue line) consisted in an intense signal centered at 523 °C and a side-peak starting at a lower temperature (ca. 300 °C). The translation of the former signal to a higher temperature, compared to the parent Mn_2O_3, indicates that when Fe^{x+} cations are inserted in the system, a chemical structure more resistant to reduction is formed. In this sense, and according to the literature, the signal appeared below 530 °C can be attributed to the variation of

oxidation state of Mn and Cu species (from 3+ to 2+). While, the signal occurred at T > 530 °C is ascribed to the following reduction: $Fe^{2+} \rightarrow Fe$ (Leith & Howden, 1988; T. Li et al., 2007).

Table 5.2 H_2-uptake of the synthesized catalysts during H_2-TPR analyses. Adapted from (Marin Figueredo, Piumetti, Fino, et al., 2021)

Sample	H_2 consumption (mmol g_{cat}^{-1})
Mn_2O_3	6.99
$MnCu_{15}$	7.22
$MnFe_{15}$	8.25
$MnCu_{7.5}Fe_{7.5}$	8.48

The reduction signal of the $MnCu_{7.5}Fe_{7.5}$ (red line) consisted as well in two intense signal centered at 371 °C and 481 °C. This trend is similar the reduction of the parent Mn_2O_3. Nevertheless, an increased H_2-uptake took place below 400 °C, and a slight shifting of the most intense reduction was observed. In this sense, the reduction signal evidenced an intermediate trend respect to the $MnFe_{15}$ and the $MnCu_{15}$ catalysts. Accordingly, the reduction signal appeared at lower temperature was assigned to the reduction $Cu^{x+} \rightarrow Cu^0$ and, as well, to the initial reduction of Fe^{3+} and Mn^{3+} cations. Instead, the contribution appeared at higher temperature was ascribed to the further reduction of the Mn and Fe cations.

Table 5.3 Soot burnt (mg) during soot-TPR analyses Adapted from (Marin Figueredo, Piumetti, Fino, et al., 2021)

Sample	Soot burnt $^{300\text{-}550\ °C}$ (mg)	Soot burnt $^{550\text{-}700\ °C}$ (mg)
Mn_2O_3	0.73	1.09
$MnCu_{15}$	0.71	1.18
$MnFe_{15}$	0.81	1.14
$MnCu_{7.5}Fe_{7.5}$	0.72	1.12

The reducibility by soot of the synthesized oxides (soot-TPR analyses) is reported in Figure 5.4, in terms of produced CO_2 and CO. Concerning produced CO_2, a reduced-intensity signal was observed at about 150 °C-300 °C. While at higher temperature, the signal appeared comprises a rather complex ensemble of peaks. The former can be attributed to the release carbon dioxide (probably atmospheric) adsorbed in basic sites of the manganese oxides (Gandhe, Rebello, Figueiredo, & Fernandes, 2007). Considering that there is no O_2 in the gaseous feed,

the latter signal corresponds to CO and CO_2 resulting from soot oxidation occurred by means of oxygen species present in the catalyst. The literature reports that the oxidation happening at about 350-450 °C takes place by means of surface chemisorbed O_2^- species, whereas between 450 and 550 °C soot oxidation takes place due to more electronegative oxygen, e.g. O_2^{2-} or O^- (Z. Li et al., 2012; Spinicci & Tofanari, 1990). Above 550 °C the highest oxidation rate occurs due to the reduction of the metal species in the bulk. In fact, the slow release of structural lattice oxygen present in the bulk coincides with the appearance of unconverted CO.

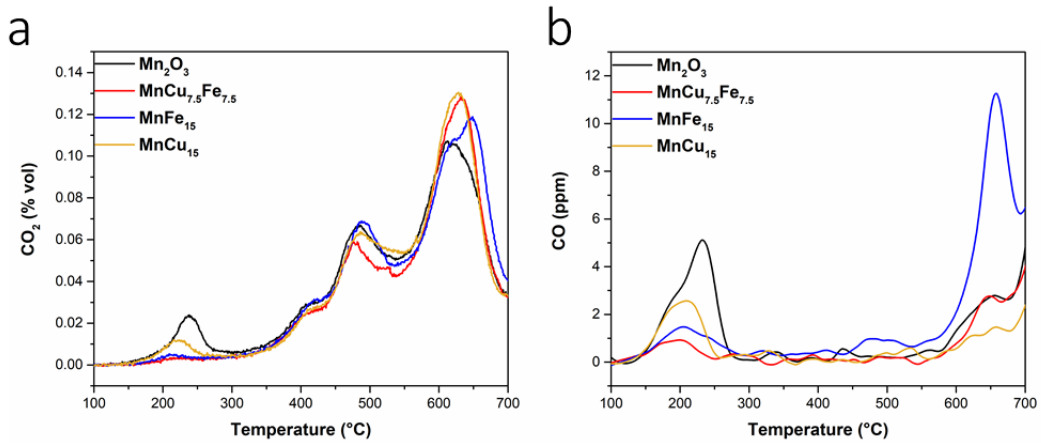

Figure 5.4 Soot-TPR investigations carried out on the synthesized catalysts. Reprinted from (Marin Figueredo, Piumetti, Fino, et al., 2021).

Table 5.3 summarizes the amounts of soot oxidized in the soot-TPR analyses. Considering the prior discussion, the quantity of soot burnt in the 300-550 °C range is associated to the oxidation by means of active surface-chemisorbed oxygen species. Consistently, those values are indicative of the catalyst's ability to start the catalytic oxidation of soot at low temperatures. Instead, above 550 °C soot oxidation takes place due to the reduction occurring in the bulk of the catalyst. In this sense, it can be stated that the incorporation of the foreign metals (Cu and/or Fe) enhances the reducibility of the synthesized MnO_x by soot according to the following trend: $Mn_2O_3 < MnCu_{7.5}Fe_{7.5} < MnFe_{15} < MnCu_{15}$.

5.4 X-ray photoelectron spectroscopy

The various spectra harvested via XPS analyses are reported in Figure 5.5. Section a shows the spectra in the Mn 2*p* core level along with their corresponding deconvolution. The signal attributed to the $2p_{3/2}$ level appeared between 637.5-648.0 eV. While the signal at about 648.0-658.0 eV spectra is related to the $2p_{1/2}$

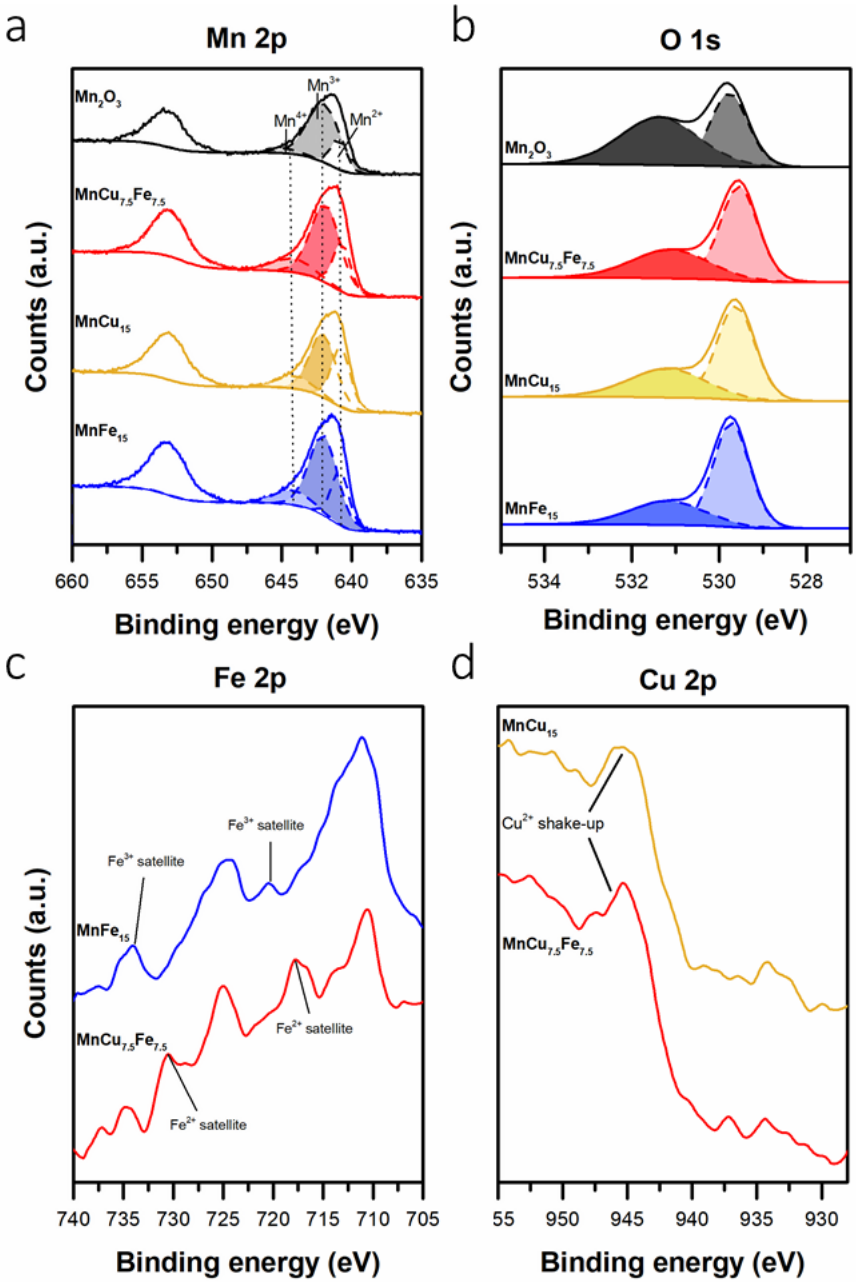

Figure 5.5 XPS spectra harvested in the (a) Mn 2*p*, (b) O 1*s*, (c) Fe 2*p* and (d) Cu 2*p* core level. Reprinted from (Marin Figueredo, Piumetti, Fino, et al., 2021).

level. Several investigations reported in the literature that the relative amounts of manganese species (namely, Mn^{4+}, Mn^{3+} and Mn^{2+}) may be estimated by means of the $2p_{3/2}$ level signal deconvolution (Biesinger et al., 2011; Marco Piumetti, Fino, et al., 2015; Santos et al., 2010). In this sense, the signal contributions observed between 640.7-640.9 eV correspond to the Mn^{2+}, between 641.8-642.1 eV to the

Mn^{3+} and between 644.1-644.8 to the Mn^{4+} cation. The relative amounts corresponding to each Mn^{x+} specie, as derived from spectra deconvolution are summarized in section a of Figure 5.6. It evidences that introducing iron and/or copper inside the MnO_x structure elevated the number of manganese species with higher oxidation state (Mn^{4+}) in the surface of the catalyst. This behavior puts a light on the role of Fe and Cu in the appearance of more oxidized Mn species. Noteworthy, the catalyst containing the highest loading copper (namely, the $MnCu_{15}$) evidenced a high population of Mn with lower oxidation state, i.e., Mn^{2+} species.

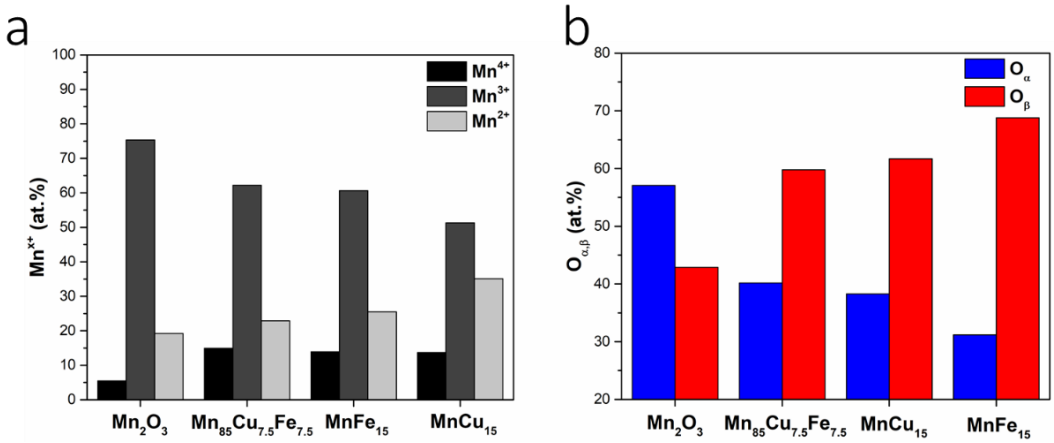

Figure 5.6 Relative abundances of (a) Mn^{x+} and (b) oxygen species (O_α and O_β), as derived from the deconvolution of the harvested Mn 2*p* and O 1*s* core level spectra, respectively. Reprinted from (Marin Figueredo, Piumetti, Fino, et al., 2021).

The spectra harvested in the O 1*s* core level and the corresponding deconvolution are reported in section b of Figure 5.5. As a whole, the spectra consist in two peaks located at different binding energies. Each signal is related to different oxygen species, as follows: surface chemisorbed oxygen (O_α-species) and structural lattice (O_β) oxygen (thus the O^{2-} bonded to metals). In this sense, the signal between 529.4-529.9 eV was assigned to nucleophilic O_β species bonded to Mn, Fe or Cu (Moulder et al., 1992). Instead, the signal between 531.2-531.5 eV was assigned to electrophilic O_α-species like O_2^-, O^- and to OH groups (Kim & Shim, 2010; Santos et al., 2010). As shown in section Figure 5.6 (section b), the parent Mn_2O_3 showed the highest number of O_α-species and, as a consequence, the highest O_α/O_β ratio (ca. 1.33). Concerning the samples containing Cu^{x+} species (thus the $MnCu_{7.5}Fe_{7.5}$ and $MnCu_{15}$ catalysts), similar O_α/O_β ratios (0.67 and 0.62 respectively) were observed, while the $MnFe_{15}$ evidenced the lowest value for the same ratio (ca. 0.45).

The spectra reported in section c of Figure 5.5 were harvested in the Fe 2*p* core level region. The region between 707.0-717.0 eV corresponds to the $2p_{3/2}$ level, whereas the signal corresponding to the $2p_{1/2}$ level appeared at about 723.0-728.8 eV. The literature remarks that the presence of iron species (e.g., Fe^{2+} and Fe^{3+}) can be evaluated by detecting the $2p_{1/2}$ level signal and the corresponding satellites (Biesinger et al., 2011; Yamashita & Hayes, 2008). The spectra of the $MnCu_{7.5}Fe_{7.5}$ and the $MnFe_{15}$, evidenced intense peaks centered at ca. 710.7 and 711.1 eV respectively. Moreover, satellites related to the Fe^{3+} specie were detected (mostly in the $MnFe_{15}$), thus highlighting the presence of an increased number of Fe^{3+} in both catalysts. On the other hand, the spectrum of $MnCu_{7.5}Fe_{7.5}$ catalyst showed satellites at about 716.9 and 730.6 eV correlated to Fe^{2+} species. Noteworthy, the appearance of reduced Fe^{2+} coincides with high amounts of oxidized Mn^{4+} species over the $MnCu_{7.5}Fe_{7.5}$ catalyst (vide supra). This may propose that the contemporary substitution of structural Mn^{3+} species with iron and copper can increase the occurrence reduced Fe^{2+} species in the catalytic surface.

The spectra harvested in the Cu 2*p* core level are reported in section d of Figure 5.5. As reported in the literature, the signal attributed to the $2p_{3/2}$ level occurred at about 930.0-937.0 eV. The signal present in this region aids in estimating the oxidation state of the superficial Cu^{x+} species and, in turn, for the eventual quantification (in terms of relative abundance) (Biesinger et al., 2010; Kundakovic & Flytzani-Stephanopoulos, 1998; W. Liu & Flytzani-Stephanopoulos, 1995a; Marco Piumetti, Bensaid, Andana, Russo, et al., 2017). Though the reduced intensity of the spectra does not consent an accurate quantification of the different Cu^{x+} species, shake-ups attributed to Cu^{2+} species were detected in both spectra. Therefore, suggesting that Cu^{2+} species are present in the surface of these catalysts, i.e. Cu species with 2+ oxidation state.

5.5 Catalytic activity

5.5.1 Carbonaceous matter (soot) oxidation

The catalytic results harvested during the soot oxidation tests in “loose” contact tests are summarized in Figure 5.7. Accordingly, the prepared catalysts carried out the oxidation of soot at temperatures below those needed for the thermal oxidation pathway, in other words the non-catalyzed reaction. The soot converted to CO_x during both the catalyzed and uncatalyzed tests are included in sections a,b of Figure 5.7. During the non-catalytic test (green dotted line), the combustion of soot

produces relatively high amounts of CO, i.e., a highly unselective conversion takes place in absence of a catalyst. Nevertheless, minimal outflowing amounts of CO were observed during the oxidation tests in presence of the prepared catalysts. Accordingly, this highlights the high selectivity of the synthesized oxides towards the complete oxidation of the carbonaceous matter.

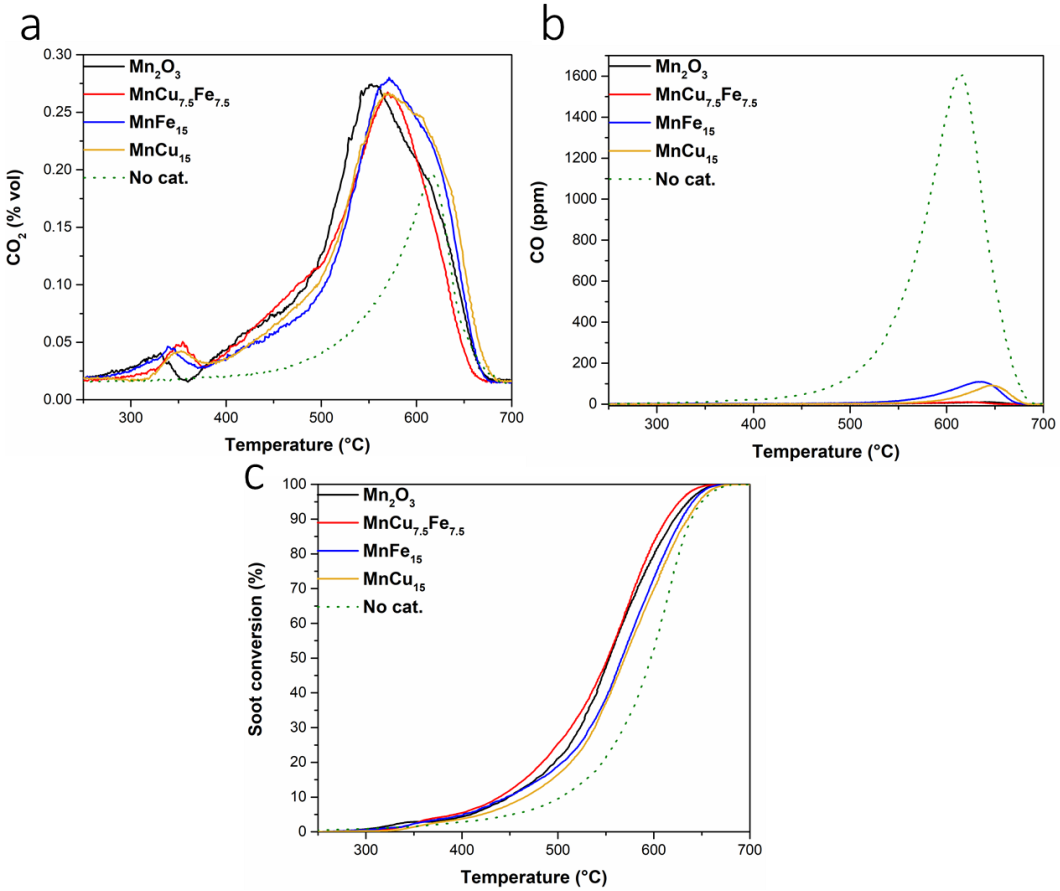

Figure 5.7 Amounts produced of (a) CO_2 and (b) CO and (c) the corresponding conversions (%) as a function of the temperature occurred during soot oxidation screenings carried out in "loose" contact conditions over the synthesized catalysts. Reprinted from (Marin Figueredo, Piumetti, Fino, et al., 2021).

As a whole, during the catalytic tests two signals (CO_2) appeared at low temperatures (ca. 200 °C and 340 °C). The former signal was attributed to CO_2 species adsorbed on superficial basic sites (previously discussed in the soot-TPR section, vide supra), therefore it was not counted for calculating the converted soot. Instead, the latter signal was assigned to the catalytic oxidation of soot that occurred in "tight" contact condition with the catalysts. Noteworthy, considering that the catalytic beds were prepared by means of a standard "loose contact" procedure, this contribution was unexpected. Consistently, this highlights that a physico-chemical

property of the prepared catalysts could have promoted the occurrence of soot-catalyst "tight" contact points and, as a consequence, enhanced the oxidation of soot at lower temperature. The literature reports that well-defined nanostructures can promote catalytic activity in soot oxidation at low temperatures by means of an enhanced number of catalyst-soot contact points (Andana et al., 2016; Marco Piumetti, Bensaid, et al., 2015). The performances of the synthesized catalysts during the soot oxidation screenings (in terms of $T_{X\%}$ and reaction rates) are summarized in Table 5.4. According to the performances observed (in terms of the temperature required for converting 50% of the soot in the reactor, thus the $T_{50\%}$) rather similar performances, and the best, were observed for both the Mn_2O_3 and $MnCu_{7.5}Fe_{7.5}$ catalysts. Conversely, the performance (according to the $T_{X\%}$ and the reaction rate) of the $MnCu_{15}$ was the worst among the synthesized catalysts. In this sense, the following decreasing trend for the catalytic performance can be outlined: $Mn_2O_3 \approx MnCu_{7.5}Fe_{7.5} > MnFe_{15} > MnCu_{15}$. Excluding the $MnFe_{15}$ catalyst, the suggested trend is accordance with the relative amounts of superficial O_α-species (as estimated by means of XPS analyses, vide supra).

Table 5.4 Soot oxidation performances of the synthesized catalysts in terms of $T_{10\%}$, $T_{50\%}$, $T_{90\%}$ and reaction rates. Adapted from (Marin Figueredo, Piumetti, Fino, et al., 2021)

Sample	$T_{10\%}$ (°C)	$T_{50\%}$ (°C)	$T_{90\%}$ (°C)	r_{soot}[a] (mmol h^{-1} g^{-1})
Mn_2O_3	449	553	622	2.10
$MnCu_{15}$	466	570	636	1.42
$MnFe_{15}$	447	567	630	1.54
$MnCu_{7.5}Fe_{7.5}$	440	552	613	1.91

[a]calculated at 415 °C

The literature has reported that the catalytic activity of different oxide materials takes place by means of superficial redox cycles, in which structural oxygen participates, i.e. the Mars-van Krevelen reaction mechanism (Mars & van Krevelen, 1954; Marco Piumetti, Bensaid, Andana, Russo, et al., 2017). For this reaction pathway the enhanced mobility of oxygen plays a key role, i.e., better reducibility along with the presence of high number of structural defects should improve the oxidative performance (Marin Figueredo et al., 2020; Marco Piumetti, Bensaid, Andana, Russo, et al., 2017; Marco Piumetti, Fino, et al., 2015). Nevertheless, the catalytic activity trend outlined in this investigation could not be assigned to the better reducibility of the catalysts occurred due to the doping of the MnO_x with Cu

and/or Fe. On the other hand, the reaction rates for the soot oxidation reaction seem correlated to the ratio of Mn^{3+}/Mn^{2+} species (estimated by means of Mn 2*p* core level spectra deconvolution). Accordingly, the rate of soot oxidation decreased when amount of reduced Mn^{2+} species is higher (see Figure 5.8). The trend was assessed with a linear fitting (see solid red line), whereas the dashed red lines denote the 95% confidence bands. This finding suggests that the oxidative performance of the catalyst seems compromised by a high number of reduced Mn^{2+} species. In fact, a previous research work evidences that high amounts of reduced Mn^{2+} species worsened the oxidative performance of oxide catalysts (Marin Figueredo et al., 2020). In this sense, this investigation strongly suggests that, under the studied reactive environment, Mn^{2+} cations present in the catalyst do not actively participate reactive redox pathway.

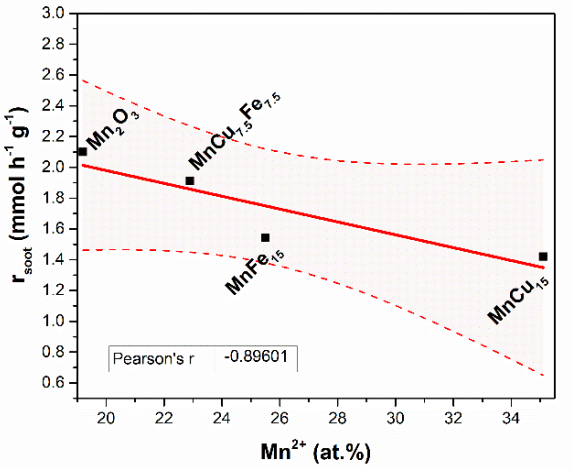

Figure 5.8 Decreasing trend of the reaction rates in soot catalytic oxidation over the synthesized catalysts as a function of the relative amount of reduced Mn^{2+} species. Reprinted from (Marin Figueredo, Piumetti, Fino, et al., 2021).

Moreover, the most promising catalysts, i.e. the $MnCu_{7.5}Fe_{7.5}$ and the Mn_2O_3, were investigated in soot oxidation catalytic tests carried out under "tight" contact soot-catalyst conditions (see Figure 5.9). In the graphs, the solid lines correspond to the results of the screening carried out in "loose" contact condition, while the dashed lines correspond those observed under "tight" contact conditions. As a whole, the CO_2 signal (section a, Figure 5.9) occurred at lower temperature values ca. 400 °C, compared to the test performed under "loose" contact.

Similarly, the signal of produced CO (section b, Figure 5.9) appeared at lower temperatures. As well, the amount of CO produced was lower, compared to the "loose" contact tests. In this scenario, the catalytic conversions observed in "tight" contact conditions (section c, Figure 5.9) highlight the catalytic superiority of the

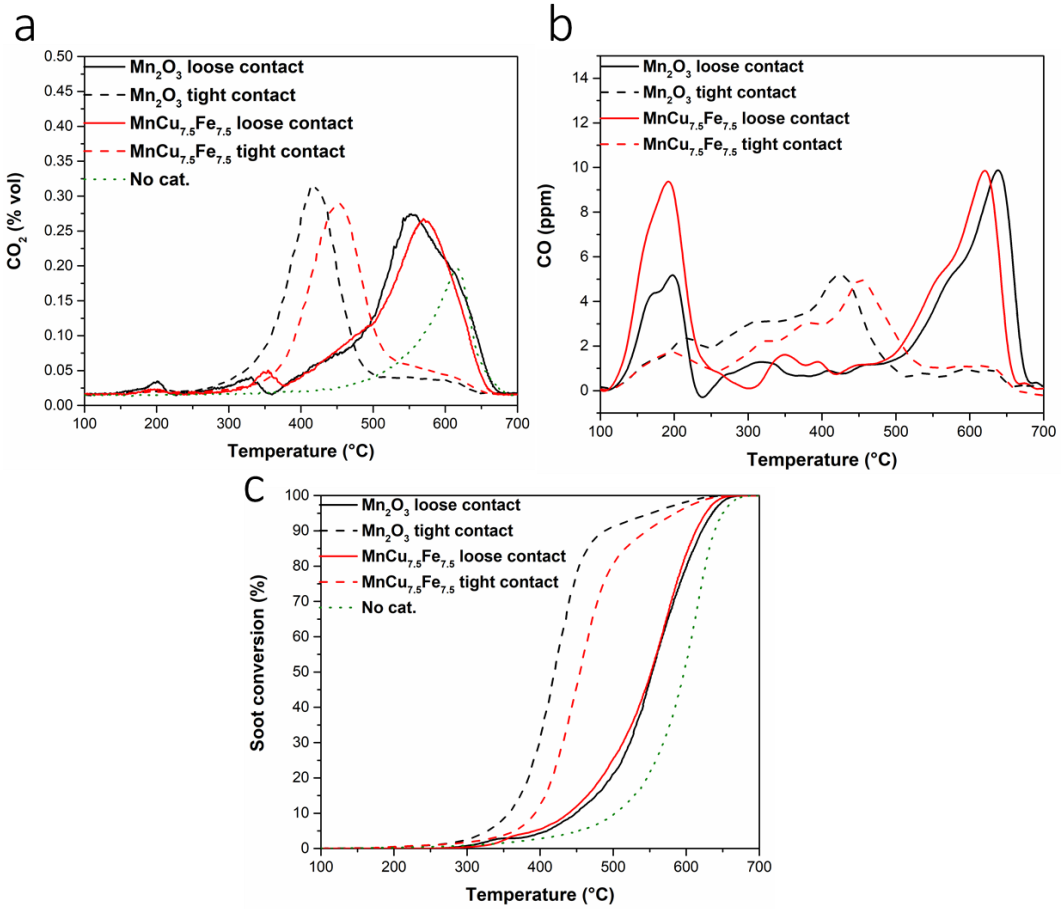

Figure 5.9 Amounts produced of (a) CO_2 and (b) CO and (c) the corresponding conversions (%) as a function of the temperature occurred during soot oxidation screenings carried out in "tight" contact conditions over the Mn_2O_3 and the $MnCu_{7.5}Fe_{7.5}$ catalysts. Reprinted from (Marin Figueredo, Piumetti, Fino, et al., 2021).

parent Mn_2O_3 ($T_{50\%}$ = 420 °C) compared to the $MnCu_{7.5}Fe_{7.5}$ oxide ($T_{50\%}$ = 455 °C). This finding further confirms that maximizing the soot-catalyst contact points highly enhance the performance of the catalysts. Noteworthy, over the Mn_2O_3 catalyst the oxidation reaction began at lower temperature (compared to the $MnCu_{7.5}Fe_{7.5}$). This is in accordance with the ability of the catalysts to initiate the soot oxidation reaction by means of surface-chemisorbed oxygen species, that in turn coincides with the trend of O_α/O_β observed in the XPS analyses (vide supra). Therefore, these findings highlight the paramount role of the chemisorbed oxygen species for the occurrence of catalytic soot oxidation at low temperatures.

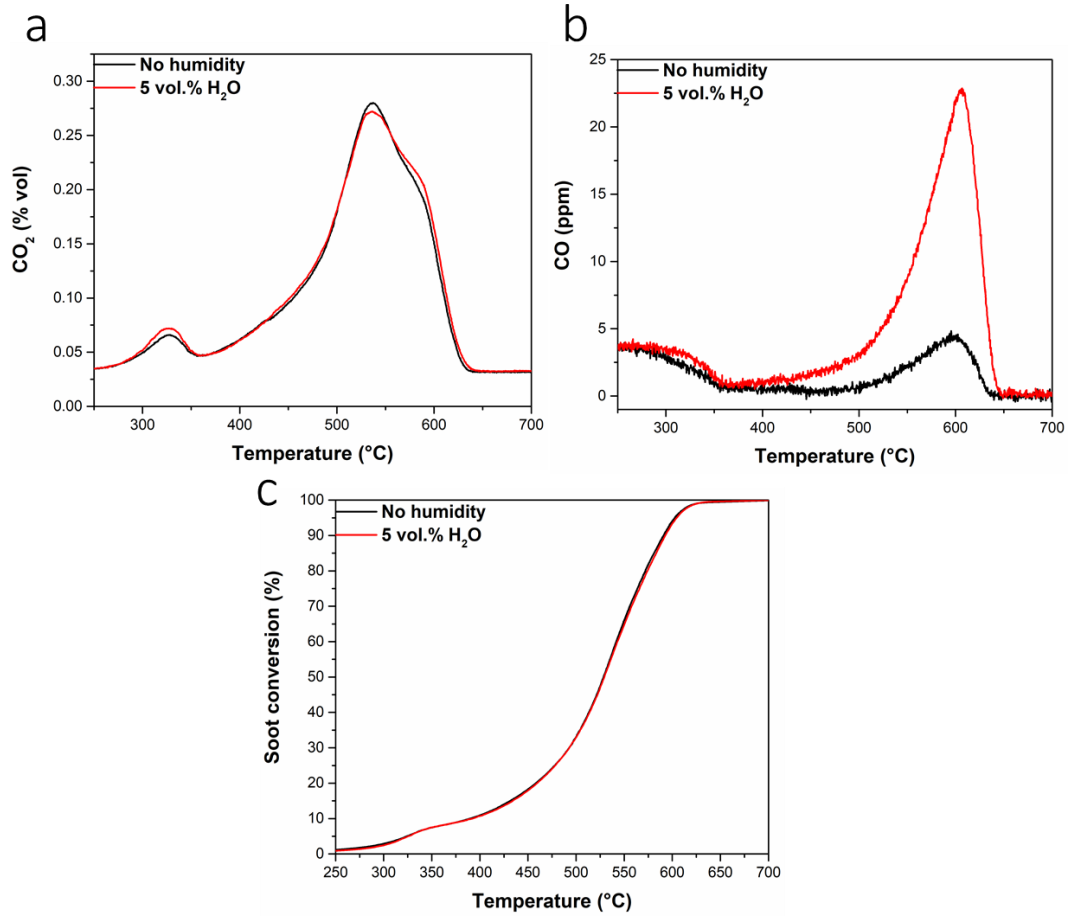

Figure 5.10 Amounts produced of (a) CO_2 and (b) CO and (c) the corresponding conversions (%) as a function of the temperature occurred during soot oxidation screenings carried out in "loose" contact conditions over the Mn_2O_3 in presence of 5 vol.% of water. Reprinted from (Marin Figueredo, Piumetti, Fino, et al., 2021).

Moreover, an assessment regarding the catalytic stability of the most promising catalysts (the Mn_2O_3 and $MnCu_{7.5}Fe_{7.5}$) was carried out. For the study, the catalysts were previously aged at high temperature (ca. 750 °C, 4 h). The graphical catalytic stability results are not reported for brevity reasons, and are available for consultation in the published paper (Marin Figueredo, Piumetti, Fino, et al., 2021). As a whole, a CO_2 side peak signal occurred at ca. 615 °C can be noticed during the catalytic screening of both aged catalysts. As well, the production of CO became noticeable. These signals took place in the temperature region at which the non-catalytic thermal conversion of soot occurs. Accordingly, the results suggest that a slight deactivation of the low-temperature catalytic activity took place. The deteriorated performance was ascribed to a probable sintering process suffered by the catalysts during the ageing treatment. In fact, the thermal procedure changed

importantly surface areas available, from ca. 13 $m^2 g^{-1}$ to 6 $m^2 g^{-1}$ in both cases (see Table 5.1). Furthermore, the ageing process could have induced changes in the monolithic-like morphology of the catalysts or, as well, the reduction of the population of O_α-species, that proved to be beneficial in the soot oxidation reaction.

Finally, the catalytic performance of the best catalyst (the Mn_2O_3) was studied under a stream containing 5 vol.% of humidity. In Figure 5.10 are summarized the results obtained in the screenings. Noteworthy, the produced CO_2 observed under both conditions are rather similar (see section a, Figure 5.10). Nevertheless, the side peak observable at about 615 °C evidenced a slight increased intensity when water was present in the gaseous inlet. Similarly, increased amounts of CO compared to the test in "dry" conditions, were verified in the aforementioned temperature region. Consistently, this suggests that non-catalytic soot oxidation may occur in presence of water. Nevertheless, these findings reveal that the presence of H_2O in the gaseous reactor-inlet has a practically negligible effect over the catalytic soot oxidation over the Mn_2O_3. Thus demonstrating, at some extent, the resistance of the catalytic activity of the Mn_2O_3 catalyst to water vapors in the gaseous stream. These results agree with other investigation reported in the literature (Christensen et al., 2017; Peralta, Milt, Cornaglia, & Querini, 2006).

5.5.2 Propylene oxidation

The catalytic soot conversions exhibited by the synthesized catalysts in the propylene oxidation screenings (as a function of the temperature) are summarized in Figure 5.11. Moreover, the corresponding performances were included in Table 5 in terms of C_3H_6 reaction rate and the temperatures: $T_{10\%}$, $T_{50\%}$ and $T_{90\%}$.

Table 5.5 Catalytic performances of the synthesized catalysts in propylene oxidation reaction, in terms of $T_{10\%}$, $T_{50\%}$, $T_{90\%}$ and reaction rates. Adapted from (Marin Figueredo, Piumetti, Fino, et al., 2021).

Sample	$T_{10\%}$ (°C)	$T_{50\%}$ (°C)	$T_{90\%}$ (°C)	r_{pr}[a] (µmol h^{-1} m^{-2})
Mn_2O_3	182	213	236	3.83
$MnCu_{15}$	178	212	236	5.86
$MnFe_{15}$	181	212	234	5.30
$MnCu_{7.5}Fe_{7.5}$	180	214	237	5.36

[a]calculated at 170 °C

The $T_{X\%}$ demonstrated by the doped catalysts during the propylene abatement tests did not show a noteworthy variation compared to those observed for the parent Mn_2O_3. On the other hand, the estimated specific reaction rates were observed to increase when the parent oxide was doped with Cu and/or Fe. Remarkably, the highest reaction rate was observed in the catalyst that showed (in H_2-TPR analysis) the best low-temperature reducibility, thus the $MnCu_{15}$ catalyst. Accordingly, these findings suggest that incorporating Cu and/or Fe (as foreign metals) in the structure of Mn_2O_3 (as XRD analyses revealed) can enhance its activity in VOCs catalytic oxidation. As reported in the literature, the synthesis mixed manganese-oxides comprising other transition metals may increase the amount of oxygen vacancies, and therefore enhance the formation of defective oxide structures (María Roxana Morales, Barbero, & Cadús, 2006, 2008). Accordingly, these parameters are most likely the key aspects for the improved catalytic activity observed in C_3H_6 oxidation by the doped-MnO_x materials investigated in this work.

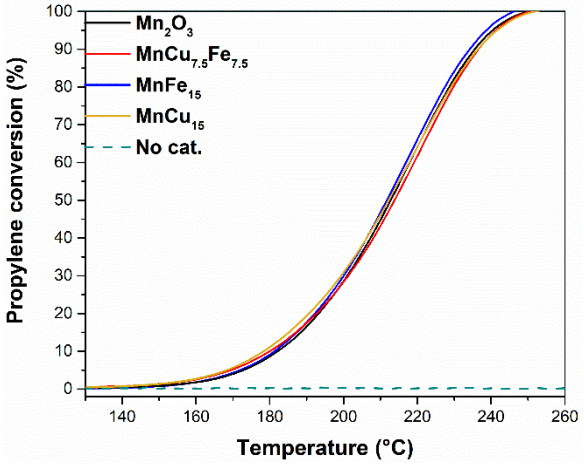

Figure 5.11 Conversions (%) of propylene over the synthesized catalysts, for the propylene catalytic oxidation reaction as a function of the temperature. Reprinted from (Marin Figueredo, Piumetti, Fino, et al., 2021).

The reproducibility of the catalytic performance over the most active catalyst (the $MnCu_{15}$), by means of two consecutive oxidative tests. The graphical results are not reported for brevity reasons, and available for consultation in the published paper (Marin Figueredo, Piumetti, Fino, et al., 2021). No significant variation in the catalytic performance was observed between the first and the second catalytic runs.

As well, the long-term catalytic stability of the $MnCu_{15}$ was investigated in a time on stream (TOS) test at swinging temperature conditions. The catalytic conversions registered in the aforementioned test are reported in Figure 5.12.

Overall, no deactivation of the catalytic performance of the $MnCu_{15}$ was observed under the swinging temperature conditions during the 7 h on stream. Moreover, the catalytic conversion evidenced a stable behavior after 1 h in the different stages of the test. Accordingly, the catalytic activity was confirmed to be stable and reproducible in relatively long period while being subject to cyclic temperature conditions.

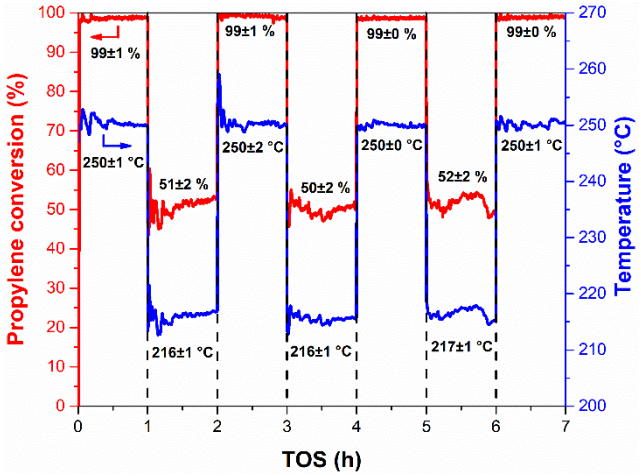

Figure 5.12 Propylene catalytic conversion (%) over the $MnCu_{15}$ as a function of the TOS under swinging temperature operative conditions. Reprinted from (Marin Figueredo, Piumetti, Fino, et al., 2021).

As well, the catalytic activity of the $MnCu_{15}$ in the propylene oxidation reaction was assessed under a gaseous stream containing 5 vol.% of H_2O. The curves reported in Figure 5.13 compare the catalytic results (C_3H_6 oxidation) observed under dry conditions and those with 5 vol.% humidity. Remarkably, almost no variation was observed in the overall catalytic performances in spite of the humidity present in the gaseous stream. Nevertheless, a slight decrease of the propylene conversion can be observed in the low-temperature region when water is present in the reactor gaseous feed. This result suggests that the adsorption of H_2O molecules could be occurring onto the sites active for the oxidation reaction. In this sense, other authors have attributed this condition to molecules of water competitively adsorbing on the active sites of the oxide material, leading to a slight worsening of the catalytic VOC oxidation (FANG, CHEN, XIA, XI, & LI, 2009; W. B. Li, Wang, & Gong, 2010). As a conclusion, it can be stated that the overall performance of the $MnCu_{15}$ catalyst for the C_3H_6 oxidation reaction remains practically unvaried under a gaseous stream containing 5 vol.% of H_2O.

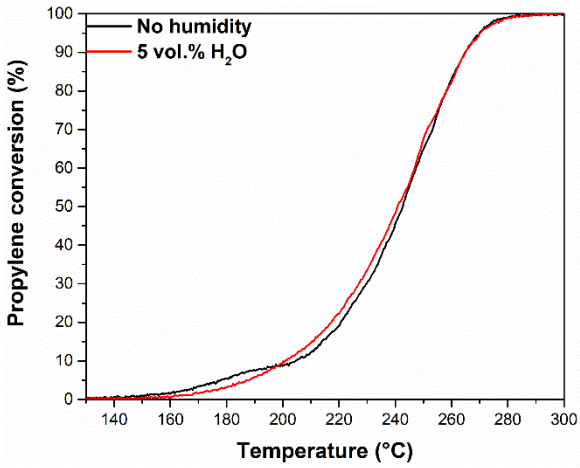

Figure 5.13 Comparison of the catalytic performances of the $MnCu_{15}$ catalysts in the propylene oxidation reaction without humidity and in presence of 5 vol.% of H_2O in the stream. Reprinted from (Marin Figueredo, Piumetti, Fino, et al., 2021).

Further studies were carried out to better investigate the propylene oxidation reaction kinetics over the $MnCu_{15}$ catalyst. Accordingly, isothermal tests (at 150, 160, 170 and 180 °C) were performed, in which the C_3H_6 concentration of the reactor inlet was varied between 75 ppm, 100 ppm, 200 ppm, 300 ppm and 500 ppm. For these tests, a high excess of O_2 (ca. 10 vol.%), diluted in N_2 was maintained. During the tests, operative conditions analogous to those of the propylene oxidation tests were used. A fairly linear increase of the oxidation rates (see section a, Figure 5.14) was observed when the propylene inlet concentration was increased. As well, the higher the temperature of the test, the higher the observed. Additionally, the effect changing the oxygen inlet concentration over the oxygen reaction rate was assessed at 160 °C (see section b, Figure 5.14). For the latter test, an inlet C_3H_6 concentration of 500 ppm was maintained. The rate of O_2 consumption was estimated by means of the CO and CO_2 outflowing from the reactor, and thus related to the catalytic oxidation reaction. This test highlighted an increasing rate of O_2 consumption under conditions with high excess of propylene in the stream. Instead, above 1 vol.% of O_2 the consumption rate did not show relevant variations. The observed mostly constant consumption suggests oxygen could have saturated the catalytic surface. Remarkably, this finding highlight that the activity of the $MnCu_{15}$ catalyst in the C_3H_6 oxidation reaction remains practically unchanged when the inlet O_2 amount ranges between 1 and 10 vol.%. Particularly, a higher O_2 consumption rate occurred when the inlet concentration was 1 vol.%. This outcome may suggest that different catalytic phenomena could be taking place, e.g., better adsorption of the VOC in competitive sites or a higher availability of structural-lattice oxygen as in a Mars-van Krevelen reaction

mechanism. In fact, the latter possibility seems probable, since the incorporation of copper in the framework of Mn_2O_3 (as confirmed by XRD studies, vide supra) enhanced the lattice oxygen mobility, as demonstrated by the reducibility analyses (H_2 and soot-TPR).

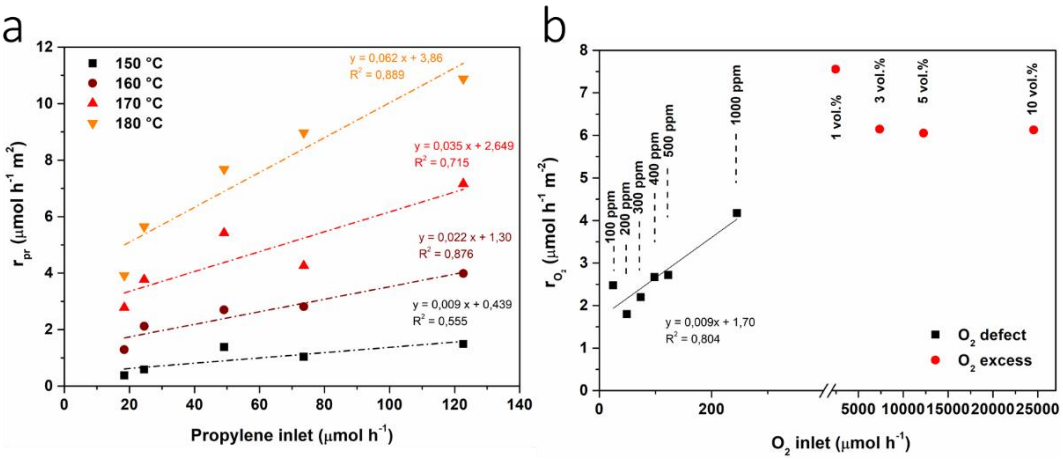

Figure 5.14 (a) C_3H_6 reaction rates (at 10 vol.% O_2) as a function of the C_3H_6 fed in the reactor inlet in various temperature conditions and (b) O_2 reaction rate (at 500 ppm C_3H_6) as a function of the O_2 fed in the reactor inlet. Reprinted from (Marin Figueredo, Piumetti, Fino, et al., 2021).

5.5.3 Simultaneous oxidation of soot and propylene

A comparison was performed between the catalytic performances observed in screenings for (i) only propylene oxidation and (ii) simultaneous soot and propylene oxidation over Mn_2O_3. The results harvested, in terms of CO_2 and CO are summarized in sections a and b of Figure 5.15. Observing the CO_2 profiles from both tests, overlapping signals are observed in the region at which the VOC oxidation takes place, after which soot oxidation takes place. Consistently, it seems that the signal of the soot+C_3H_6 oxidation test consists in the sum of the signals observed during the separated C_3H_6 oxidation test and the soot oxidation test. Interestingly, this suggests that the oxidation of the VOC and soot can occur contemporarily. Moreover, it seems that there are no negative effects of one process above the other. Under this scenario, the catalytic conversion of only soot (blue dashed line) was compared to the soot conversion under a stream containing C_3H_6 (black solid line), see section c of Figure 5.15. Remarkably, a higher amount of soot converted during the simultaneous soot-C_3H_6 catalytic oxidation test (at about 350 °C), compared to the one converted in the only-soot oxidation test.

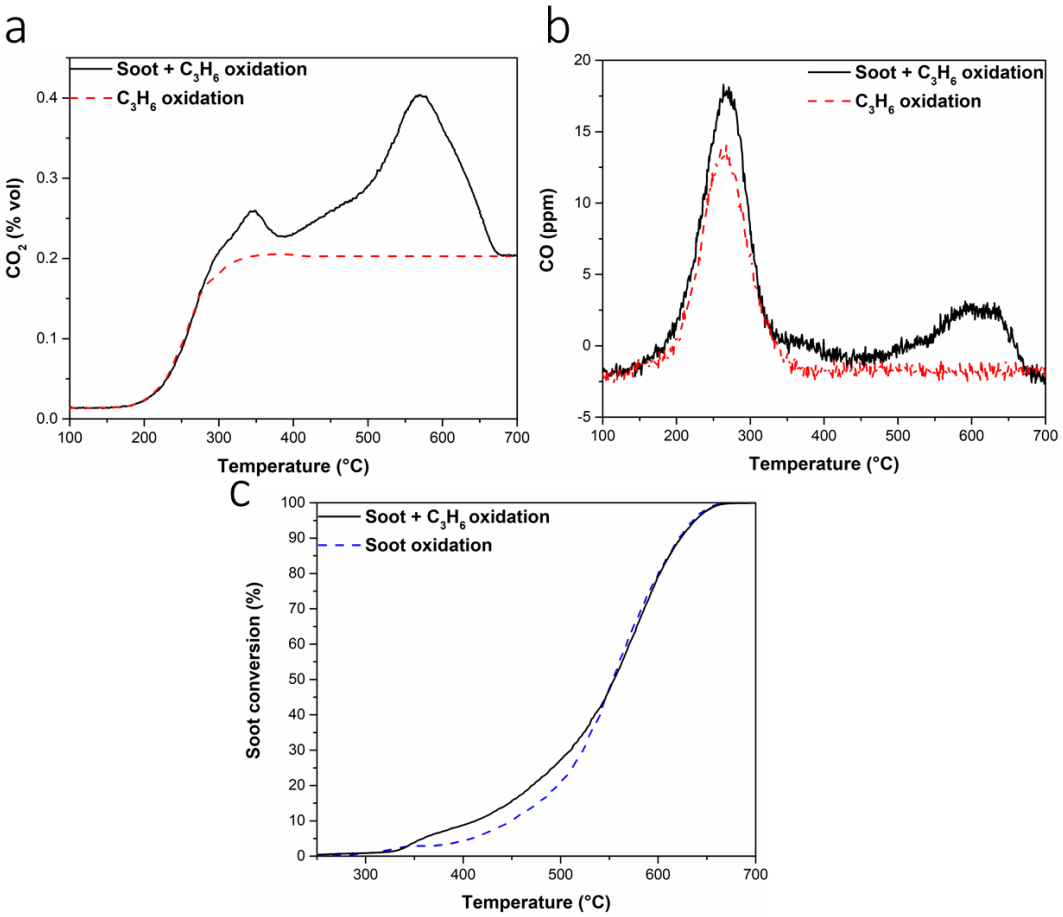

Figure 5.15 Amounts produced of (a) CO_2 and (b) CO and as a function of the temperature occurred during the oxidation screenings for propylene and propylene + soot performed in "loose" contact conditions. (c) catalytic conversions (%) of soot in presence (black solid line) and in absence of C_3H_6 (blue dashed line), as a function of the temperature. Reprinted from (Marin Figueredo, Piumetti, Fino, et al., 2021).

As well, the simultaneous soot-C_3H_6 catalytic oxidation was investigated under a stream containing 5 vol.% of H_2O, see Figure 5.16. Like in the previously discussed tests, in the soot-C_3H_6 oxidation tests in presence of humidity the CO_2 signal (see section a of Figure 5.16) overlapped the CO_2 signal corresponding to the oxidation test of propylene in presence of water (red dashed line). Consistently, it was attributed to C_3H_6 oxidation occurring independently from the soot oxidation process. Above 280 °C, the shape of the produced CO_2 profile observed is similar to the one occurred in soot oxidation test over Mn_2O_3, achieving peaks maxima at comparable temperatures (see section a of Figure 5.7). Nevertheless, additional CO_2

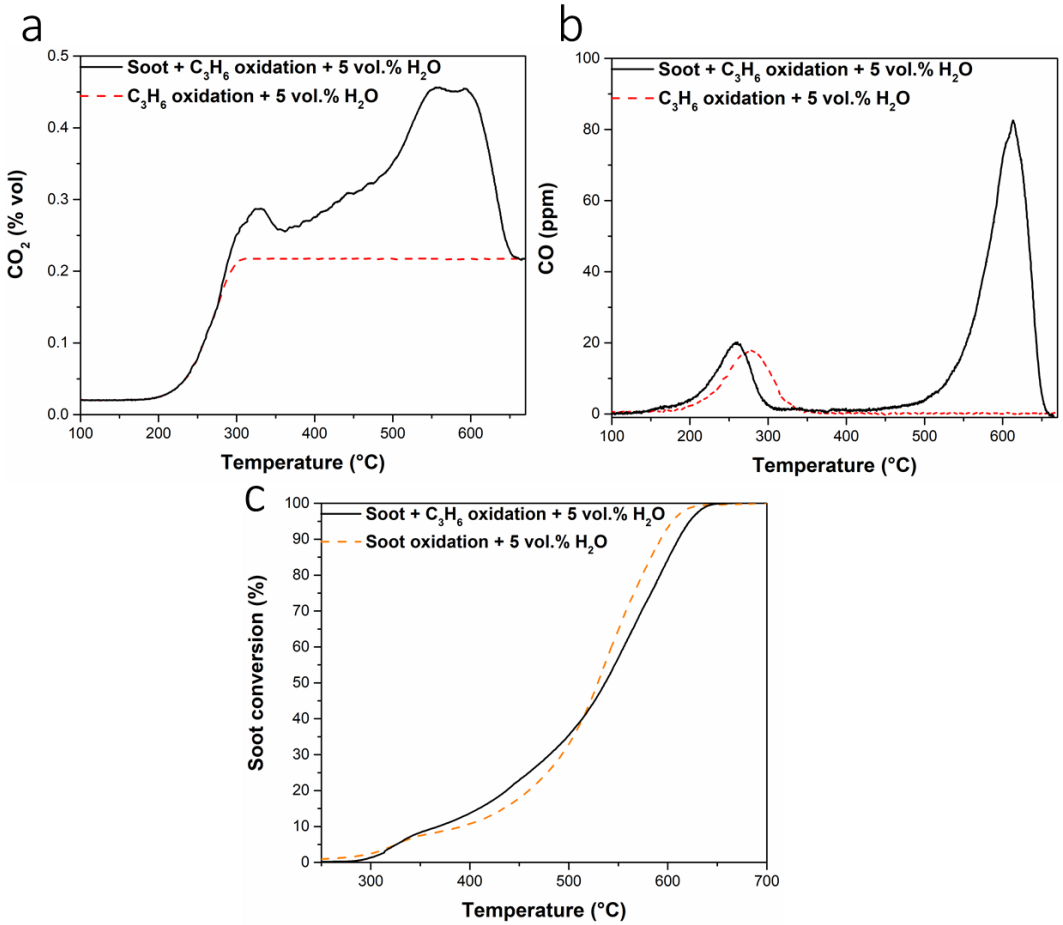

Figure 5.16 Amounts produced of (a) CO_2 and (b) CO and as a function of the temperature occurred during the oxidation screenings for propylene and propylene + soot carried out in "loose" contact conditions under 5 vol.% of H_2O. (c) catalytic conversions (%) of soot in presence (black solid line) and in absence of C_3H_6 (blue dashed line), as a function of the temperature with 5 vol.% of H_2O in the stream. Reprinted from (Marin Figueredo, Piumetti, Fino, et al., 2021).

and CO signals appeared at about 600 °C (see sections a and b of Figure 5.16). Accordingly, it seems that an increased amount soot particles is converting through thermal oxidation. Consistently and according to the literature this was attributed to the presence of humidity that probably promoted the deactivation of the catalyst (Peralta et al., 2006). Interestingly, below 515 °C an apparently higher amount of soot converted (black solid line), compared to the amount converted in the test in which C_3H_6 is not present (see section c of Figure 5.16). This outcome coincides with the one reported in section c of Figure 5.15. As mentioned earlier, soot oxidation occurring in that temperature region was attributed to the conversion of

soot particles in "tight" contact with the catalyst. In fact, other authors have reported a higher rate of soot oxidation may occur under "tight" contact conditions under a stream containing VOCs (Aouad, Abi-Aad, & Aboukaïs, 2009)(Godoy et al., 2018). These findings highlight the possible beneficial interactions that could be occurring between both the C_3H_6 and soot catalytic oxidation processes occurring in the surface of the catalyst. Actually, other investigation (Aouad et al., 2009) has confirmed that the low-temperature soot oxidation could be induced by means of the ignition of the exothermal C_3H_6 oxidation reaction. In this context, the exothermal VOC oxidation reaction could be generating local temperature enhancements over the surface of the catalyst, thus causing some soot oxidation in the low temperature region.

Overall, these findings provide strong proof for presuming that C_3H_6 oxidation occurs in spite of the soot particles present in the reactor. Moreover, the outcome of the test for the simultaneous soot-VOC oxidation remarks that the propylene catalytic oxidation reaction may assist the soot oxidation process. In this sense, the partial elimination of a higher number of soot particles may take place at temperatures lower than those needed in absence of the VOC.

5.6 Conclusions

A set of doped-Mn_2O_3 catalysts were synthesized through the sol-gel preparation technique using citric acid. The catalysts were doped with transition metals (Cu and/or Fe) and defined as follows: $MnCu_{15}$, $MnFe_{15}$ and $MnCu_{7.5}Fe_{7.5}$. Overall, the experimental results of the soot oxidation tests revealed the parent Mn_2O_3 as the most performing catalyst. The most promising catalyst evidenced good and stable catalytic activity in oxidation tests before and after being severely aged (thermally) and, as well, under a stream containing ca. 5 vol.% humidity. The catalytic activity in soot oxidation was associated to the ratio of Mn^{3+}/Mn^{2+} species present in the surface of the catalyst. Therefore, highlighting the important role played by reducible Mn species in catalytic soot oxidation.

As well, the $MnCu_{15}$ catalyst evidenced the best overall performance in the catalytic propylene oxidation reaction. Consecutive catalytic tests revealed the reproducibility of the $MnCu_{15}$ catalytic performance. Moreover, its catalytic stability was verified under a 7 h TOS experiment and swinging temperature conditions. Interestingly, almost no deactivation of the $MnCu_{15}$ catalyst was observed under a gaseous stream containing 5 vol.% of humidity. The improved catalytic activity was correlated to the better reducibility of the oxide, occurred due to the incorporation of copper (Cu) in the structure of Mn_2O_3.

Finally, screenings for the simultaneous soot-propylene oxidation in either in dry or humid conditions (5 vol.% of H_2O) were carried out. The tests revealed a fairly stable catalytic performance of the Mn_2O_3, since the soot and propylene oxidation reactions took place contemporarily. Remarkably, the results evidenced that the soot oxidation reaction seems promoted when propylene is being oxidized, therefore indicating that soot oxidation could be assisted by the mechanism of the propylene oxidation reaction.

Chapter 6

Catalytic abatement of VOCs and soot over Manganese Oxide Catalysts

6.1 Introduction

For this chapter, a set of MnO_x catalysts was prepared by means of two different synthesis techniques, the solution combustion synthesis (SCS) and the sol-gel (SG) technique. These procedures investigated allowed to prepare catalysts with different physico-chemical and catalytic properties. The elevated catalytic performances of the synthesized materials were validated in the oxidation reactions of VOC probe molecules (propene and ethene) and carbonaceous particulate matter (carbon soot).

The procedures used for the synthesis of the catalytic materials (solution combustion synthesis and sol-gel), along with the set of prepared catalysts is reported in section 2.2.1 and section 2.2.2. The study of the physico-chemical properties of the synthesized catalysts was carried out using several characterization techniques (as reported in section 2.3).

This chapter includes data resulting from my personal research and was published in: Marin Figueredo, M.J., Cocuzza, C., Bensaid, S., Fino, D., Piumetti, M., Russo, N. (2021). Catalytic Abatement of Volatile Organic Compounds and Soot over Manganese Oxide Catalysts. *Materials*, 14, page 4534. The publication and the copyright license are consultable at the following link:

https://www.mdpi.com/1996-1944/14/16/4534.

6.2 Material structural and textural properties

X-ray diffractometry studies were carried out, with the aim of revealing the crystalline phases in the catalysts. The diffraction date harvested were summarized in Figure 6.1.

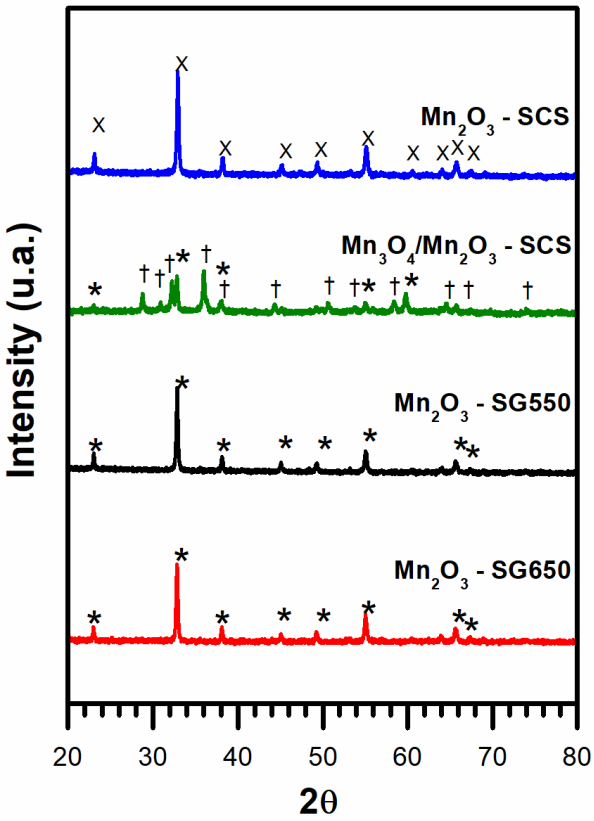

Figure 6.1 Diffractograms harvested during X-ray powder diffraction analyses. Assignments: Mn_2O_3 peaks = X and *; Mn_3O_4 = †. Reprinted from (Marin Figueredo, Cocuzza, et al., 2021).

The diffractograms of the Mn_2O_3-SG650 and Mn_2O_3-SG550 revealed the presence of the Mn_2O_3 cubic structure (according to the reference code 01-078-0390). Therefore, confirming that, regardless of the different calcination temperatures applied during the sol-gel synthesis, identical crystalline phases consisting in the Mn_2O_3 system are obtained. Instead, the diffraction pattern of the Mn_2O_3-SCS evidenced that the formation of an orthorhombic system of the Mn_2O_3

(according to the ref. code 01-073-1826) took place. Particularly, a mixed diffraction pattern was observed for the Mn_3O_4/Mn_2O_3 catalyst. Consistently, the catalyst is mainly formed by hausmannite (with ref. code 00-024-0734), nevertheless, further diffraction lines corresponding to Mn_2O_3 (with ref. code 01-078-0390) were observed.

The textural properties (as derived from N_2 physisorption at -196 °C analyses) are reported in Table 6.1. Accordingly, it can be observed that the SCS technique allowed the formation of higher specific surface areas (S_{BET}), compared to the SG preparation. Evidently, the formation of elevated specific surface areas denotes a positive outcome, because it may enhance the catalytic performances in gas-phase reactions by means of the eventual increased number of available active sites. Instead, the formation of larger crystallites was observed in the catalysts synthesized through the SG technique, compared to those prepared with the SCS.

The FESEM micrographs including the observed morphologies of the samples are reported in Figure 6.2.

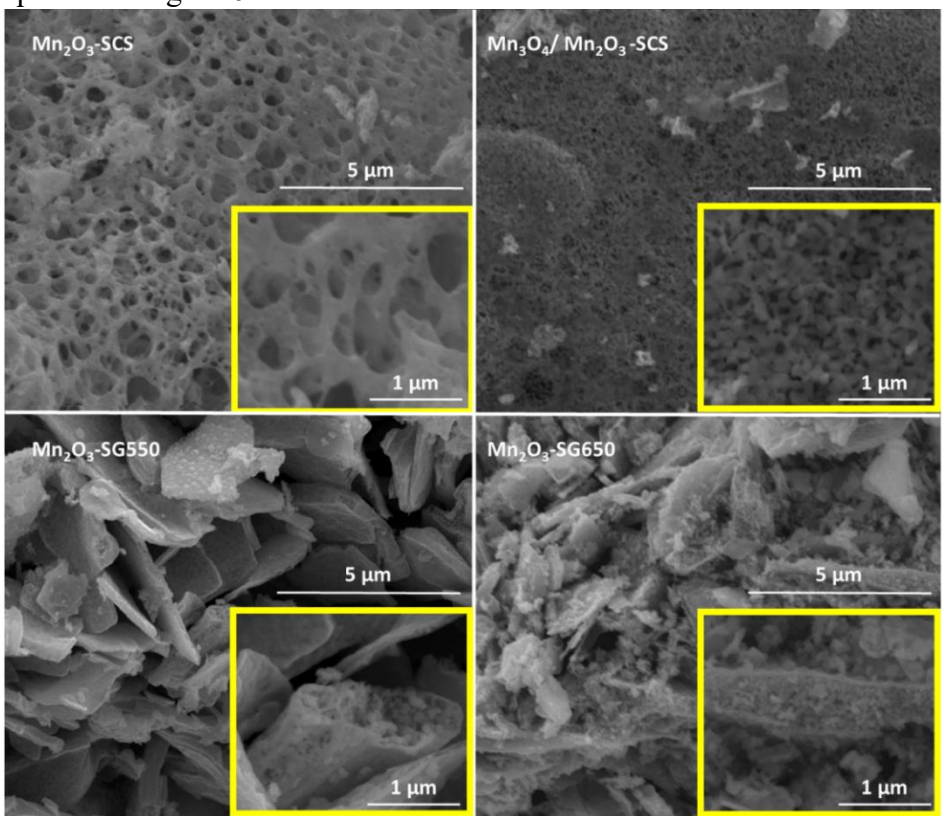

Figure 6.2 Morphologies of the synthesized catalysts (and their corresponding magnifications) as observed in FESEM analyses. Reprinted from (Marin Figueredo, Cocuzza, et al., 2021).

Table 6.1 Textural properties of the prepared samples catalysts. Adapted from (Marin Figueredo, Cocuzza, et al., 2021)**.**

Sample	S_{BET}[a] ($m^2\ g^{-1}$)	V_P[a] ($cm^3\ g^{-1}$)	D_P[a] (nm)	CS[b] (nm)
Mn_2O_3-SG550	15	0.12	32	67
Mn_2O_3-SG650	11	0.10	37	61
Mn_2O_3-SCS	22	0.15	26	52
Mn_3O_4/Mn_2O_3-SCS	21	0.13	23	37 / 53

Estimated by means of [a] N_2 physisorption at -196 °C and [b] Scherrer formula. S_{BET}: specific BET surface area, V_P: total pore volume, D_P: pore diameter, CS: size of crystallites

As a whole, the images revealed that both preparation techniques allowed the formation of mesoporous structures. Particularly, the images evidenced that the nanoplates obtained through the sol-gel synthesis consisted in an internal hollowed structure contained in an external shell. As well, highly porous structures were observed in catalysts prepared by means of the SCS, which coincided with the highest S_{BET}. This evidences that that the formation of the typical SCS sponge-like structures leads to higher surface areas, respect to the SG counterpart. In fact, the sample synthesized via SG synthesis were consisted in (visibly less porous) slim nanoplates.

6.3 Temperature-programmed analyses (H_2-TPR and soot-TPR)

Reducibility analyses (H_2-TPR) were carried out over the catalysts flowing 5 vol.%-H_2 in Ar, while the temperature was changed in the 100-800 °C range. The signals corresponding to the reduction are summarized in Figure 6.3. As a whole, the catalysts formed by Mn_2O_3 evidenced a two-peak reduction behavior. In this sense, the peak-signal appeared in the 350–383 °C range was attributed to the following reduction step $Mn_2O_3 \rightarrow Mn_3O_4$. Instead, the signal appeared at higher temperatures was ascribed to the following reduction step: $Mn_3O_4 \rightarrow MnO$ (Aguilera et al., 2011; Delimaris & Ioannides, 2008; Kapteijn et al., 1994; Marco Piumetti, Fino, et al., 2015). Accordingly, the mentioned reducibility tests further confirmed the increased number Mn species with 3+ as oxidation state (thus Mn^{3+}) in the Mn_2O_3 samples (as revealed by the XRD studies). Furthermore, the enhanced formation of large crystallites in the SG preparation technique (calculated through the Scherrer formula) seemed correlated to the reduced intensity of the first reduction signal (thus, the low-temperature peak), and the occurrence of the second signal at higher temperature values. As reported in the literature, the formation of

larger Mn_2O_3 particles may result in an increased resistance to reduction (Marco Piumetti, Bensaid, Andana, Dosa, et al., 2017; Marco Piumetti, Bensaid, Andana, Russo, et al., 2017).

The slight reduction signal observed in the Mn_3O_4/Mn_2O_3-SCS that appeared around 300 °C may be ascribed to the Mn^{3+} species of Mn_2O_3 crystals present in the sample, as revealed through XRD studies (vide supra). Accordingly, an overall reducibility trend (according to the observed low-temperature reduction peak) was outlined: Mn_2O_3-SG550 > Mn_2O_3-SCS > Mn_2O_3-SG650 > Mn_3O_4/Mn_2O_3-SCS.

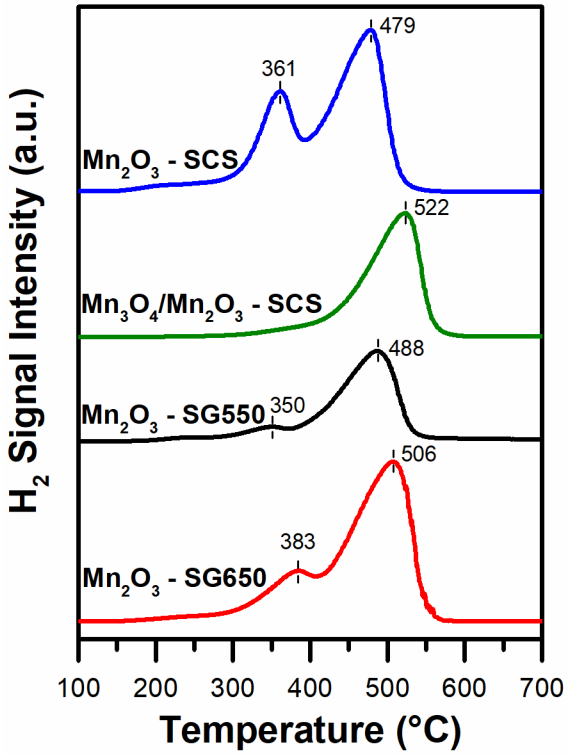

Figure 6.3 Reducibility analyses (H_2-TPR) over the prepared catalysts. Reprinted from (Marin Figueredo, Cocuzza, et al., 2021).

Reducibility analyses of the catalysts by soot were carried out under tight contact condition, therefore in absence of oxygen (reported in Figure 6.4). During these tests, the oxidation of soot occurred by means of the oxygen species present in the catalyst. Several peaks of CO_2 were appeared during the analyses. The signal at the lowest temperature occurred at about 240 °C (observed only in the Mn_2O_3-SG550 catalyst). This signal was ascribed to the desorption of CO_2 that is bonded to the basic sites of the manganese oxide (Gandhe et al., 2007). The signal appeared above 450 °C was ascribed to soot oxidation ($C + O_\alpha \rightarrow CO + O_\alpha \rightarrow CO_2$) by means

of chemisorbed O_2^-, whereas the signal appeared in the 450 - 550 °C range was ascribed to other electrophilic oxygen (like O^- and O_2^{2-}) (Z. Li et al., 2012; Spinicci & Tofanari, 1990). The signal that took place above 550 °C corresponds to soot oxidation by means of oxygen released from the bulk ($C + O_\beta \rightarrow CO + CO_2$), thus contemporaneous with the formation of CO (reported in section b of Figure 6.4). The latter signal occurs as a result of the slow oxygen diffusion between the bulk and the catalyst's surface, thus not allowing the further conversion of the reaction intermediate (thus the CO) to CO_2 (Andana et al., 2016). Noteworthy, a reduced signal intensity was observed for the catalysts calcined at 600 °C and 650 °C, compared to the signal observed for the only catalyst calcined at 550 °C, i.e., the Mn_2O_3-SG550. Such outcome proposes that higher calcination temperatures could have stabilized the catalyst's crystalline structure, therefore resulting in an overall lower reducibility. Accordingly, the following overall trend for the reducibility of the samples by soot was outlined: Mn_2O_3-SG550 > Mn_2O_3-SG650 ≈ Mn_2O_3-SCS ≈ Mn_3O_4/Mn_2O_3-SCS.

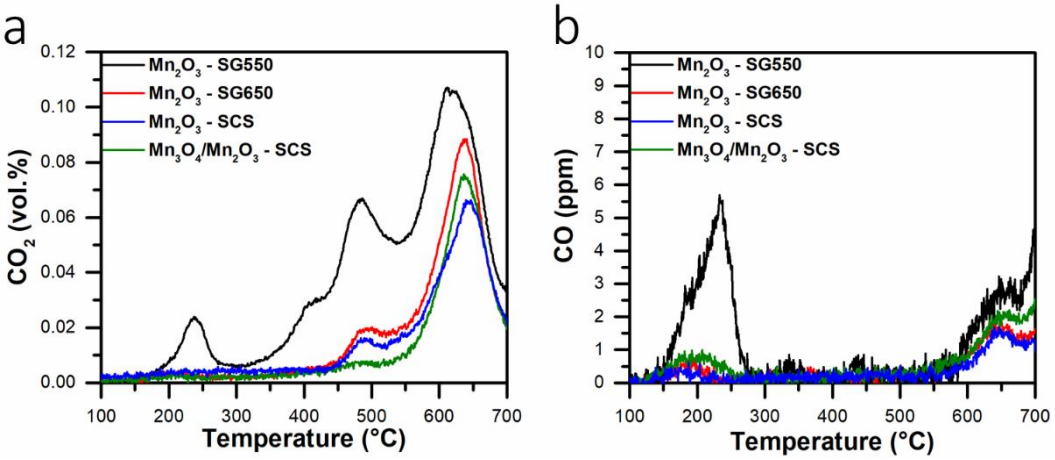

Figure 6.4 Profiles of (a) CO_2 and (b) CO observed in the soot-TPR analyses of the synthesized catalysts. Reprinted from (Marin Figueredo, Cocuzza, et al., 2021).

6.4 X-ray photoelectron spectroscopy

The spectra harvested in the XPS analyses are reported in Figure 6.5. The spectra (and the corresponding deconvolution) included in section a of Figure 6.5, correspond to the O 1*s* core level. Overall, the spectra evidenced with two signal maxima at different values of binding energy (BE). These signals correspond to different oxygen species. The peak occurring at lower binding energy values (529.6-529.9 eV) are assigned to the nucleophilic lattice oxygen specie (O^{2-}) that is bonded to Mn (i.e. O_β species) (Moulder et al., 1992). Instead, the peak appeared

between 531.2 and 531.4 eV is associated to electrophilic oxygen species (like O_2^- or O^-) or OH groups present over the surface of the sample (Kim & Shim, 2010; Santos et al., 2010). By means of spectra deconvolution, the relative amounts of O_α and O_β species were estimated (see Table 6.2). Accordingly, the following decreasing trend was observed for the O_α/O_β: Mn_2O_3-SG550 > Mn_2O_3-SCS > Mn_2O_3-SG650 ≈ Mn_3O_4/Mn_2O_3-SCS. Noteworthy, the increased population of O_α species has been associated by other authors to the total oxidation of hydrocarbons (Y. Liu et al., 2014; Marco Piumetti, Fino, et al., 2015; Zawadzki & Trawczyński, 2011).

Table 6.2 Relative amounts of oxygen species (at.%) as derived from the O 1*s* core level spectra deconvolution. Adapted from (Marin Figueredo, Cocuzza, et al., 2021)

Sample	O_α, OH BE (eV)	O_α (at.%)	O_β BE (eV)	O_β (at.%)	O_α/O_β
Mn_2O_3-SG550	531.4	56.7	529.8	43.3	1.31
Mn_2O_3-SG650	531.2	31.8	529.6	68.2	0.47
Mn_2O_3-SCS	531.3	38.5	529.6	61.5	0.63
Mn_3O_4/Mn_2O_3-SCS	531.4	31.8	529.9	68.2	0.47

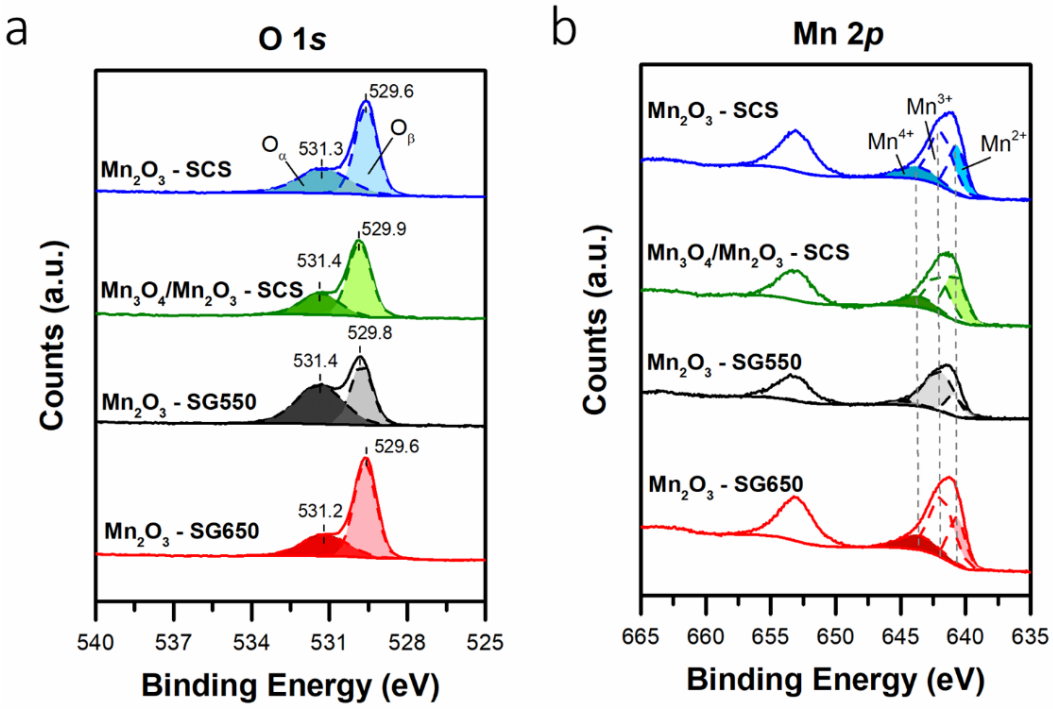

Figure 6.5 X-ray photoelectron spectra harvested in the (a) O 1*s* and (b) Mn 2*p* core level. Reprinted from (Marin Figueredo, Cocuzza, et al., 2021).

Moreover, the spectra harvested in the Mn 2*p* core level are summarized in section b of Figure 6.5. The signal appeared at higher BE is ascribed to the $2p_{1/2}$ level, instead, the signal contribution occurred in the 637.8-647.4 eV BE range, is attributed to the $2p_{3/2}$ level. Other authors have reported in the literature that a deconvolution can be performed for the latter contribution, in order to estimate the relative amounts of Mn^{x+} species (with x = 4+; 3+ and 2+) present in the catalyst (Biesinger et al., 2011; Marco Piumetti, Fino, et al., 2015; Santos et al., 2010). The deconvolution of the spectra (numerical data not reported for brevity reasons) confirmed the elevated amounts of Mn^{3+} species, and therefore their predominance, in the samples mainly composed by Mn_2O_3. Instead, the estimation on the number of Mn^{3+} and Mn^{2+} species in the Mn_3O_4/Mn_2O_3-SCS sample, as expected, consisted in similar amounts, since the mentioned catalyst in mainly composed by the Mn_3O_4 spinel.

6.5 Catalytic activity

6.5.1 VOC oxidation

The catalytic activity of the synthesized catalysts was investigated in the oxidation reactions of soot precursors (i.e., of VOCs). For the VOC catalytic tests, ethene and propene and ethene were the investigated probe molecules. The results of the catalytic VOC abatement tests are reported in section a of the Figure 6.6 and the Figure 6.7. As a whole, the synthesized catalysts converted the VOCs completely at low temperatures, compared to the case where no catalyst is present in the reactor. The calculated rates of VOC conversion by the prepared catalysts are reported in Table 6.3.

Table 6.3 Specific reaction rates for the ethene and propene catalytic oxidation reactions, over the synthesized catalysts. Adapted from (Marin Figueredo, Cocuzza, et al., 2021)

Sample	$r_{propene}$[a] (µmol h^{-1} m^{-2})	r_{ethene}[b] (µmol h^{-1} m^{-2})
Mn_2O_3-SG550	0.94	1.67
Mn_2O_3-SG650	0.49	1.13
Mn_2O_3-SCS	0.35	1.04
Mn_3O_4/Mn_2O_3-SCS	1.48	1.69

[a]calculated at 130 °C, [b]calculated at 160 °C

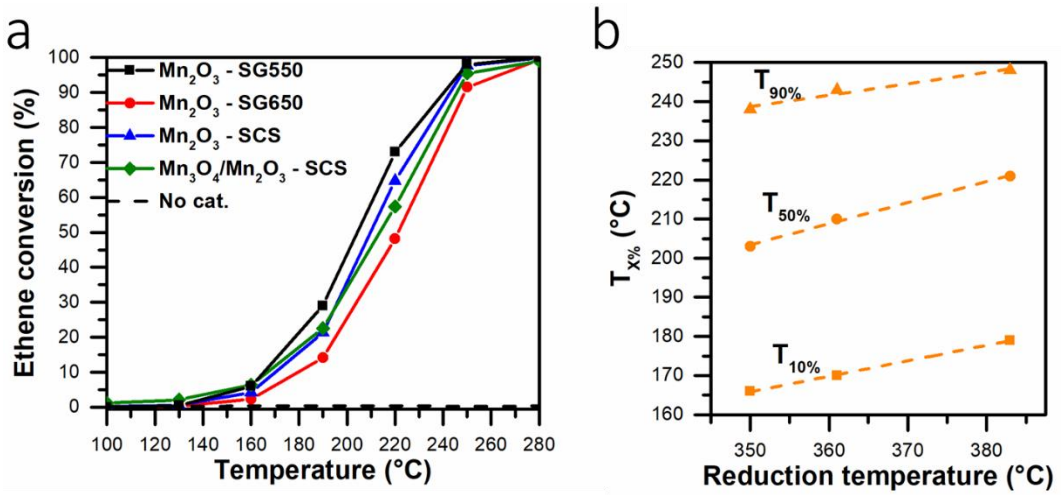

Figure 6.6 (a) Conversions (%) of propene as a function of the temperature over the prepared catalysts and (b) correlation between the low-temperature reduction signal and the catalytic performance in propene oxidation (over Mn_2O_3 catalysts) in terms of $T_{10\%}$, $T_{50\%}$ and $T_{90\%}$. Reprinted from (Marin Figueredo, Cocuzza, et al., 2021).

For the propene oxidation reaction, the following catalytic activity trend was outlined: Mn_3O_4/Mn_2O_3-SCS > Mn_2O_3-SG550 > Mn_2O_3-SCS > Mn_2O_3-SG650. As a whole, the materials prepared by means of the SG preparation evidenced better catalytic performances when a lower calcination temperature was utilized. In this sense, a higher calcination temperature may have promoted a sintering process that leads to a reduction of the catalyst's surface area (see Table 6.1). Accordingly, this outcome highlights the key role of the calcination condition (i.e., temperature) for the preparation materials catalytically active in VOCs oxidation. The structure of the catalyst that evidenced the best catalytic activity in the oxidation of propene was formed mainly by the spinel Mn_3O_4 (thus, coupled $Mn^{3+}|Mn^{2+}$ species). Moreover, this sample presented the smallest crystallite size observed in the prepared set of catalysts (ca. 37 nm for the Mn_3O_4). Consistently, the remarkable catalytic activity of the Mn_3O_4/Mn_2O_3-SCS may be attributed to the small crystallites of hausmannite present in the catalyst. In fact, according to the literature, the occurrence of small crystallites can lead to the occurrence of an elevated number of crystallite edges and corners, and therefore, the occurrence of more defective structures which are active in oxidation reactions (Dosa et al., 2018; M. Piumetti & Russo, 2017). Noteworthy, the catalysts formed by Mn_2O_3 (according to XRD analyses), the trend observed for the catalytic activity coincided with decreasing trends of the following parameters: (i) reducibility at low temperatures, and (ii) the amount of O_α-species chemisorbed on the surface of the catalyst. In effect, the data concerning the

catalytic performance in propene oxidation was fitted and evidenced a linear trend dependent on the temperature for the occurrence of the first reduction peak (see section b, Figure 6.6). This finding confirms the correlation between reducibility and the better catalytic activity in the oxidation C_3H_6 (in terms of $T_{10\%}$, $T_{50\%}$ and $T_{90\%}$, in other words the temperatures for reaching conversions of 10%, 50% and 90%, respectively).

Although the Mn_2O_3-SG550 catalyst presented an intermediate S_{BET} value compared to the other synthesized catalysts, it evidenced best catalytic performance for the ethene oxidation reaction (see section a of Figure 6.7). Taking into consideration the calculated reaction rates and the overall catalytic performances, the following catalytic activity trend was outlined for the oxidation of ethene: Mn_2O_3-SG550 > Mn_3O_4/Mn_2O_3-SCS > Mn_2O_3-SCS > Mn_2O_3-SG650. Overall, the catalytic activity seems correlated to the relative amount of active chemisorbed O_α-species (as confirmed by means of XPS analysis, vide supra) and (for the Mn_2O_3 catalysts) to the improved reducibility of the catalysts at low temperature (see section b, Figure 6.7).

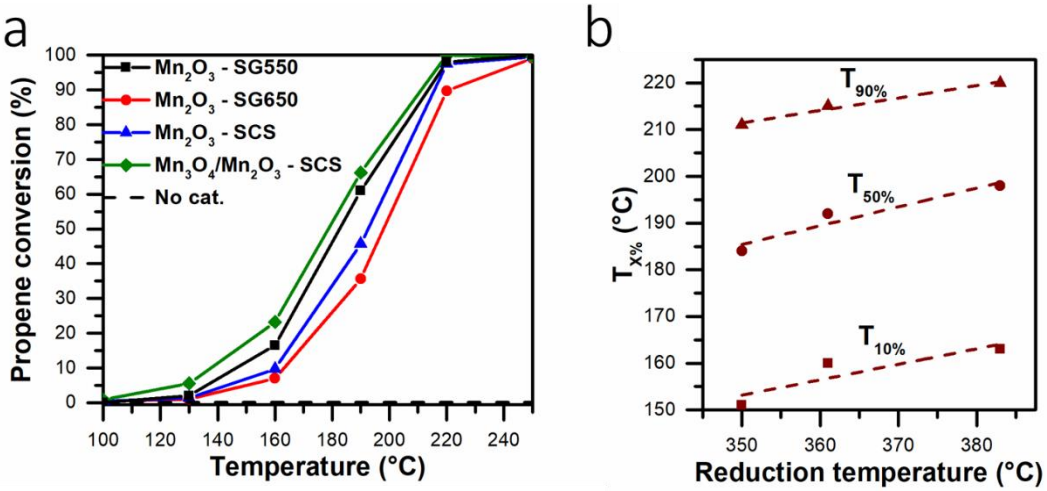

Figure 6.7 (a) Conversions (%) of ethene as a function of the temperature over the prepared catalysts and (b) correlation between the low-temperature reduction signal and the catalytic performance in ethene oxidation (over Mn_2O_3 catalysts) in terms of $T_{10\%}$, $T_{50\%}$ and $T_{90\%}$. Reprinted from (Marin Figueredo, Cocuzza, et al., 2021).

In this sense, the results highlight the key role played by both the reducibility of the catalyst and a high number of active O_α-species for the catalytic oxidation of ethene. Accordingly, the literature reports that increased amounts of these chemisorbed species, in conjunction with enhanced catalyst low-temperature

reducibility may promote the oxidation of VOCs at low temperatures (Marin Figueredo et al., 2020; Marco Piumetti, Bensaid, Andana, Russo, et al., 2017; Marco Piumetti, Fino, et al., 2015; Santos et al., 2010). The overall scenario observed during the catalytic abatement of the VOCs highlights that, catalysts belonging to the same group or family can present different catalytic performances depending on the abated molecule. This indicates that the catalytic activity for a given reaction may depend on a wide set of properties of the catalyst (e.g. reducibility, surface acidity, crystallites size, population of chemisorbed oxygen species, etc.). In this sense, it may be speculative to select a material as a catalyst for a given reaction taking into consideration a single physicochemical property or based on catalytic results obtained with other molecules. In conclusion, the synthesized catalysts evidenced good catalytic activity for the abatement of VOCs (i.e., carbon soot precursors), in a range of relatively low temperatures.

6.5.2 Carbonaceous matter (soot) oxidation

The synthesized materials were investigated in soot catalytic abatement tests, in tight or loose contact. The latter condition was achieved gently mixing the powders used in the test (inert silica, catalyst, and soot). On the other hand, intimate solid-solid interactions (in other words, tight contact conditions) were achieved performing a ball-milling process. The conversions observed during the soot oxidation tests are reported in Figure 6.8.

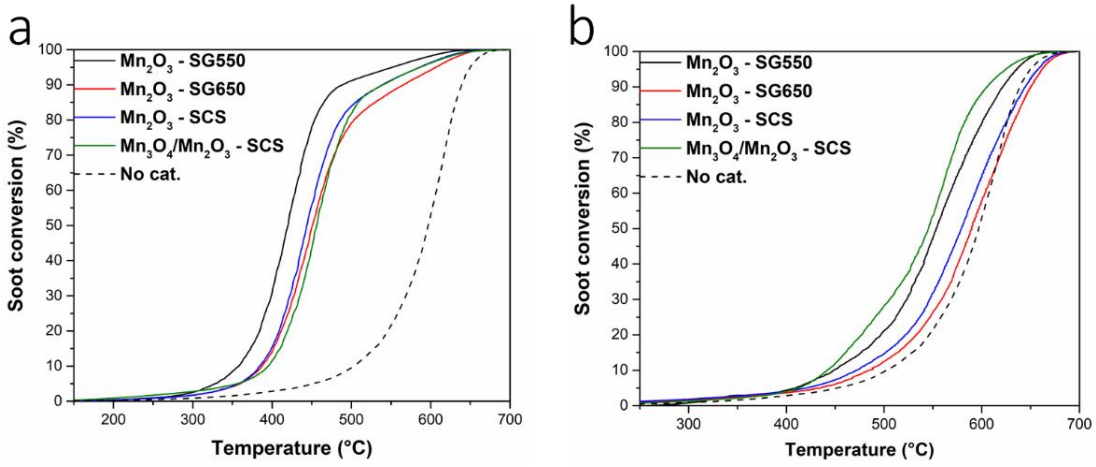

Figure 6.8 Soot catalytic conversions (%) under (a) "tight" and (b) "loose" contact conditions. Reprinted from (Marin Figueredo, Cocuzza, et al., 2021).

In the catalytic tests, the oxidation product was mostly carbon dioxide, whereas the formation of carbon monoxide remained low (or even unnoticeable) in most cases. Considering that soot oxidation is a solid-solid reaction, the enhancement of

the contact between the catalyst and soot plays a key role in order to better investigate the soot oxidation reaction kinetics (Marco Piumetti et al., 2016). Accordingly, the conversions observed under "tight" condition evidence the intrinsic activity of the catalytic surface. In this sense, the results observed in "tight" contact tests revealed that the active phase of the catalysts calcined at higher temperatures (above 600 °C; see the lines with blue, red, and green color) carried out the soot oxidation with similar performances. Conversely, the catalyst calcined at lower temperature (550 °C for the Mn_2O_3-SG550) outperformed the other synthesized catalysts. In fact, the Mn_2O_3-SG550 catalyst reached the 10% and 50% of soot conversion at temperatures ca. 25 °C below the other catalysts. These findings suggest that elevated calcination temperatures could have promoted the sintering of the catalyst and, as a consequence, have diminished the overall number of contact points present in the catalysts that are available for soot. As well, the catalysts that were calcined at higher temperatures presented diminished reducibility (as observed in soot-TPR analyses, vide supra), which is also associated to with their lower catalytic performances under "tight" contact conditions. Moreover, the best catalyst presented the highest relative amount of active O_α-species, which, according to the literature, are important in order to start the oxidation of soot (Fino et al., 2016). In this sense, the results highlight the high importance of elevated amounts of surface chemisorbed O_α species and of the improved catalyst reducibility for the carbon soot oxidation process.

On the hand, the catalytic tests under "loose" contact conditions are more representative of the contact conditions occurred in real catalytic traps (Marco Piumetti et al., 2016). The performances observed in the catalytic tests revealed similar catalytic activities in the case of the Mn_2O_3-SG650 and the Mn_2O_3-SCS catalysts. Nevertheless, in this contact condition, the catalyst containing the spinel Mn_3O_4 outperformed the catalytic activity Mn_2O_3-SG550 during the soot oxidation tests. This finding suggests that, although the former catalyst was treated at higher temperatures, the soot-Mn_3O_4 contact points enhanced importantly the catalytic performance. Moreover, this highlights the contact points were readily accessible for soot particles without favoring more intimate catalyst-soot contact conditions. This could be attributed to the sponge-like structure of the catalyst, characteristic of the solution combustion synthesis. That morphology (resembling a catalytic filter/trap) may have allowed an easier path for the soot particles to penetrate and remain trapped in the structure of the catalyst, compared to the hollowed nanoplates. In fact, this could have increased the occurrence of soot-catalyst contact

points for soot catalytic oxidation reaction. Noteworthy, previous research works evidenced that Mn_3O_4 (and mixed oxides comprising Mn_3O_4) host elevated amounts of acid sites, compared to other MnO_x materials (Deorsola, Andreoli, Armandi, Bonelli, & Pirone, 2016; Marco Piumetti, Fino, et al., 2015). Lewis acid sites consist in oxygen deficient superficial-metal cations. These sites may play a key role in the following oxidation process: adsorption of oxygen, its diffusion over the surface, and the final transfer to soot (oxidation). Consistently, the catalytic performance for the oxidation of soot can be correlated to these active sites (Wagloehner et al., 2014, 2015). Accordingly, the high catalytic activity (of the Mn_3O_4/Mn_2O_3-SCS catalyst) under "loose" contact was attributed to a combined promoting effect of the sponge-type morphology (that behaves as a powder filter or trap) and a probable increased number of acid sites in contact with soot. The overall results evidenced the remarkable efficacy of sustainable MnO_x-based materials in the abatement of carbonaceous particles and its organic precursors, thus the VOCs.

6.6 Conclusions

A set of MnO_x catalysts was prepared by means of two preparation techniques: the solution combustion synthesis (the Mn_3O_4/Mn_2O_3-SCS and the Mn_2O_3-SCS) and the sol-gel synthesis (the Mn_2O_3-SG550 and the Mn_2O_3-SG650). The preparation techniques allowed the synthesis of different catalysts, in terms of physicochemical and catalytic properties. As a whole, the best catalytic activities were performed by the Mn_2O_3-SG550 and the Mn_3O_4/Mn_2O_3-SCS catalysts. The catalysts were tested in the catalytic abatement of carbonaceous particulate matter and the VOCs. Regarding the catalytic elimination of VOCs (ethene and propene), the best catalytic performances were correlated to the following aspects:

1. The high number of active surface chemisorbed O_α species, that can importantly enhance the occurrence low-temperature total catalytic oxidation of hydrocarbons.

2. The promoted reducibility of catalysts at low temperature, and thus the improved mobility of the oxygen that participated in the oxidation reaction.

3. The occurrence of small crystallites, that can contain a high number of surface defects that promote the catalytic activity.

The effect of the mentioned parameters (1 and 2) on the catalytic oxidative activity of the studied materials for the abatement of carbonaceous particulate matter was demonstrated in this work. Consistently, under "tight" contact

conditions, the best catalytic activity for the soot oxidation reaction was observed in the catalyst that comprised the highest number of O_{α} species and exhibited better reducibility, thus the Mn_2O_3-SG550. This outcome highlighted the positive effect of the aforementioned parameters on the intrinsic oxidative activity of the catalysts' surface. Instead, On the other hand, the Mn_3O_4/Mn_2O_3-SCS catalyst evidenced an outstanding catalytic activity under "loose" contact conditions, which was attributed to the combined effect of (i) a convenient filter-like morphology (that could have improved the capture of soot particles) and (ii) a probable high number of surface acid sites, characteristic of Mn_3O_4 catalysts.

Chapter 7

Final comments

7.1 General conclusions

This work comprehends the preparation and study of several metal oxide materials (cerium, manganese, copper, iron, -based) as oxidation catalysts for the elimination of volatile organic compounds (VOCs) and soot.

The first part of this work included the synthesis of three ceria-based families of mixed-oxide catalysts (i.e. Ce-Mn, Ce-Cu and Ce-Mn-Cu) by means of the solution combustion synthesis (SCS) and the corresponding catalytic study. As a whole, the binary and ternary catalysts evidenced better catalytic activities in the oxidation of VOCs probe molecules (propylene, ethylene), compared to the parent CeO_2, Mn_2O_3 and CuO catalysts. Moreover, the best performances were observed in the mixed oxides containing the highest loading of Mn, Cu, or Mn+Cu. The best activities were attributed to probable interactions taking place between different oxide phases and, as well, to the improved low-temperature reducibility of the catalysts. Furthermore, the most active catalysts in the oxidation of each VOC were deposited over SiC monoliths and tested in a bench-scale reactor. Accordingly, good and stable catalytic performances were observed over the catalyzed monoliths in the oxidation of the VOC probe molecules.

In the second part of this work, Cu and Fe -doped manganese oxides (and the corresponding parent oxides, i.e. the Mn_2O_3, Fe_2O_3 and CuO) were synthesized through a facile sol-gel preparation technique. The synthesized powders comprised mesoporous structures, were studied and tested in the oxidation of VOCs probe

molecules. Remarkable performances were observed in both the parent Mn_2O_3 and the Mn oxide doped with both Cu and Fe. Accordingly, the catalytic results highlighted the following parameters to play a key role in VOC oxidation: high population of surface-chemisorbed oxygen and better low-temperature reducibility. Moreover, synergistic interactions taking place between Mn, Cu and Fe seem to assure a better catalytic performance, compared to the other prepared oxides.

Subsequently, for the third part the catalysts prepared by means of sol-gel were further studied in the oxidation of propylene and soot. Particularly, the catalytic activity stability was investigated under gaseous streams containing humidity (5 vol.%) and over catalysts severely aged. The catalytic activity in soot oxidation was correlated to the ratio of Mn^{3+}/Mn^{2+} species present in the catalytic surface, thus demonstrating the key role of reducible species for the soot oxidation reaction. The incorporated Cu in the structure of Mn_2O_3 evidenced the best activity in propylene oxidation, and demonstrated to be reproducible and stable over long time in temperature swinging conditions. Finally, the simultaneous oxidation of soot and propylene was investigated. It was observed that both oxidation reactions took place contemporarily and that the presence of propylene seems to promote the oxidation of the soot particles at lower temperature.

For the last part, manganese oxides were prepared by means of both the solution combustion synthesis and the sol-gel technique. The physico-chemical properties of the catalysts were varied by changing the synthesis parameters. The catalytic performances of these materials were investigated in the oxidation of VOCs probe molecules and soot. In VOC oxidation the best performances were associated to high amounts of surface-chemisorbed oxygen, better low-temperature reducibility thus better oxygen mobility and the occurrence of small crystallites. As well, the soot oxidation results demonstrated the importance of elevated amounts of chemisorbed oxygen and better reducibility. Moreover, when intimate catalyst-soot contact was assured, the key role was played by the chemisorbed oxygen species, whereas under “loose” contact the activity was improved by means of morphological (filter-like) features and a probable high number of acid sites typical of Mn_3O_4 catalysts.

7.2 Future perspectives

Considering the different results from this work, a wide group of ideas appear feasible for future research activities. In this sense, the following tasks could complement the theoretical aspects revised in this dissertation:

Improvement of the catalytic activity of manganese oxides: According to the results included in this dissertation and the cited literature, manganese oxides revealed themselves as outstanding catalytic materials for both VOCs and soot oxidation. As a consequence, future investigations may include the tuning of physico-chemical properties in order to maximize the catalytic activities of these oxides. This could be achieved by changing the type of synthesis, synthesis parameters, oxidation state of Mn, and so on. As well, a better understanding of the role played by superficial acid sites in the mechanism of the studied oxidation reactions could be an interesting perspective.

Mn-Cu-O_x catalytic systems: The mixed Mn-Cu oxides as catalysts revealed a promising activity and stability toward the oxidation reaction of the investigated VOCs probe molecules. Considering their relatively high availability in the earth's crust, these catalysts are of great interest for future studies.

Occurrence of phase-interactions: The eventual occurrence of beneficial interactions (or synergistic in the best of cases) revealed to play a key role for observing low-temperature catalytic activity in the metal oxide catalysts. Therefore, a possible future activity could be the study of the dynamics that take between oxide phases that lead to the aforementioned catalytic enhancement.

Scale-up of catalytic materials: For future activities, it must be considered the insight given by this dissertation into the preparation of structured catalysts, i.e. catalyzed monoliths, and their good catalytic performances. In fact, the preparation and application of these monolithic catalysts is a first step from the base research to the development of this technology. In the best of cases, this type of assessment could bring this technology to a Technology Readiness Level (TRL) of 4. Meaning the effective validation in the laboratory of the catalytic material for an eventual application.

References

Abdelouahab-Reddam, Z., Mail, R. El, Coloma, F., & Sepúlveda-Escribano, A. (2015). Platinum supported on highly-dispersed ceria on activated carbon for the total oxidation of VOCs. *Applied Catalysis A: General*, *494*, 87–94. https://doi.org/10.1016/J.APCATA.2015.01.026

Aguilera, D. A., Perez, A., Molina, R., & Moreno, S. (2011). Cu-Mn and Co-Mn catalysts synthesized from hydrotalcites and their use in the oxidation of VOCs. *Applied Catalysis B: Environmental*, *104*(1–2), 144–150. https://doi.org/10.1016/j.apcatb.2011.02.019

Andana, T., Piumetti, M., Bensaid, S., Russo, N., Fino, D., & Pirone, R. (2016). Nanostructured ceria-praseodymia catalysts for diesel soot combustion. *Applied Catalysis B: Environmental*, *197*, 125–137. https://doi.org/10.1016/J.APCATB.2015.12.030

Aouad, S., Abi-Aad, E., & Aboukaïs, A. (2009, May 20). Simultaneous oxidation of carbon black and volatile organic compounds over Ru/CeO2 catalysts. *Applied Catalysis B: Environmental*, Vol. 88, pp. 249–256. https://doi.org/10.1016/j.apcatb.2008.10.002

Avgouropoulos, G., Ioannides, T., & Matralis, H. (2005). Influence of the preparation method on the performance of CuO-CeO 2 catalysts for the selective oxidation of CO. *Applied Catalysis B: Environmental*, *56*(1-2 SPEC. ISS.), 87–93. https://doi.org/10.1016/j.apcatb.2004.07.017

Avgouropoulos, George, & Ioannides, T. (2003). Selective CO oxidation over CuO-CeO2 catalysts prepared via the urea–nitrate combustion method. *Applied Catalysis A: General*, *244*(1), 155–167. https://doi.org/10.1016/S0926-860X(02)00558-6

Bensaid, S., Piumetti, M., Novara, C., Giorgis, F., Chiodoni, A., Russo, N., & Fino, D. (2016). Catalytic Oxidation of CO and Soot over Ce-Zr-Pr Mixed Oxides Synthesized in a Multi-Inlet Vortex Reactor: Effect of Structural Defects on the Catalytic Activity. *Nanoscale Research Letters*, *11*(1), 494. https://doi.org/10.1186/s11671-016-1713-1

Biesinger, M. C., Lau, L. W. M., Gerson, A. R., & Smart, R. S. C. (2010). Resolving surface chemical states in XPS analysis of first row transition metals, oxides

and hydroxides: Sc, Ti, V, Cu and Zn. *Applied Surface Science*, *257*(7), 887–898. https://doi.org/10.1016/j.apsusc.2010.10.051

Biesinger, M. C., Payne, B. P., Grosvenor, A. P., Lau, L. W. M., Gerson, A. R., & Smart, R. S. C. (2011). Resolving surface chemical states in XPS analysis of first row transition metals, oxides and hydroxides: Cr, Mn, Fe, Co and Ni. *Applied Surface Science*, *257*(7), 2717–2730. https://doi.org/10.1016/j.apsusc.2010.10.051

Bloemen, H. J. T., & Burn, J. (1993). *Chemistry and analysis of volatile organic compounds in the environment*. Springer.

Chen, D., He, D., Lu, J., Zhong, L., Liu, F., Liu, J., … Luo, Y. (2017). Investigation of the role of surface lattice oxygen and bulk lattice oxygen migration of cerium-based oxygen carriers: XPS and designed H2-TPR characterization. *Applied Catalysis B: Environmental*, *218*, 249–259. https://doi.org/10.1016/j.apcatb.2017.06.053

Christensen, J. M., Grunwaldt, J. D., & Jensen, A. D. (2017). Effect of NO2 and water on the catalytic oxidation of soot. *Applied Catalysis B: Environmental*, *205*, 182–188. https://doi.org/10.1016/j.apcatb.2016.12.024

Delimaris, D., & Ioannides, T. (2008). VOC oxidation over MnOx-CeO2 catalysts prepared by a combustion method. *Applied Catalysis B: Environmental*, *84*(1–2), 303–312. https://doi.org/10.1016/j.apcatb.2009.02.003

Delimaris, D., & Ioannides, T. (2009). VOC oxidation over CuO-CeO_2 catalysts prepared by a combustion method. *Applied Catalysis B: Environmental*, *89*(1–2), 295–302. https://doi.org/10.1016/j.apcatb.2009.02.003

Deng, W., Dai, Q., Lao, Y., Shi, B., & Wang, X. (2015). Low temperature catalytic combustion of 1,2-dichlorobenzene over CeO2-TiO2mixed oxide catalysts. *Applied Catalysis B: Environmental*, *181*, 848–861. https://doi.org/10.1016/j.apcatb.2015.07.053

Deorsola, F. A., Andreoli, S., Armandi, M., Bonelli, B., & Pirone, R. (2016). Unsupported nanostructured Mn oxides obtained by Solution Combustion Synthesis: Textural and surface properties, and catalytic performance in NOx SCR at low temperature. *Applied Catalysis A: General*, *522*, 120–129. https://doi.org/10.1016/j.apcata.2016.05.002

Dosa, M., Piumetti, M., Bensaid, S., Andana, T., Novara, C., Giorgis, F., … Russo, N. (2018). Novel Mn–Cu-Containing CeO2 Nanopolyhedra for the Oxidation of CO and Diesel Soot: Effect of Dopants on the Nanostructure and Catalytic Activity. *Catalysis Letters*, *148*(1), 298–311. https://doi.org/10.1007/s10562-

017-2226-y

Dupin, J.-C., Gonbeau, D., Vinatier, P., & Levasseur, A. (2000). Systematic XPS studies of metal oxides, hydroxides and peroxides. *Physical Chemistry Chemical Physics*, *2*(6), 1319–1324. https://doi.org/10.1039/A908800H

Ertl, G., Knözinger, H., & Weitkamp, J. (2008). Handbook of Heterogeneous Catalysis. In *Handbook of Heterogeneous Catalysis* (Vol. 1–5). https://doi.org/10.1524/zpch.1999.208.part_1_2.274

European Parliament and Council. (2004). Directive 2004/42/CE on the limitation of emissions of volatile organic compounds due to the use of organic solvents in certain paints and varnishes and vehicle refinishing products and amending Directive 1999/13/EC. *Official Journal of the European Union*, 10. Retrieved from https://eur-lex.europa.eu/legal-content/EN/TXT/PDF/?uri=CELEX:32004L0042&from=EN

European Parliament and Council. (2008). DIRECTIVE 2008/50/EC OF THE EUROPEAN PARLIAMENT AND OF THE COUNCIL. *Official Journal of the European Union*, 44. Retrieved from https://eur-lex.europa.eu/legal-content/EN/TXT/?uri=CELEX:32008L0050

FANG, J., CHEN, X., XIA, Q., XI, H., & LI, Z. (2009). Effect of Relative Humidity on Catalytic Combustion of Toluene over Copper Based Catalysts with Different Supports. *Chinese Journal of Chemical Engineering*, *17*(5), 767–772. https://doi.org/10.1016/S1004-9541(08)60275-X

Fawole, O. G., Cai, X. M., & Mackenzie, A. R. (2016). Gas flaring and resultant air pollution: A review focusing on black carbon. *Environmental Pollution*, *216*, 182–197. https://doi.org/10.1016/J.ENVPOL.2016.05.075

Fino, D., Bensaid, S., Piumetti, M., & Russo, N. (2016). A review on the catalytic combustion of soot in Diesel particulate filters for automotive applications: From powder catalysts to structured reactors. *Applied Catalysis A: General*, *509*, 75–96. https://doi.org/10.1016/J.APCATA.2015.10.016

Fu, N., Wei, P., Jia, Y., Zheng, X., & Guan, J. (2021). Indoor volatile organic compounds in densely occupied education buildings of four universities: Target list, concentration levels and correlation analysis. *Building and Environment*, *191*, 107599. https://doi.org/10.1016/j.buildenv.2021.107599

Gandhe, A. R., Rebello, J. S., Figueiredo, J. L., & Fernandes, J. B. (2007). Manganese oxide OMS-2 as an effective catalyst for total oxidation of ethyl acetate. *Applied Catalysis B: Environmental*, *72*(1–2), 129–135. https://doi.org/10.1016/j.apcatb.2006.10.017

Gelles, T., Krishnamurthy, A., Adebayo, B., Rownaghi, A., & Rezaei, F. (2020). Abatement of gaseous volatile organic compounds: A material perspective. *Catalysis Today*, *350*, 3–18. https://doi.org/10.1016/j.cattod.2019.06.017

Genuino, H. C., Dharmarathna, S., Njagi, E. C., Mei, M. C., & Suib, S. L. (2012). *Gas-Phase Total Oxidation of Benzene, Toluene, Ethylbenzene, and Xylenes Using Shape-Selective Manganese Oxide and Copper Manganese Oxide Catalysts*. https://doi.org/10.1021/jp301342f

Godoy, M., Banús, E., Sanz, O., Montes, M., Miró, E., & Milt, V. (2018). Stacked Wire Mesh Monoliths for the Simultaneous Abatement of VOCs and Diesel Soot. *Catalysts*, *8*(1), 16. https://doi.org/10.3390/catal8010016

Gross, M. S., Ulla, M. A., & Querini, C. A. (2012). Diesel particulate matter combustion with CeO2 as catalyst. Part I: System characterization and reaction mechanism. *Journal of Molecular Catalysis A: Chemical*, *352*, 86–94. https://doi.org/10.1016/J.MOLCATA.2011.10.018

Guo, X., & Zhou, R. (2016). A new insight into the morphology effect of ceria on CuO/CeO 2 catalysts for CO selective oxidation in hydrogen-rich gas. *Catalysis Science & Technology*, *6*(11), 3862–3871. https://doi.org/10.1039/C5CY01816A

Gupta, T., & Kumar Singh, D. (2016). *Organic Species Emitted as a Part of Combustion Residue: Fate and Transformation in the Ambient Air Critical microenvironment View project Design innovation View project Organic Species Emitted as a Part of Combustion Residue: Fate and Transformation in the Ambient Air*. Retrieved from https://www.researchgate.net/publication/298392042

Heynderickx, P. M., Thybaut, J. W., Poelman, H., Poelman, D., & Marin, G. B. (2010). The total oxidation of propane over supported Cu and Ce oxides: A comparison of single and binary metal oxides. *Journal of Catalysis*, *272*(1), 109–120. https://doi.org/10.1016/j.jcat.2010.03.006

Hime, N. J., Marks, G. B., & Cowie, C. T. (2018). A Comparison of the Health Effects of Ambient Particulate Matter Air Pollution from Five Emission Sources. *International Journal of Environmental Research and Public Health 2018, Vol. 15, Page 1206*, *15*(6), 1206. https://doi.org/10.3390/IJERPH15061206

Imamura, S., Shono, M., Okamoto, N., Hamada, A., & Ishida, S. (1996). Effect of cerium on the mobility of oxygen on manganese oxides. *Applied Catalysis A: General*, *142*(2), 279–288. https://doi.org/10.1016/0926-860X(96)00095-6

Joung, H. J., Kim, J. H., Oh, J. S., You, D. W., Park, H. O., & Jung, K. W. (2014). Catalytic oxidation of VOCs over CNT-supported platinum nanoparticles. *Applied Surface Science*, *290*, 267–273. https://doi.org/10.1016/J.APSUSC.2013.11.066

Kamal, M. S., Razzak, S. A., & Hossain, M. M. (2016). Catalytic oxidation of volatile organic compounds (VOCs) – A review. *Atmospheric Environment*, *140*, 117–134. https://doi.org/10.1016/J.ATMOSENV.2016.05.031

Kapteijn, F., Singoredjo, L., Andreini, A., & Moulijn, J. A. (1994). Activity and selectivity of pure manganese oxides in the selective catalytic reduction of nitric oxide with ammonia. *Applied Catalysis B: Environmental*, *3*(2–3), 173–189. https://doi.org/10.1016/0926-3373(93)E0034-9

Khan, F. I., & Kr. Ghoshal, A. (2000). Removal of Volatile Organic Compounds from polluted air. *Journal of Loss Prevention in the Process Industries*, *13*(6), 527–545. https://doi.org/10.1016/S0950-4230(00)00007-3

Kim, S. C., & Shim, W. G. (2010). Catalytic combustion of VOCs over a series of manganese oxide catalysts. *Applied Catalysis B: Environmental*, *98*(3–4), 180–185. https://doi.org/10.1016/j.apcatb.2010.05.027

Koppmann, R. (2007). *Volatile organic compounds in the atmosphere*. Blackwell Pub.

Krishnamurthy, A., Adebayo, B., Gelles, T., Rownaghi, A., & Rezaei, F. (2020). Abatement of gaseous volatile organic compounds: A process perspective. *Catalysis Today*, *350*, 100–119. https://doi.org/10.1016/j.cattod.2019.05.069

Kundakovic, L., & Flytzani-Stephanopoulos, M. (1998). Reduction characteristics of copper oxide in cerium and zirconium oxide systems. *Applied Catalysis A: General*, *171*(1), 13–29. https://doi.org/10.1016/S0926-860X(98)00056-8

Lee, J. H., Jo, D. Y., Choung, J. W., Kim, C. H., Ham, H. C., & Lee, K. Y. (2021). Roles of noble metals (M = Ag, Au, Pd, Pt and Rh) on CeO2 in enhancing activity toward soot oxidation: Active oxygen species and DFT calculations. *Journal of Hazardous Materials*, *403*, 124085. https://doi.org/10.1016/J.JHAZMAT.2020.124085

Leith, I. R., & Howden, M. G. (1988). Temperature-programmed reduction of mixed iron-manganese oxide catalysts in hydrogen and carbon monoxide. *Applied Catalysis*, *37*(C), 75–92. https://doi.org/10.1016/S0166-9834(00)80752-6

Li, C., Xin, Q., & Guo, X. xian. (1992). Surface oxygen species and their

reactivities in the mild oxidation of ethylene on cerium oxide studied by FT-IR spectroscopy. *Catalysis Letters*, *12*(1–3), 297–305. https://doi.org/10.1007/BF00767212

Li, T., Yang, Y., Zhang, C., Tao, Z., Wan, H., An, X., … Li, Y. (2007). Effect of Manganese Incorporation Manner on an Iron-Based Catalyst for Fischer-Tropsch Synthesis. *Journal of Natural Gas Chemistry*, *16*(3), 244–251. https://doi.org/10.1016/S1003-9953(07)60055-3

Li, W. B., Wang, J. X., & Gong, H. (2010). Catalytic combustion of VOCs on non-noble metal catalysts. *Catalysis Today*, *148*(1–2), 81–87. https://doi.org/10.1016/j.cattod.2009.03.007

Li, X., Zhang, L., Yang, Z., Wang, P., Yan, Y., & Ran, J. (2020). Adsorption materials for volatile organic compounds (VOCs) and the key factors for VOCs adsorption process: A review. *Separation and Purification Technology*, *235*, 116213. https://doi.org/10.1016/j.seppur.2019.116213

Li, Y., Fu, Q., & Flytzani-Stephanopoulos, M. (2000). Low-temperature water-gas shift reaction over Cu- and Ni-loaded cerium oxide catalysts. *Applied Catalysis B: Environmental*, *27*(3), 179–191. https://doi.org/10.1016/S0926-3373(00)00147-8

Li, Z., Meng, M., Zha, Y., Dai, F., Hu, T., Xie, Y., & Zhang, J. (2012). Highly efficient multifunctional dually-substituted perovskite catalysts La 1-xK xCo 1-yCu yO 3-δ used for soot combustion, NOx storage and simultaneous NOx-soot removal. *Applied Catalysis B: Environmental*, *121–122*, 65–74. https://doi.org/10.1016/j.apcatb.2012.03.022

Liang, Q., Wu, X., Weng, D., & Xu, H. (2008). Oxygen activation on Cu/Mn-Ce mixed oxides and the role in diesel soot oxidation. *Catalysis Today*, *139*(1–2), 113–118. https://doi.org/10.1016/j.cattod.2008.08.013

Lin, X., Li, S., He, H., Wu, Z., Wu, J., Chen, L., … Fu, M. (2018). Evolution of oxygen vacancies in MnOx-CeO2mixed oxides for soot oxidation. *Applied Catalysis B: Environmental*, *223*, 91–102. https://doi.org/10.1016/j.apcatb.2017.06.071

Liotta, L. F. (2010, October 20). Catalytic oxidation of volatile organic compounds on supported noble metals. *Applied Catalysis B: Environmental*, Vol. 100, pp. 403–412. https://doi.org/10.1016/j.apcatb.2010.08.023

Liu, S., Wu, X., Weng, D., & Ran, R. (2015). Ceria-based catalysts for soot oxidation: a review. *Journal of Rare Earths*, *33*(6), 567–590. https://doi.org/10.1016/S1002-0721(14)60457-9

Liu, W., & Flytzani-Stephanopoulos, M. (1995a). Total Oxidation of Carbon monoxide and Methane over Transition Metal-Fluorite Oxide Composite Catalysts.pdf. *Journal of Catalysis*, *153*, 317–332.

Liu, W., & Flytzani-Stephanopoulos, M. (1995b). Total oxidation of carbon monoxide and methane over transition metal fluorite oxide composite catalysts: I. Catalyst composition and activity. *Journal of Catalysis*, *153*(2), 304–316. https://doi.org/10.1006/jcat.1995.1132

Liu, Y., Dai, H., Deng, J., Xie, S., Yang, H., Tan, W., … Guo, G. (2014). Mesoporous Co3O4-supported gold nanocatalysts: Highly active for the oxidation of carbon monoxide, benzene, toluene, and o-xylene. *Journal of Catalysis*, *309*, 408–418. https://doi.org/10.1016/j.jcat.2013.10.019

Machida, M., Uto, M., Kurogi, D., & Kijima, T. (2000). MnO(x)-CeO2binary oxides for catalytic NO(x) sorption at low temperatures. Sorptive removal of NO(x). *Chemistry of Materials*, *12*(10), 3158–3164. https://doi.org/10.1021/cm000207r

Marin Figueredo, M. J., Andana, T., Bensaid, S., Dosa, M., Fino, D., Russo, N., & Piumetti, M. (2020). Cerium–Copper–Manganese Oxides Synthesized via Solution Combustion Synthesis (SCS) for Total Oxidation of VOCs. *Catalysis Letters*, *150*(6), 1821–1840. https://doi.org/10.1007/s10562-019-03094-x

Marin Figueredo, M. J., Cocuzza, C., Bensaid, S., Fino, D., Piumetti, M., & Russo, N. (2021). Catalytic Abatement of Volatile Organic Compounds and Soot over Manganese Oxide Catalysts. *Materials 2021, Vol. 14, Page 4534*, *14*(16), 4534. https://doi.org/10.3390/MA14164534

Marin Figueredo, M. J., Piumetti, M., Bensaid, S., Fino, D., & Nunzio, R. (2021). Catalytic Oxidation of Volatile Organic Compounds over Porous Manganese Oxides Prepared via Sol-Gel Method. *Nanostructured Catalysts for Environmental Applications*, 59–78. https://doi.org/10.1007/978-3-030-58934-9_2

Marin Figueredo, M. J., Piumetti, M., Fino, D., Russo, N., Cocuzza, C., & Bensaid, S. (2021). Catalytic Oxidation of Soot and Volatile Organic Compounds over Cu and Fe Doped Manganese Oxides Prepared via Sol-Gel Synthesis. *SAE Technical Papers*, (2021). https://doi.org/10.4271/2021-24-0088

Mars, P., & van Krevelen, D. W. (1954). Oxidations carried out by means of vanadium oxide catalysts. *Chemical Engineering Science*, *3*, 41–59. https://doi.org/10.1016/S0009-2509(54)80005-4

Mohankumar, S., & Senthilkumar, P. (2017, December 1). Particulate matter

formation and its control methodologies for diesel engine: A comprehensive review. *Renewable and Sustainable Energy Reviews*, Vol. 80, pp. 1227–1238. https://doi.org/10.1016/j.rser.2017.05.133

Morales, Maria R., Yeste, M. P., Vidal, H., Gatica, J. M., & Cadus, L. E. (2017). Insights on the combustion mechanism of ethanol and n-hexane in honeycomb monolithic type catalysts: Influence of the amount and nature of Mn-Cu mixed oxide. *Fuel*, *208*, 637–646. https://doi.org/10.1016/J.FUEL.2017.07.069

Morales, María Roxana, Barbero, B. P., & Cadús, L. E. (2006). Total oxidation of ethanol and propane over Mn-Cu mixed oxide catalysts. *Applied Catalysis B: Environmental*, *67*(3–4), 229–236. https://doi.org/10.1016/j.apcatb.2006.05.006

Morales, María Roxana, Barbero, B. P., & Cadús, L. E. (2008). Evaluation and characterization of Mn-Cu mixed oxide catalysts for ethanol total oxidation: Influence of copper content. *Fuel*, *87*(7), 1177–1186. https://doi.org/10.1016/j.fuel.2007.07.015

Moulder, J. F., Stickle, W. F., Sobol, P. E., & Bomben, K. D. (1992). *Handbook of X-ray Photoelectron Spectroscopy* (J. Chastain, Ed.). Eden Prairie, United States of America: Perkin-Elmer Corporation, Physical Electronics Division.

Mukherjee, A., & Agrawal, M. (n.d.). *World air particulate matter: sources, distribution and health effects*. https://doi.org/10.1007/s10311-017-0611-9

Mullins, D. R. (2015). The surface chemistry of cerium oxide. *Surface Science Reports*, *70*(1), 42–85. https://doi.org/10.1016/j.surfrep.2014.12.001

Munteanu, G., Ilieva, L., & Andreeva, D. (1997). Kinetic parameters obtained from TPR data for α-Fe2O3 and Au/α-Fe2O3 systems. *Thermochimica Acta*, *291*(1–2), 171–177. https://doi.org/10.1016/S0040-6031(96)03097-3

Ni, M., Huang, J., Lu, S., Li, X., Yan, J., & Cen, K. (2014). A review on black carbon emissions, worldwide and in China. *Chemosphere*, *107*, 83–93. https://doi.org/10.1016/J.CHEMOSPHERE.2014.02.052

Njagi, E. C., Genuino, H. C., King'Ondu, C. K., Dharmarathna, S., & Suib, S. L. (2012). Catalytic oxidation of ethylene at low temperatures using porous copper manganese oxides. *Applied Catalysis A: General*, *421–422*, 154–160. https://doi.org/10.1016/j.apcata.2012.02.011

Palmisano, P., Russo, N., Fino, P., Fino, D., & Badini, C. (2006). High catalytic activity of SCS-synthesized ceria towards diesel soot combustion. *Applied Catalysis B: Environmental*, *69*(1–2), 85–92.

https://doi.org/10.1016/J.APCATB.2006.06.002

Peralta, M. A., Milt, V. G., Cornaglia, L. M., & Querini, C. A. (2006). Stability of Ba,K/CeO2 catalyst during diesel soot combustion: Effect of temperature, water, and sulfur dioxide. *Journal of Catalysis*, *242*(1), 118–130. https://doi.org/10.1016/j.jcat.2006.05.025

Piumetti, M., & Russo, N. (2017). *Notes on Catalysis for Environment and Energy*. CLUT-Politecnico di Torino.

Piumetti, Marco, Bensaid, S., Andana, T., Dosa, M., Novara, C., Giorgis, F., … Fino, D. (2017). Nanostructured Ceria-Based Materials: Effect of the Hydrothermal Synthesis Conditions on the Structural Properties and Catalytic Activity. *Catalysts*, *7*(6), 174. https://doi.org/10.3390/catal7060174

Piumetti, Marco, Bensaid, S., Andana, T., Russo, N., Pirone, R., & Fino, D. (2017). Cerium-copper oxides prepared by solution combustion synthesis for total oxidation reactions: From powder catalysts to structured reactors. *Applied Catalysis B: Environmental*, *205*, 455–468. https://doi.org/10.1016/j.apcatb.2016.12.054

Piumetti, Marco, Bensaid, S., Russo, N., & Fino, D. (2015). Nanostructured ceria-based catalysts for soot combustion: Investigations on the surface sensitivity. *Applied Catalysis B: Environmental*, *165*, 742–751. https://doi.org/10.1016/j.apcatb.2014.10.062

Piumetti, Marco, Fino, D., & Russo, N. (2015). Mesoporous manganese oxides prepared by solution combustion synthesis as catalysts for the total oxidation of VOCs. *Applied Catalysis B: Environmental*, *163*, 277–287. https://doi.org/10.1016/j.apcatb.2014.08.012

Piumetti, Marco, van der Linden, B., Makkee, M., Miceli, P., Fino, D., Russo, N., & Bensaid, S. (2016). Contact dynamics for a solid-solid reaction mediated by gas-phase oxygen: Study on the soot oxidation over ceria-based catalysts. *Applied Catalysis B: Environmental*, *199*, 96–107. https://doi.org/10.1016/j.apcatb.2016.06.006

Platau, A., Johansson, L. I., Hagström, A. L., Karlsson, S. E., & Hagström, S. B. M. (1977). Oxidation of cerium and titanium studied by photoelectron spectroscopy. *Surface Science*, *63*(C), 153–161. https://doi.org/10.1016/0039-6028(77)90334-X

Ramírez, N., Cuadras, A., Rovira, E., Borrull, F., & Marcé, R. M. (2012). Chronic risk assessment of exposure to volatile organic compounds in the atmosphere near the largest Mediterranean industrial site. *Environment International*,

39(1), 200–209. https://doi.org/10.1016/j.envint.2011.11.002

Ranji-Burachaloo, H., Masoomi-Godarzi, S., Khodadadi, A. A., & Mortazavi, Y. (2016). Synergetic effects of plasma and metal oxide catalysts on diesel soot oxidation. *Applied Catalysis B: Environmental*, *182*, 74–84. https://doi.org/10.1016/j.apcatb.2015.09.019

Reitz, J. B., & Solomon, E. I. (1998). Propylene oxidation on copper oxide surfaces: Electronic and geometric contributions to reactivity and selectivity. *Journal of the American Chemical Society*, *120*(44), 11467–11478. https://doi.org/10.1021/ja981579s

Santos, V. P., Pereira, M. F. R., Órfão, J. J. M., & Figueiredo, J. L. (2009). Synthesis and Characterization of Manganese Oxide Catalysts for the Total Oxidation of Ethyl Acetate. *Topics in Catalysis*, *52*(5), 470–481. https://doi.org/10.1007/s11244-009-9187-3

Santos, V. P., Pereira, M. F. R., Órfão, J. J. M., & Figueiredo, J. L. (2010). The role of lattice oxygen on the activity of manganese oxides towards the oxidation of volatile organic compounds. *Applied Catalysis B: Environmental*, *99*(1–2), 353–363. https://doi.org/10.1016/j.apcatb.2010.07.007

Sarigiannis, D. A., Karakitsios, S. P., Gotti, A., Liakos, I. L., & Katsoyiannis, A. (2011). Exposure to major volatile organic compounds and carbonyls in European indoor environments and associated health risk. *Environment International*, *37*(4), 743–765. https://doi.org/10.1016/J.ENVINT.2011.01.005

Shannon, R. D. (1976). Revised effective ionic radii and systematic studies of interatomic distances in halides and chalcogenides. *Acta Crystallographica Section A*, *32*(5), 751–767. https://doi.org/10.1107/S0567739476001551

Spinicci, R., & Tofanari, A. (1990). Characterization of catalysts for methane-coupling by means of temperature programmed desorption. *Catalysis Today*, *6*(4), 473–479. https://doi.org/10.1016/0920-5861(90)85041-L

Spivey, J. J. (1987). Complete Catalytic Oxidation of Volatile Organics. *Industrial and Engineering Chemistry Research*, *26*(11), 2165–2180. https://doi.org/10.1021/ie00071a001

Trovarelli, A. (2002). *Catalysis by ceria and related materials*. Retrieved from https://www.worldcat.org/title/catalysis-by-ceria-and-related-materials/oclc/49785570

U.S. Environmental Protection Agency. Office of Air and Radiation. *Control*

Techniques for Volatile Organic Compound Emissions from Stationary Sources. , (1992).

United States Environmental Protection Agency. (2021a). Particulate Matter (PM) Basics | US EPA. Retrieved August 26, 2021, from https://www.epa.gov/pm-pollution/particulate-matter-pm-basics#PM

United States Environmental Protection Agency. (2021b). Technical Overview of Volatile Organic Compounds. Retrieved August 23, 2021, from https://www.epa.gov/indoor-air-quality-iaq/technical-overview-volatile-organic-compounds#2

Wagloehner, S., Baer, J. N., & Kureti, S. (2014). Structure-activity relation of iron oxide catalysts in soot oxidation. *Applied Catalysis B: Environmental*, *147*, 1000–1008. https://doi.org/10.1016/j.apcatb.2013.09.049

Wagloehner, S., Nitzer-Noski, M., & Kureti, S. (2015). Oxidation of soot on manganese oxide catalysts. *Chemical Engineering Journal*, *259*, 492–504. https://doi.org/10.1016/j.cej.2014.08.021

Wang, H., Lu, Y., Han, Y. X., Lu, C., Wan, H., Xu, Z., & Zheng, S. (2017). Enhanced catalytic toluene oxidation by interaction between copper oxide and manganese oxide in Cu-O-Mn/γ-Al2O3catalysts. *Applied Surface Science*, *420*, 260–266. https://doi.org/10.1016/j.apsusc.2017.05.133

Wang, Q., Yeung, K. L., & Bañares, M. A. (2020, October 1). Ceria and its related materials for VOC catalytic combustion: A review. *Catalysis Today*, Vol. 356, pp. 141–154. https://doi.org/10.1016/j.cattod.2019.05.016

Wasalathanthri, N. D., SantaMaria, T. M., Kriz, D. A., Dissanayake, S. L., Kuo, C. H., Biswas, S., & Suib, S. L. (2017). Mesoporous manganese oxides for NO2 assisted catalytic soot oxidation. *Applied Catalysis B: Environmental*, *201*, 543–551. https://doi.org/10.1016/j.apcatb.2016.08.052

Wöllner, A., Lange, F., Schmelz, H., & Knözinger, H. (1993). Characterization of mixed copper-manganese oxides supported on titania catalysts for selective oxidation of ammonia. *Applied Catalysis A, General*, *94*(2), 181–203. https://doi.org/10.1016/0926-860X(93)85007-C

Wood, B. J., Wise, H., & Yolles, R. S. (1969). Selectivity and stoichiometry of copper oxide in propylene oxidation. *Journal of Catalysis*, *15*(4), 355–362. https://doi.org/10.1016/0021-9517(69)90304-2

Wu, W., Jin, Y., & Carlsten, C. (2018). Inflammatory health effects of indoor and outdoor particulate matter. *Journal of Allergy and Clinical Immunology*,

141(3), 833–844. https://doi.org/10.1016/J.JACI.2017.12.981

Yamashita, T., & Hayes, P. (2008). Analysis of XPS spectra of Fe 2+ and Fe 3+ ions in oxide materials. *Applied Surface Science*, *254*(8), 2441–2449. https://doi.org/10.1016/j.apsusc.2007.09.063

Yang, C., Miao, G., Pi, Y., Xia, Q., Wu, J., Li, Z., & Xiao, J. (2019, August 15). Abatement of various types of VOCs by adsorption/catalytic oxidation: A review. *Chemical Engineering Journal*, Vol. 370, pp. 1128–1153. https://doi.org/10.1016/j.cej.2019.03.232

Zawadzki, M., & Trawczyński, J. (2011). Synthesis, characterization and catalytic performance of LSCF perovskite for VOC combustion. *Catalysis Today*, *176*(1), 449–452. https://doi.org/10.1016/j.cattod.2010.10.070

Zhang, X., & Wu, D. (2016). Ceramic monolith supported Mn–Ce–M ternary mixed-oxide (M=Cu, Ni or Co) catalyst for VOCs catalytic oxidation. *Ceramics International*, *42*(15), 16563–16570. https://doi.org/10.1016/J.CERAMINT.2016.07.076

Zhang, Z., Jiang, Z., & Shangguan, W. (2016). Low-temperature catalysis for VOCs removal in technology and application: A state-of-the-art review. *Catalysis Today*, *264*, 270–278. https://doi.org/10.1016/j.cattod.2015.10.040

Zieliński, J., Zglinicka, I., Znak, L., & Kaszkur, Z. (2010). Reduction of Fe2O3 with hydrogen. *Applied Catalysis A: General*, *381*(1–2), 191–196. https://doi.org/10.1016/j.apcata.2010.04.003